THE UNIVERSITY *of* EDINBURGH

S-Process Nucleosynthesis of Updated AGB Star Models and Abundance Uncertainties from Nuclear Reaction Rates

Ashley Tattersall

Doctor of Philosophy
The University of Edinburgh
February 2025

Abstract

To understand the origin of the solar system's elemental abundances is a major challenge in astrophysics. Many generations of past stars and processes have contributed to the solar abundances. The abundances of the heavy elements beyond iron that we observe today in the solar system are mainly the result of two nucleosynthesis processes: the slow neutron-capture process (s-process) and the rapid neutron-capture process (r-process). Low-mass asymptotic giant branch (AGB) ($2 < M/M_{\odot} < 3$) and massive ($M/M_{\odot} > 10$) stars have been identified as the sites of the s-process. The s-process nucleosynthetic yields of low-mass AGB stars (initial mass $M/M_{\odot} = 2$, 3, and metallicity, Z = 0.01, 0.02 and 0.03) were calculated using stellar models with an updated mixing scheme. The ^{13}C-pocket, a thin shell in the star where s-process material is produced, is formed through mixing induced by internal gravity waves (IGWs). This results in a pocket three times larger on average and hence larger s-process production compared to previous models. The full nucleosynthesis was calculated in post-processing using the NuGrid MPPNP code. Isotopic and elemental abundances are compared to other stellar data sets available in the literature and to a wide range of observations, including carbon-stars, barium stars, and pre-solar grains. Good agreement was determined with few exceptions, for example ^{96}Mo, ^{137}Ba and ^{138}Ba. To judge the significance of (dis)agreements of our model results with observations, uncertainties of stellar yields and surface abundances due to uncertainties in nuclear reaction rates were determined, by adopting a Monte Carlo method. Rates for all neutron capture and neutron source reactions were simultaneously varied within their uncertainties in 10000 one zone nucleosynthesis calculations, resulting in an equal number of final isotopic abundances. The most important (key) nuclear reactions impacting on certain abundance changes were determined by calculation of Pearson correlation coefficients. Subsequently, these key nuclear reaction rates were varied within uncertainties in full multi zone post-processing calculations and results were used to estimate total uncertainties in

stellar yields and surface abundances. Many abundance ratios can be constrained within 10% of the uncertainties from the nuclear physics input. Some are significantly higher than this, i.e. $^{84}Sr/^{86}Sr$, $^{88}Sr/^{86}Sr$, $^{96}Zr/^{94}Zr$ and $^{100}Mo/^{96}Mo$. The higher uncertainties are due to the uncertain neutron capture cross sections of branching point nuclei, which have not been determined experimentally yet.

Lay Summary

Stars are the primary source of the chemical elements in the Universe. They produce the elements throughout their lives (and deaths) by nuclear reactions, i.e. the combination of atomic nuclei. Some of these nuclear reactions, allow the star to generate energy and remain stable against their own gravity.

This thesis studies the production of the heavy elements, which are elements heavier than iron, in asymptotic giant branch (AGB) stars. AGB stars are stars like our Sun, but in an advanced stage of their evolution. AGB stars have finished burning helium in their cores and consist of an inert core made of carbon and oxygen. They create energy by the fusion of hydrogen and helium in thin shells. In this region of the star, the heavy elements are created by the absorption of neutrons. The freshly synthesised elements are then transported to the stellar surface and can be observed with modern day telescopes.

In this thesis, updated models of the evolution of AGB stars have been used to calculate the creation of the heavy elements. It was found that a higher amount of heavy elements are produced for the updated models compared to previously, and results showed good agreement with astronomical observations. The stellar models and nucleosynthesis calculations rely on inputs that are uncertain. The impact of poorly understood mixing processes in the star, as well as poorly known nuclear reaction probabilities was investigated. This allowed to identify nuclear reactions which should be studied in experimental laboratories in the future.

Acknowledgments

First and foremost, I want to thank my supervisors: Claudia Lederer-Woods, Umberto Battino, and Alex Murphy, to whom I am greatly indebted to for all the support and guidance they provided throughout my studies.

Also, I thank the members of the NuGrid collaboration, the staff, and the students of the nuclear physics group at the University of Edinburgh for making my time in Edinburgh enjoyable. I am grateful for your friendship and support.

Finally, I thank my family for their constant support and the University of Edinburgh for providing me with this opportunity.

Contents

List of Figures

List of Tables

Chapter 1

Introduction

1.1 Evolution and Nucleosynthesis of Intermediate Mass Stars

A star is a massive, luminous sphere of plasma held together by gravity. Stars need to provide thermal pressure to counteract the inward pull of gravity to remain stable (hydrostatic equilibrium). This thermal pressure is provided by nuclear fusion, where nuclei combine to form heavier nuclei releasing energy. Stars are composed of mainly hydrogen and helium, which were already formed in the first few minutes after the Big Bang[1]. Elements heavier than helium, which are referred to as "metals" in astronomy, make up only a few percent of the composition (and this percentage is used to define the metallicity of a star, denoted by Z).

The following chapter will discuss the evolution and nucleosynthesis of stars, with a focus on intermediate mass stars defined as stars with initial mass between 1.8 $< M_{\odot} <$ 10 ($M_{\odot}$ is the solar mass) (Herwig et al. [93]), which are of relevance to this thesis. For a comprehensive overview refer for example to Iliadis [97] and Kippenhahn et al. [108]. The evolutionary path of a star can be tracked observationally with the aid of a Hertzsprung Russel (HR) diagram, which

[1]Big Bang nucleosynthesis (BBN) (also called primordial nucleosynthesis) occurred within the first few minutes after the Big Bang when the universe was extremely hot and dense. During this brief period, nuclear reactions fused protons and neutrons into helium and small traces of other light elements like deuterium (^{2}H), ^{3}He, and lithium. Primordial nucleosynthesis created the initial composition of the light element abundance in the universe.

displays the surface temperature vs the star's luminosity (Figure 1.1). When a proto-star contracts, it heats up, eventually reaching temperatures high enough to start the first, and longest, burning stage in the life of a star, hydrogen burning. During this period, the star remains on the so-called "main sequence" of the HR diagram (see Figure 1.1). Hydrogen burning is where 4 hydrogen (H) nuclei fuse to form a helium (He) nucleus, releasing about 26 MeV of energy per fusion. For stars with mass below $1.3M_{\odot}$ (Salaris & Cassisi [187]) this happens through the pp chain (Adelberger et al. [2]), which is a reaction sequence starting with

$$p + p \rightarrow {}^{2}H + e^{+} + \nu_{e}. \tag{1.1}$$

Deuterium is then rapidly destroyed by a subsequent proton capture forming ^{3}He

$$p + {}^{2}H \rightarrow {}^{3}He + \gamma. \tag{1.2}$$

Finally, the combination of 2 ^{3}He nuclei results in ^{4}He and 2 protons via

$${}^{3}He + {}^{3}He \rightarrow {}^{4}He + 2p, \tag{1.3}$$

which closes the ppI chain. There are also other branches possible (pp II and pp III) which utilise ^{4}He as catalysts. For temperatures in the Sun's core (15 MK) the ppI chain dominates hydrogen burning. Stars of mass higher than 1.3 $M_{\odot}$ and with some pre-existing carbon, nitrogen and oxygen nuclei burn hydrogen through the so-called CNO cycle (or Bethe Weizsäcker cycle), where carbon, nitrogen and oxygen are used as catalysts. The reaction sequence for the CNO-I chain (Krane [114]) is

$$\begin{aligned}
{}^{12}C + p &\rightarrow {}^{13}N + \gamma \\
{}^{13}N &\rightarrow {}^{13}C + e^{+} + \nu_{e} \\
{}^{13}C + p &\rightarrow {}^{14}N + \gamma \\
{}^{14}N + p &\rightarrow {}^{15}O + \gamma \\
{}^{15}O &\rightarrow {}^{15}N + e^{+} + \nu_{e} \\
{}^{15}N + p &\rightarrow {}^{12}C + {}^{4}He
\end{aligned} \tag{1.4}$$

As can be seen, while ^{12}C is transformed initially into ^{13}N, it is regenerated in a later step. The CNO cycle changes abundances ratios C/N and C/O, in particular, ^{14}N(p,γ) is the slowest in the cycle due to it low cross section, hence matter accumulates at ^{14}N.

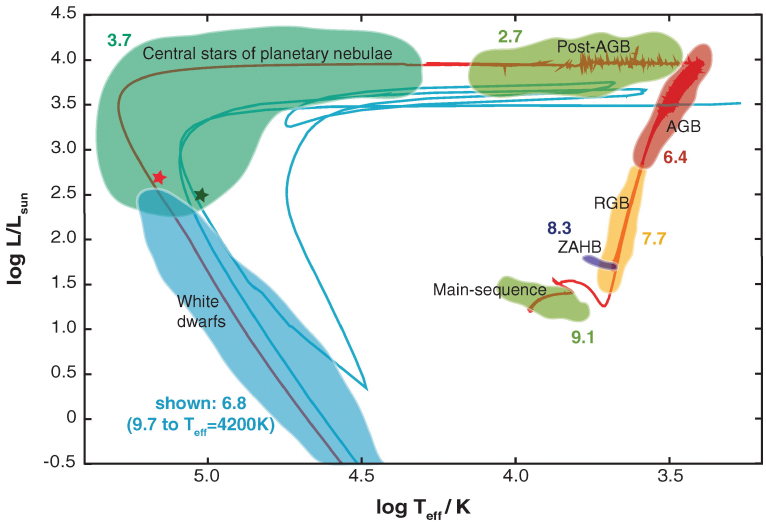

Figure 1.1 *The Hertzsprung-Russell diagram of a $2M_{\odot}$ from the main-sequence to the white dwarf stage. The numbers next to the labeled evolutionary phases indicate the log of the approximate duration of the phase. Larger masses would have smaller timescales, smaller masses larger ones. Taken from Herwig [89].*

Once hydrogen is exhausted in the core it starts to contract and heat up as no more energy is produced by nuclear fusion. The core is now an inert helium core. Hydrogen burning continues in a thin shell around the core leading to the start of the red giant branch (RGB) phase as indicated in Figure 1.1. This phase leads to an expansion of the outer envelope, resulting in a decrease in surface temperature while the luminosity increases in orders of magnitude. Meanwhile, the stellar core keeps contracting and heating as more helium is accumulated by hydrogen burning. When the core temperatures reach 0.2 GK, helium burning begins in the core, and the star moves to the horizontal branch phase in the HR diagram (see ZAHB label in Figure 1.1). This results in a hotter surface temperature and a decrease in the luminosity of the star because the envelope contracts slightly. Helium burning in the star occurs through two processes, the triple alpha process and $^{12}C(\alpha,\gamma)^{16}O$. The triple alpha process consists of 2 steps: First, two alpha particles form short lived ^{8}Be (producing an equilibrium abundance of ^{8}Be in the star), then another alpha particle gets captured on ^{8}Be creating ^{12}C (Phillips [165]). The triple alpha process allows to explain the production of the observed ^{12}C abundances thanks to the presence of a resonance in the $^{8}Be(\alpha,\gamma)^{12}C$ reaction cross section, which greatly enhances the reaction probability. This resonance was predicted by Hoyle et al. [95] and later experimentally confirmed by Dunbar et al.

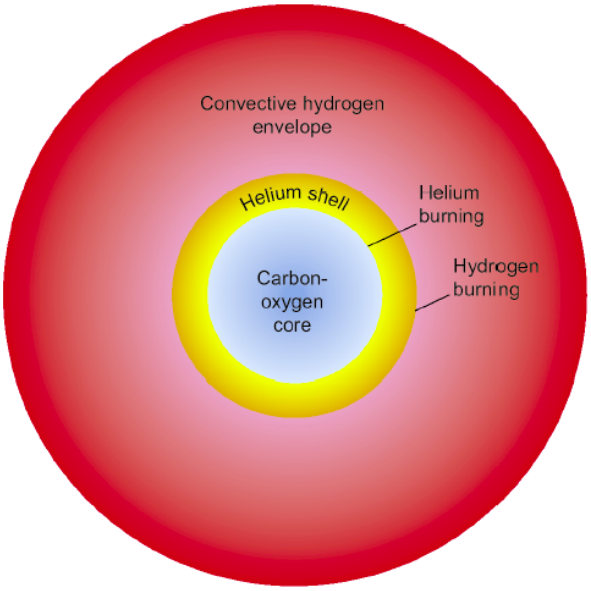

Figure 1.2 *The interior of an AGB star, clearly shown is the convective hydrogen envelope, thin helium shell, and Carbon-Oxygen core. It can be seen where hydrogen and helium burning takes place, at the lower boundary of the envelope and shell respectively. Where Helium burning happens is also the region where the* ^{13}*C-pocket is formed. Not to scale. Taken from Herwig [89].*

[65] and Cook et al. [33] and is thus called the Hoyle state. This process produces about 7 MeV of energy per triple alpha reaction, and typically lasts only 10% of the duration of hydrogen burning.

As helium burning continues, carbon and oxygen begin to collect in the core of the star which contracts and becomes increasingly electron degenerate. Once the helium abundance in the core becomes too low, the star enters the asymptotic giant branch (AGB) phase burning helium in a shell around the core, the star's envelope expands again cooling the surface slightly but gaining a larger increase in luminosity (see Figure 1.1). The stellar structure looks like in Figure 1.2: The core consists of inert carbon and oxygen, a helium rich shell, a hydrogen burning shell and a hydrogen rich convective envelope that is about 250 times larger than the core's diameter. After helium burning, stars with stellar masses above 10 $M_\odot$ can ignite subsequent carbon burning, followed by neon, oxygen and silicon burning which allows the creation of elements up to and including the iron peak (Karakas & Lattanzio [105]). Stars that undergo these processes do not enter the AGB phase.

1.1.1 The Asymptotic Giant Branch Phase

The AGB phase is split into two parts; the early-AGB and the thermally pulsing (TP)-AGB. During the early AGB phase, the helium shell burning dominates nuclear energy production. It burns outward from the core boundary towards the convective hydrogen envelope. The star also temporarily becomes a RGB star again until all the helium in the shell is exhausted (Vassiliadis & Wood [207]). From this point the TP-AGB phase starts, nuclear energy is released primarily from hydrogen burning in a thin shell at the bottom of the hydrogen shell and is interrupted periodically by thermonuclear runaway helium flash events called thermal pulses (TPs). During hydrogen shell burning in the inter-pulse phase (time between TPs), more and more helium is added to the He inter-shell. Eventually, temperature in the inter-shell becomes high enough to start helium burning with a flash, because of the electron degeneracy of the plasma in the inter-shell. During this TP, neutrons at high densities are released by ^{22}Ne(α,n) reactions, where ^{22}Ne is produced by alpha captures on the abundant ^{14}N in the ^{14}N(α,γ)^{18}F(β^+)^{18}O(α,γ)^{22}Ne reaction chain (Cristallo et al. [44, 47]). The TP causes the envelope to expand and cool, halting hydrogen burning in this region. Helium burning is now the dominant energy source.

This pulse driven convective zone (PDCZ) is important for the nuclear production in AGB stars because the highest temperatures for nucleosynthesis are reached at its base ($\sim$3$\times$10^8 K), enabling the ^{22}Ne(α,n) reaction to marginally activate. Also, during the TP material is mixed from the core with the helium shell, thereby adding more ^{12}C and ^{16}O, which terminates helium burning earlier as the mixing leads to a decrease in the helium abundance. Overall, this increases the ^{12}C abundances, which allows the production of ^{13}C via the ^{12}C(p,γ)^{13}N(β^+)^{13}C reaction chain (Cristallo et al. [44], Liu et al. [127]). This will later allow the slow neutron-capture process (s-process) to occur by efficiently releasing neutrons in ^{13}C(α,n) reaction.

Figure 1.3 shows the stellar structure of a MESA (Paxton et al. [159]) model as a function of time in the AGB phase in the form of a Kippenhahn diagram. The evolution is shown from TP 14 to 15 of a 2M$_\odot$ star with Z=0.01. Regions with convection are marked in blue. After thermal pulse 14, the convective envelope reaches past the boundary into the helium shell (this is called third dredge-up (TDU)). This occurs because the envelope expands and cools as the core contracts after the end of a dominant nuclear burning event. At this point, a region rich

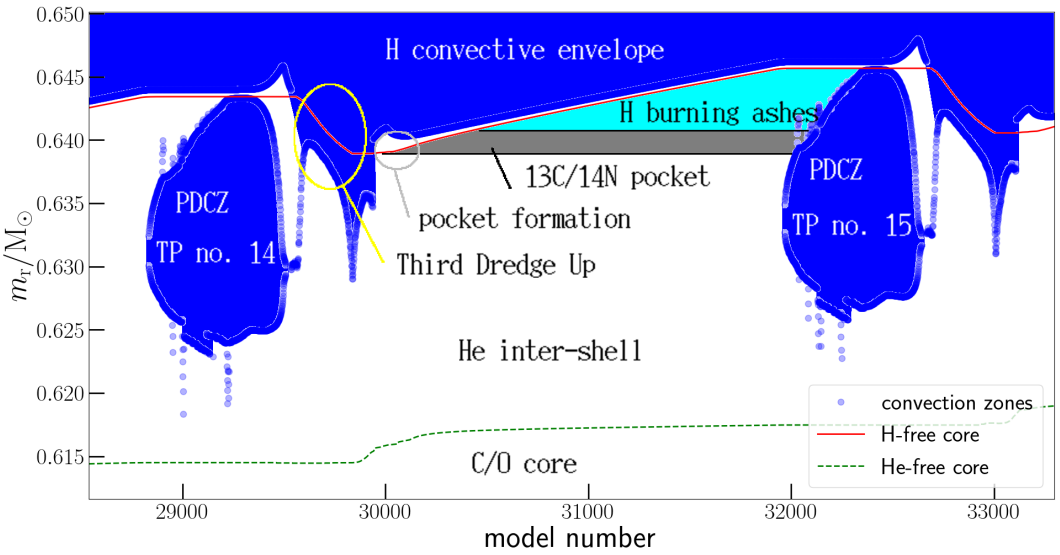

Figure 1.3 *A Kippenhahn diagram from thermal pulse number 14 to 15 of a $3M_\odot$ stellar model with z=0.02, detailing the TDU event introduced by the PDCZ started by the helium flash. The TDU occurs when the Hydrogen envelope penetrates down into the helium inter-shell, taking material from the inter-shell into the convective envelope. The timescale is different per model number. The red solid line indicates the mass coordinate of the H-free core. The dotted blue line shows the boundaries of convection; each dot corresponds to one model in time.*

in ^{13}C (the ^{13}C-pocket) forms below a layer rich in ^{14}N (the ^{14}N-pocket), and the residue of hydrogen burning above the helium shell at the bottom of the envelope. ^{13}C vs ^{14}N abundances are of key importance for the AGB since ^{14}N is an efficient neutron poison, i.e. absorbing neutrons by (n,p) reactions. The ^{13}C-pocket size is defined as the mass coordinate difference between the points where the mass fraction[2] of ^{13}C, X(^{13}C), exceeds 0.001 and X(^{13}C) $\geq$ X(^{14}N). Neutrons are produced by ^{13}C(α,n) reactions over about hundred thousand years with densities of about 10^7 cm^{-3}. Abundances of key isotopes around the mass coordinate of the ^{13}C-pocket are shown in Figure 1.4, for a star of 3 M$_\odot$ and Z=0.02. The 3 panels represent different stages, the top panel shows the TDU at maximum penetration, the middle panel shows the formed ^{13}C-pocket, while the bottom panel shows the situation at a later stage where *s*-process elements have been produced in the pocket.

The TDU also transports newly synthesised elements to the star's surface. These

[2]The mass fraction X within a mixture is the ratio of the mass m_i divided by the total mass m_{tot}, i.e. $X_i=\frac{m_i}{m_{tot}}$

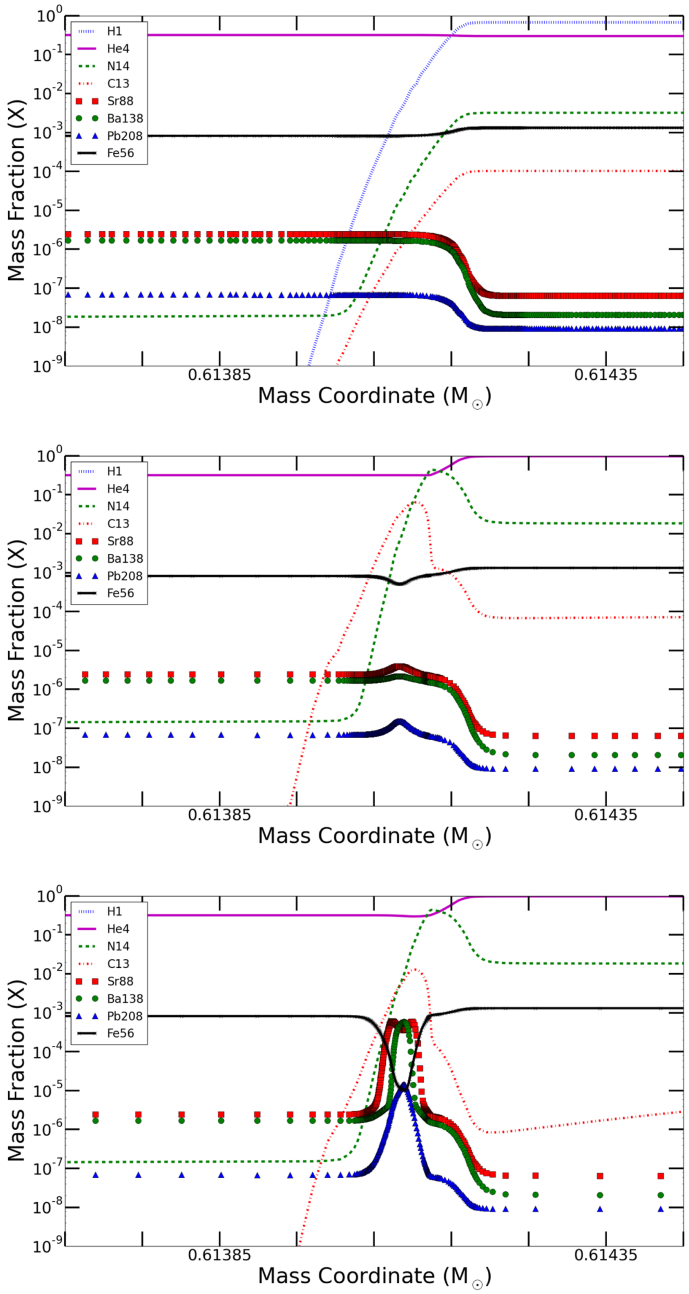

Figure 1.4 *Abundances at different mass coordinates from the center of the star are shown in three different evolutionary steps of* ^{13}C*-pocket in a* $3M_{\odot}$*, z=0.02 stellar model. The top panel displays the moment TDU achieves maximum penetration, which is followed by the radiative burning of the* ^{13}C*-pocket with the consequent neutron release (middle panel) and the s-process nucleosynthesis (bottom panel). Hydrogen and Helium were selected to define the boundaries between the Hydrogen envelope, Helium inter-shell and the CO core.* ^{13}C *and* ^{14}N *are chosen to show the development of the* ^{13}C*-pocket and the* ^{14}N*-pocket directly above.* ^{88}Sr*,* ^{138}Ba *and* ^{208}Pb *are s-process products that lie at the neutron magic peaks. Taken from Battino et al. [11].*

products include CNO cycle products, and products of the main *s*-process. The spectra of low mass AGB stars are indicative of high carbon abundances and unstable elements like technetium, which can only be formed by the *s*-process in AGB stars. In particular the high carbon abundance allows the surface of the star to become opaque to radiation making the material likely to be ejected from the star as stellar wind. Later, the *s*-process material can be encased in silicon carbide if the conditions of the stars atmosphere enable condensation, becoming a silicon carbide grain (Karakas [104], Karakas & Lattanzio [105], Lugaro et al. [138]).

The TPs stop because the envelope is depleted from mass loss through stellar wind that no longer allows hydrogen burning to produce the helium and temperature required for the TP. This ends the TP-AGB and starts the post-AGB phase (see Figure 1.1), noticeable by an increase in temperature (Battino et al. [11], Werner & Herwig [215]).

In the post-AGB phase strong stellar winds lead to the formation of planetary nebula and expose the core. As hotter layers of the stars are exposed the surface temperature rises and the star moves to the left on the HR diagram (see Figure 1.1). The shell of gas around the central star in the nebula heats up remaining as luminous as the AGB phase and post-AGB phase with a hotter surface temperature because of the radiation released from the core, which expands the nebula. Once the star has shed all its envelope, it becomes a white dwarf (see Figure 1.1) gradually cooling in temperature and reducing in luminosity, supported by electron degeneracy (Herwig [89], Rolfs & Rodney [185]). White dwarfs are very dense (10^9 kg/m^3), with sizes typically similar to our Earth, but a mass comparable to our Sun. For intermediate mass stars the white dwarf's composition is mainly carbon and oxygen.

Stars with masses of 1-10$M_\odot$ enter the AGB phases. While their evolutionary path is similar, there are some differences in the AGB phase depending on their stellar mass which leads to differences in their heavy element production. AGB stars can be grouped into 3 sub categories, 1-4 $M_\odot$ (known as low-mass AGB), 4-8 $M_\odot$ (massive AGB), and 8-10 $M_\odot$ (super AGB) (Herwig [89]). Others define the mass ranges differently i.e Cristallo et al. [41], Karakas & Lattanzio [105], Lugaro & Chieffi [134]. Figure 1.5 shows these three groups including some relevant evolutionary stages and their final fate. Low mass AGB stars produce most heavy elements between Zr and Pb by mass, while super AGB stars are less efficient, due to their higher gravity they produce a smaller helium inter-shell resulting in

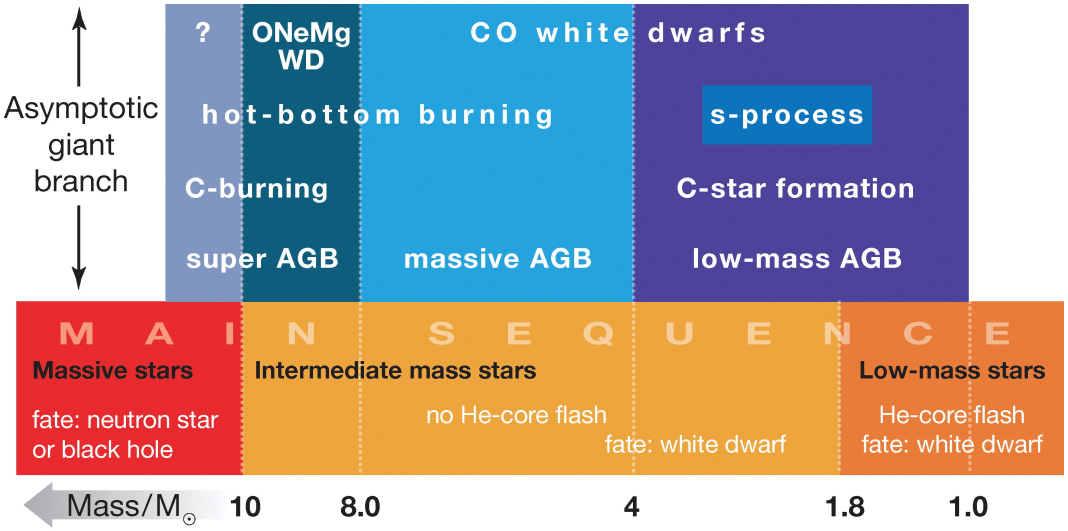

Herwig, F. 2005
Annu. Rev. Astron. Astrophys. 43: 435–79

Figure 1.5 *Diagram showing the different categories by initial mass for the main sequence and the AGB phase for solar metallicity. The final fate and some characteristic evolutionary properties are added. This defines the mass intervals I will describe. The borders are not well defined theoretically, they depend on other factors such as mass loss and mixing, more so for electron-capture supernovae. All values given are estimates and depend heavily on modelling details. Taken from Herwig [89].*

a smaller ^{13}C-pocket (around a factor of 10 smaller than a 2 $M_\odot$ star) (Cristallo et al. [43]). Massive AGB stars are defined by the characteristic of hot-bottom burning, a hydrogen shell burning condition in which the outer part of the shell is included in the envelope convection. In this way, the carbon content in the stellar envelope decreases, as it is exposed to hydrogen burning conditions and transformed into nitrogen by proton captures (Herwig [89], Karakas & Lattanzio [105]). Massive AGB stars rely on the ^{22}Ne(α,n) reaction for the *s*-process and as a result do not produce significant material which is not transported to the surface until late in the evolution (García-Hernández et al. [76]). This thesis will focus on low-mass AGB stars evolved from intermediate mass stars because they are primarily responsible for polluting the Galaxy with new heavy elements, while super AGB and massive AGB stars have a much less efficient *s*-process. However, if massive AGB stars are in a close binary system they may end their lives in a Type Ia Supernova, during which a lot of iron and first *s*-process peak elements are produced (François et al. [71], Yoon & Langer [217]).

1.2 The slow neutron capture process

Chapter 1.1 described the evolution and nucleosynthesis of intermediate mass stars, and it was briefly mentioned how elements up to iron can be formed through nuclear fusion in massive stars, which allows them to maintain hydrostatic equilibrium. Elements heavier than iron are mainly formed by neutron capture processes[3]. Two neutron capture processes can explain most of the heavy element abundances, the *s*-process, and the rapid neutron-capture process (*r*-process).

In the *s*-process neutrons get captured on pre-existing seed nuclei (iron nuclei) forming an isotope with a higher mass. Radioactive beta decays are typically faster than neutron captures, hence unstable isotopes will decay to a new element before the next neutron capture will occur (Käppeler et al. [115]). The *s*-process happens in stellar environments with neutron densities between 10^{7-12} cm^{-3} and lasts for hundred thousands of years (Herwig [89]). The s-process occurs in quiescent environments of stellar interiors, in particular in low mass stars during their AGB phase, and also at the end of core He-burning and during shell C-burning in massive stars. The *r*-process, occurs in explosive astrophysical events, such as neutron star mergers (Côté et al. [52]) at extremely high neutron densities of $>10^{20}$ cm^{-3}. Neutron captures are faster than beta decays, driving the reaction path into the neutron rich region of the nuclide chart (Thielemann et al. [199], Thielemann et al. [201]). Figure 1.6 shows a section of the chart of nuclei and the respective nucleosynthesis path of the *s*-process. There are about 30 proton-rich isotopes, that cannot be explained by either the *s*-process or the *r*-process. These "p-nuclei" are produced in the so-called *p*-process or γ-process. In this process, photodisintegration reactions, i.e. (γ,p), (γ,n) and/or (γ,α) on pre-existing heavy isotopes lead to the production of neutron deficient isotopes. Their abundances are typically two orders of magnitude smaller than isotopes produced in the *s*-process and *r*-process. The stellar site of the *p*-nuclei is an open question, possible candidates are type Ia supernovae and core-collapse supernovae (Travaglio et al. [205]).

In the following, the *s*-process will be explained in more detail. For a review on the *s*-process see e.g. (Herwig [89], Karakas & Lattanzio [105], Straniero et al. [194]). In *s*-process environments, the time dependence of abundance changes in

[3]for heavy elements, charged particle reactions exhibit high Coulomb barriers which make reactions at stellar temperatures very unlikely

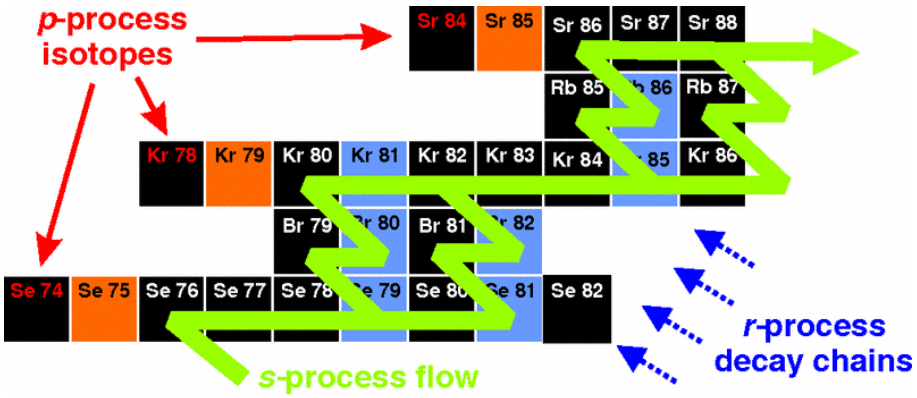

Figure 1.6 *Table of isotopes in the Se-Sr mass region showing the s-process reaction path and nuclei that can only be produced by the p-process. Taken from Dillmann et al. [62]*

stable or very long-lived nuclei can be written as

$$\frac{dY_A}{dt} = Y_{A-1}(t)N_n(t)\langle\sigma\nu\rangle_{A-1} - Y_A(t)N_n(t)\langle\sigma\nu\rangle_A, \tag{1.5}$$

assuming that no other reaction channel contribute significantly (this is justified, since charged particle reactions are extremely unlikely due to the high Coulomb barriers of reactions at high Z). Here Y_A and Y_{A-1} are the abundances of isotopes with mass A and $A-1$ respectively, N_n is the number of neutrons per unit volume. $\langle\sigma\nu\rangle$ is the reaction rate per particle pair, either producing ($\langle\sigma\nu\rangle_{A-1}$) or destroying ($\langle\sigma\nu\rangle_A$) isotope A by neutron capture. $\langle\sigma\nu\rangle$ is defined as

$$\langle\sigma\nu\rangle = \int_0^{\inf} \phi(\nu)\sigma(\nu)\nu d\nu, \tag{1.6}$$

where σ is the reaction cross section as a function of relative thermal velocity, ν is the relative velocity, and $\phi(\nu)d\nu$ is the probability to find a particle with a velocity between ν and $\nu + d\nu$. Stars are in thermal equilibrium, hence particle velocities follow a Maxwell Boltzmann distribution. It is therefore useful to define the Maxwellian averaged cross-section (MACS) as

$$\langle\sigma\rangle = \langle\sigma\nu\rangle/\nu_T. \tag{1.7}$$

Here, ν_T is the most probable velocity in the Maxwell Boltzmann distribution

$$\nu_T = \sqrt{\frac{2k_BT}{\mu}}, \tag{1.8}$$

where k_B is the Boltzmann constant, T is the temperature and μ is the reduced mass. Converting to center of mass energy E, the MACS can then be written as:

$$\langle\sigma\rangle = \frac{2}{\sqrt{\pi}(k_B T)^2}\int_0^\infty \sigma(E) E e^{-\frac{E}{k_B T}} dE. \tag{1.9}$$

Using these considerations, Equation 1.5 can be re-written as

$$\frac{dY_A}{dt} = Y_{A-1}(t)\langle\sigma\rangle_{A-1}\Phi - Y_A(t)\langle\sigma\rangle_A\Phi \tag{1.10}$$

where the neutron flux $\Phi = N_n(t)\nu_T$. For $\frac{dY_A}{dt} = 0$, in steady flow conditions (so-called local equilibrium approximation), Equation 1.5 can be rewritten as,

$$0 = Y_{A-1}\langle\sigma\rangle_{A-1} - Y_A\langle\sigma\rangle_A, \tag{1.11}$$

so both terms in the equation are equal and constant (Pritychenko [172]).

Figure 1.7 shows $Y_A\langle\sigma\rangle_A$ as a function of mass number, where Y_A are solar system abundances of s-only nuclei (i.e. nuclei, that cannot be produced in the r-process). The plot suggests a steady state is reached in the s-process above mass of about 80, between magic neutron numbers[4]. The broken equilibrium at the magic numbers (N=50,82,126), due to their low MACS resulting in a bottleneck in the reaction flow, this leads to abundance peaks in the solar system abundance distribution. This is illustrated in Figure 1.8 which shows the abundances produced in both s-process and r-process. The s-process abundances show three characteristic peaks around Sr, Ba and Pb, often called the first, second and third s-process peaks. Going back to Figure 1.7, there is also a region below mass 80 where steady state is not reached. This indicates that there are different components/stellar sites to the s-process which will be discussed in the following paragraph.

S-process abundances can be explained with two different components, the weak and main components. These components are characterised by different neutron exposures (the neutron exposure is defined as the time-integrated neutron flux (Gallino et al. [75])) and stellar conditions. The weak component occurs in massive stars (mass, $M>10M_\odot$) at the end of helium core burning, and during carbon shell burning, at stellar temperatures around 0.3 GK, and 1 GK, respectively (Pignatari et al. [167], Raiteri et al. [173]). Typical neutron

[4]Neutron magic numbers occur at N=2, 8, 20, 28, 50, 82, 126, and 184. They are arranged into complete shells within the atomic nucleus, as a result the nucleus is much more stable than other non-magic nuclei (Rohlf & Collings [184]).

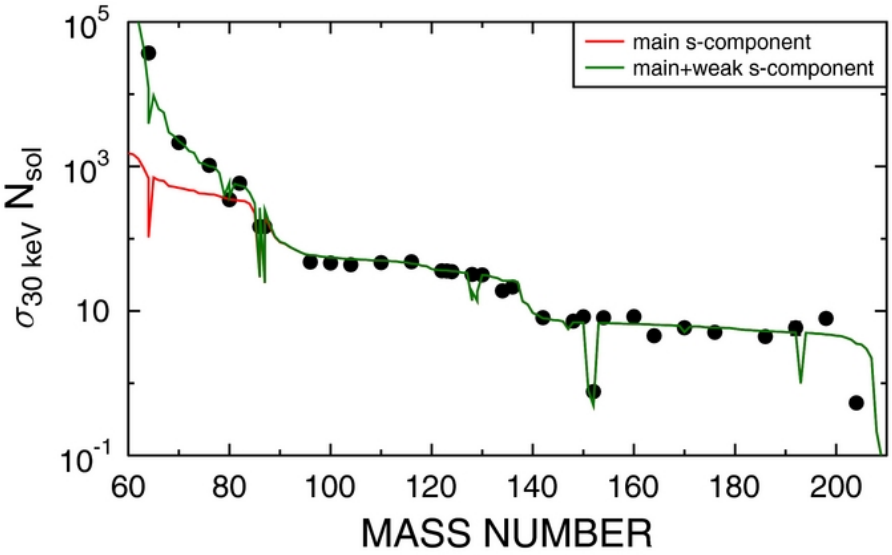

Figure 1.7 *The characteristic product of cross section times s-process abundance plotted as a function of mass number. The red line represents the main component obtained by means of the classical model, and the green line corresponds to the sum of the main and the weak component, the latter taking place in massive stars. Symbols denote the empirical products for the s-only nuclei. Some important branching points of the neutron capture chain are indicated as well. The weak component was assumed for explaining the higher s-process abundances between Fe (A = 56) and Zr (A = 90). Taken from Reifarth et al. [181].*

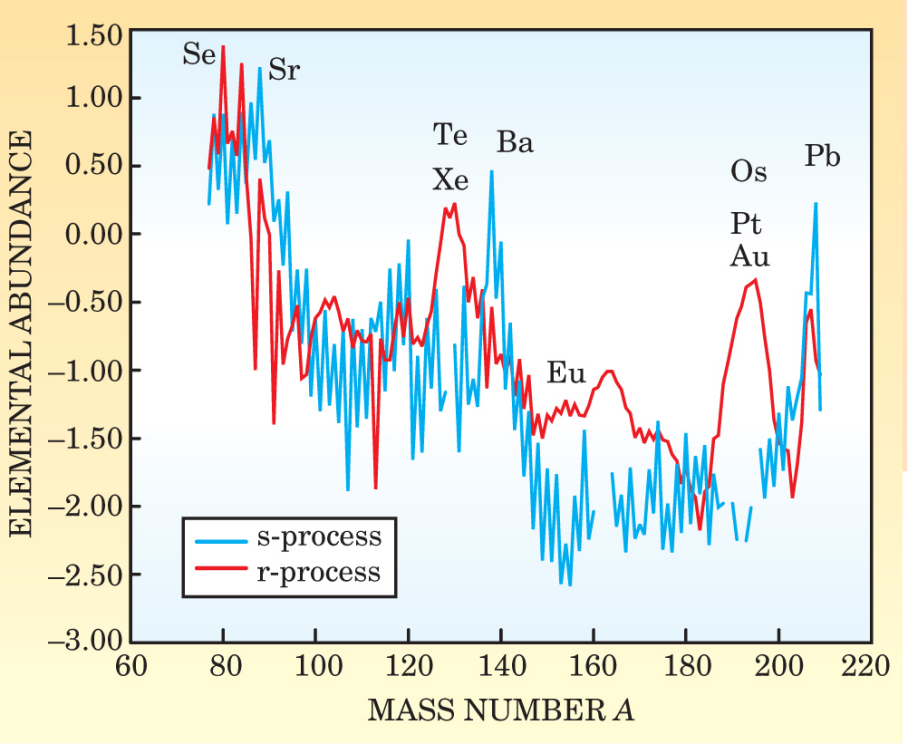

Figure 1.8 *Solar system abundances of heavy elements produced by s-process and r-process. The y-axis values are* $12 + log_{10}(abundance)$ *to make them relative to the hydrogen abundance. Abundance peaks are caused by large* β*-decay half-lives or small neutron capture rates at magic numbers corresponding to full neutron shells. Because the r-process carries nuclei farther from the valley of stability compared with the s-process, it encounters each closed shell at slightly lower mass number. Hence the r-process peaks are offset to lower atomic masses. The curves are not re-normalised because the two processes have contributed near equally to the Solar System's total abundance of heavy elements. Taken from Cowan & Thielemann [38].*

densities are 10^{7-12} cm^{-3} which are produced via the ^{22}Ne(α,n) reactions, however the duration is relatively short (hundreds of years), resulting in a low neutron exposure which does not allow establishing steady flow. Hence, this component produced mainly elements up to and including the first *s*-process peak (Sr, Y, Zr) and its role in synthesising heavier elements is limited (Nishimura et al. [151]).

The main component occurs in intermediate mass stars during their AGB phase. The main component of the *s*-process is responsible for synthesis of heavier elements up to Pb, but predominantly the second peak at: Ba, La, Ce, Pr and Nd. Neutron captures occur on a wide range of seed nuclei, leading to the production of a broad spectrum of heavy elements (Gallino et al. [75], Herwig [89], Lugaro & Chieffi [132]). During the TP, irradiations are too short, and hence neutron exposures are to small to reach steady flow and the overall contribution of this phase to abundances is small. However, the high neutron densities reached can modify individual isotopic abundances particularly around branching point nuclei.

An important role in studying *s*-process nucleosynthesis and its stellar conditions is played by branching point nuclei. Branching points are unstable nuclei where radioactive decays compete with neutron capture, resulting in a "branching" of the *s*-process path. The abundances of the isotopes following in the reaction chain are therefore highly dependent on neutron capture cross sections, neutron densities and decay half lives. If branching points affect isotopic ratios of *s*-only nuclei, neutron densities during the *s*-process can be deduced assuming that half lives, and cross sections are known. Likewise, for branching point nuclei where the stellar decay rate is temperature dependent, the stellar temperature can be determined from a known neutron density (Karakas & Lattanzio [105], Lugaro & Chieffi [132]). However, the measurement of neutron capture cross sections on unstable nuclei is challenging and in many cases not possible at present. As will be demonstrated in Chapters 3 and 4, this may lead to high uncertainties in predictions of certain isotopic abundance ratios from stellar models.

Chapter 2

Modelling stellar evolution and nucleosynthesis

2.1 Introduction

The evolution of a star can be calculated by solving a set of conservation laws, i.e. the conservation of mass, momentum and energy. These laws describe the time variation of a quantity in a given volume, considering their divergence, sources and sinks. For example, for energy conservation (exothermic) nuclear reactions would contribute as a source, while neutrino emission contributes to energy losses, as neutrinos usually escape the star without interacting. The conservation laws, complemented by the appropriate microphysics (for example opacities, equation of state, etc) need to be solved numerically with a high spatial and time resolution, which is challenging due to the vastly different timescales at work in a star (nuclear, thermal and dynamical). At present it is only possible to simulate small sections of a star of a limited evolutionary stage in 3 dimensions (for example one burning stage). For full stellar models, it is common to assume spherical symmetry and perform calculations in 1D. This is a reasonable assumption since, even in case of e.g. fast rotating stars, at least 80% of the inner mass of the star are spherically symmetric (Kippenhahn et al. [108], Pols [171]). On the other hand, this means that 3 dimensional processes such as turbulences need to be parameterised for 1D calculations. There are also 2D models, however these have been found to have issues with reliably recreating the same results of 3D simulations for specific mixing problems, e.g. turbulence (Busso et al.

[22], Edelmann et al. [67]).

A common approach also used in this thesis to calculate the nucleosynthesis of a particular stellar model is post-processing. The stellar structure evolution is calculated using the smallest possible network large enough to accurately calculate the nuclear energy generation. The stellar structure from the stellar model is then used as an input to a post-processing code, that includes the entire nuclear reaction network and calculates the produced/destroyed abundances in each zone of the star. The decoupling of stellar evolution and nucleosynthesis calculations allows to study the impact of reaction rate changes quicker, without having to re-calculate the entire stellar structure. This provides a definite speed advantage compared to fully coupled stellar evolution code calculations when modelling physical processes.

2.2 Stellar evolution models with MESA

The stellar models used for post-processing in this thesis were calculated with the open source code MESA (http://mesa.sourceforge.net). MESA stands for Modules for Experiments in Stellar Astrophysics and includes a 1D stellar evolution code MESA star for stellar evolution calculations of very low mass to massive stars. MESA has separate modules for physics and numerical algorithms with the ability to be used as a stand alone program, and it will run on a PC or multi-core architectures. The code includes comprehensive micro-physics and modern techniques like opacity and adaptive mesh refinement for mixing in stars, respectively (Pignatari et al. [169], Rees et al. [178]). A detailed description is given in Paxton et al. [159], Paxton et al. [160], Paxton et al. [161], Paxton et al. [162] and Paxton et al. [163]. The models considered in this thesis (Battino et al. [13]) were calculated with MESA revision 3709, but with a modified description of mixing (see Section 2.2.1). The output from a MESA stellar evolution model contains a wealth of information, for example temperature, density and pressure as a function of mass coordinate (these are referred to as zones) and time (the evolution is divided in time steps, which depend on the timescales/time resolution needed). As an example, a 3 $M_{\odot}$ star with a metallicity of Z=0.02 would have 76000 time steps and 2000 zones for the asymptotic giant branch (AGB) phase alone. For the evolution up the AGB phase, between 700 and 1400 zones are sufficient. An additional parameter included for each mass coordinate is the mixing profile indicator, which identifies if the mass coordinate is outside (0),

in (1), or near (2) a convective zone. MESA uses mixing length theory (MLT) to calculate mixing coefficients, D(r) for each zone to represent the convective volume in the stellar model as a diffusive process (Böhm-Vitense [18], Paxton et al. [159], Vitense [210]).

In addition to MESA, many other 1D stellar modelling codes exist. These include GENEC (Eggenberger et al. [68]), FRANEC (Limongi & Chieffi [125]), STARS (Eggleton et al. [69]), COLIBRI (Marigo et al. [145]), STAREVOL (Decressin et al. [54]), FUNS (Cristallo et al. [45]) and MSSSP (Karakas & Lattanzio [103]). The AGB phase is sometimes also modelled using so-called synthetic models, which means that the evolution from pulse to pulse is described with a parameterisation that produces the results of a full model. In some cases synthetic models can reproduce observations quantitatively better because they are calibrated to them, and they are faster to calculate. However, synthetic models cannot be extrapolated into regimes that have not yet been explored in detail with stellar evolution models. For that reason, synthetic modelling is not currently applicable to extremely low or zero metallicity models (Goriely & Siess [79], Herwig [88, 89]). An example of synthetic models is given in the work of Marigo [142], Marigo et al. [143, 144]. There are also hybrid approaches such as COLIBRI where the hydrogen envelope is simulated in a similar way to a stellar model but the interior is calculated using a synthetic model.

2.2.1 Modification of mesa for IGW mixing

Chapter 3 will present results from post-processing nucleosynthesis calculations of models that had been calculated in MESA with a modified description of mixing (Battino et al. [10, 11, 13]). Therefore, it is worth detailing in this chapter the specific adjustments that have been made to the mixing implementation of MESA for the AGB evolutionary stage. A realistic description of convective boundary mixing (CBM) processes in AGB stars is essential for slow neutron-capture process (s-process) nucleosynthesis calculations. The CBM at the bottom of the convective envelope of the star during the third dredge-up (TDU) allows formation of the ^{13}C-pocket, since it allows hydrogen rich material to diffuse into the carbon rich helium inter-shell. Mixing at convective boundaries are multi-dimensional processes which need to be parameterised for 1D models. This leads to significant uncertainties due to the unknown exact mixing scenarios (many have been proposed, such as semi-convection (Iben & Renzini [96], Langer et al.

[118], Lawlor & MacDonald [120]), overshooting (Herwig [87], Herwig et al. [90]), magnetic buoyancy (Busso et al. [23], Nucci & Busso [153], Trippella et al. [206]), etc.), and uncertainties in their implementation in 1D models have been discussed. For further discussion see for example Battino et al. [10, 11, 13], Blouin et al. [17], Cristallo et al. [42, 43], Herwig et al. [92], Karakas [104], Karakas & Lugaro [106], Lugaro et al. [139], Palmerini et al. [158], Ritter et al. [183], Vescovi [208].

Mixing during the TDUs of the AGB phase was modified in the following way in MESA models (Battino et al. [10, 11, 13]): MESA implements a CBM model with exponentially decaying diffusion coefficient, D (Freytag et al. [72], Herwig et al. [90]):

$$D_{cbm}(z) = D_0 \exp\left[\frac{-2z}{f_1 H_{P0}}\right]. \tag{2.1}$$

Where z is the distance from the convective boundary, D_0 and H_{P0} are the diffusion coefficient and the pressure scale height at the Schwarzschild boundary[1], respectively. f_1 defines the slope of D (see Figure 2.1). This overshooting profile is likely caused by Kelvin Helmholtz instabilities (Battino et al. [11], Casanova et al. [26]), which are fluid instabilities that occur when there is velocity shear in a single continuous fluid or a velocity difference across the interface between two fluids. $f_1 H_{P0}$ is the scale height that determines the decay of the diffusion coefficient further away from the convective boundary. H_{P0} is taken at the Schwarzschild boundary, the point in space that across which, if one applies the Schwarzschild criterion for convection, the plasma changes from being stable to unstable against convection. It is applied across the whole overshooting zone (Battino et al. [11], Herwig et al. [90], Kamath et al. [102], Karakas [104], Karakas & Lugaro [106], Lugaro et al. [137]). Equation 2.1 describes the rapid decrease in mixing efficiency at the convective boundary. Multi-dimensional simulations of the stellar interiors indicate that a second, shallower, exponential decay needs to be added to describe mixing below the pulse driven convective zone (PDCZ) (Herwig et al. [90], Herwig et al. [92]). This CBM method is applied to both the boundaries of the helium inter-shell while the above region is experiencing convection and the region below the boundary is non-convective. This new CBM implementation involves adding this second exponential that starts as soon as the mixing coefficient drops under a value of D_2 given by:

$$D_2 = D_0 \exp\left[\frac{-2z_2}{f_1 H_{P0}}\right] \tag{2.2}$$

[1]The Schwarzschild criterion predicts convection if the radiative temperature gradient exceeds the adiabatic temperature gradient.

which is adopted for distances of $z \leq z_2$. When including Equation 2.1, the diffusion coefficient for CBM in the range $z > z_2$ is described by:

$$D_{cbm}(z) = D_2 \exp\left[\frac{-2(z - z_2)}{f_2 H_{P0}}\right]. \tag{2.3}$$

The new implementation can be defined by the three parameters: f_1, f_2, and D_2, where f_1 still defines the first slope likely caused by Kelvin-Helmholtz instability. f_2 is the slope due to the internal gravity wave (IGW) mixing mechanism (Battino et al. [10, 11]). For a complete diagram showing the configuration see Figure 2.1 and for values used refer to Battino et al. [13]. For the stellar models used in the study, stronger material transport occurs further from the convective boundary than in previous stellar models, this leads to the formation of a larger ^{13}C-pocket. In Chapter 3 stellar models will be presented where CBM is increased to the upper limit of the uncertainty given in Denissenkov & Tout [59]. It should also be noted that the implementation of IGW mixing described here originates in a mathematical derivation taking the initial conditions from a stellar model of $3M_\odot$, Z=0.02 and a possible mass and metallicity dependence of the diffusion coefficient has not been considered in the stellar models discussed here.

2.2.2 Modification of mesa for pseudo-rotational mixing

The ratio of abundances at the second *s*-process peak around Ba (hs) and the first *s*-process peak around Sr (ls) observed in stars shows a spread in values, in particular ratios are $-0.6 <$ [hs/ls] < 0.0 for solar metallicity stars (Busso et al. [21], for a definition of bracket notation see Chapter 3.2). Stellar models applying CBM to the bottom of the helium inter-shell during thermal pulses (TPs) will only reproduce the largest observed [hs/ls] ratios, suggesting that these models reproduce the maximum observed neutron exposures (Herwig [89], Lugaro et al. [136]).

The lower [hs/ls] values could possibly be explained by additional mixing due to stellar rotation (Herwig et al. [93], Piersanti et al. [166], Siess et al. [188]). In general, shear mixing is caused by the velocity difference between a fast rotating core making contact with a slower rotating envelope during the AGB phase. As a result, shear mixing begins during the inter-pulse period diluting the ^{13}C-pocket with ^{14}N, the dominant neutron poison from the ^{14}N-pocket situated above. This reduces the available neutrons for the *s*-process, directly affecting the

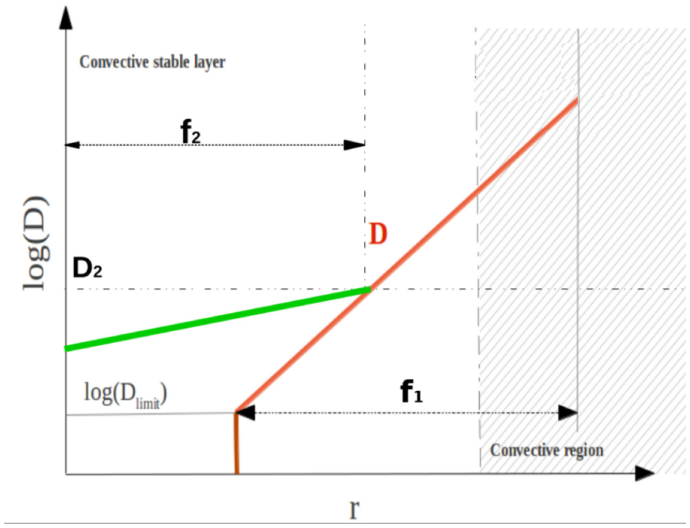

Figure 2.1 *Schematic describing the double-exponential of CBM. The red line represents the standard overshooting profile presented in Herwig et al. [90], this profile is dominated by the f_1 parameter, which determines the slope of the profile. The lower the value of f_1, the steeper the profile. The green line represents the second exponential decay profile, this becomes more relevant than overshoot when the mixing coefficient is equal to or lower than the D_2 value. Again the steepness of the slope is determined by f_2. r is the radial coordinate of the star, the diagram is not to scale and adapted from Battino et al. [11].*

neutron/seed ratio, thus reducing barium-peak production. Rotation, a stochastic process, presents a variable interaction, where a range of initial angular velocities are observed galactically. This mechanism could explain the span of *s*-process efficiencies observed through spectroscopic data and laboratory measurements of some isotopic ratios in pre-solar grains (Battino et al. [11]). Shear mixing can be induced by several different types of instabilities acting on different timescales. Examples are the Solberg-Høiland instability (Wasiutynski [214]), Dynamical shear instability (Chandrasekhar [30], Endal & Sofia [70], Zahn [218]), Secular shear instability (Endal & Sofia [70], Richard & Zahn [182], Zahn [218]), Eddington-Sweet circulation (Eddington [66], Kippenhahn [107], Sweet [195], von Zeipel [211]), Goldreich-Schubert-Fricke instability (Fricke [73], Goldreich & Schubert [77]), ABCD-instability (Spruit et al. [190]), or the triple diffusive instability (Knobloch & Spruit [109]). However, for the two latter instabilities, there are no reliable estimates as to their efficiencies (Heger et al. [81]). In addition to rotation there are also other mixing processes which may explain the observed spread in [hs/ls] values, for example magnetic dynamos (Braithwaite & Spruit [19], Braithwaite, J. [20], Cowling [39], Palmerini et al. [158], Vescovi [208], Vescovi et al. [209]).

In this thesis, the consequences of shear mixing are investigated using a simplified parameterisation, without describing the instabilities above separately. The effect of rotation on *s*-process nucleosynthesis is simulated by introducing a small amount of diffusion across the star similar to the approach of Herwig et al. [93] (Battino [9]). This only impacts on the nucleosynthesis in the inter-shell, because nothing is burning in the core and the envelope is dominated by convection. This parametric diffusion method differs from the method of others as they try to self-consistently simulate rotation, by including all other effects on the stellar structure (den Hartogh et al. [56, 57], Piersanti et al. [166]). The study by Herwig et al. [93] predicts a mixing coefficient of around $\log(\mathrm{D}[\mathrm{cm}^2\mathrm{s}^{-1}])\sim 2$ which would eventually lead to no *s*-process production due to excessive mixing of ^{14}N into the ^{13}C pocket. This calculation is based on models of rotating stars which only account for conservation of angular momentum. However, these models fail to predict observed rotational velocities, indeed they predict 10-1000 times faster rotation then obtained from asteroseismology measurements (Cantiello et al. [24]). The shear mixing coefficient is dependent on the square of the vertical velocity gradient (Maeder & Meynet [140], Mathis et al. [147], Zahn [219]). The core rotational velocity v_{core} is faster than the envelope velocity, i.e. $\mathrm{v}_{core} \sim \mathrm{C} \times \mathrm{v}_{env}$, with C approximately between 2 and 4 (Deheuvels et al. [55]). Hence D_{rot} is

proportional to:

$$\begin{aligned} D_{rot} \propto (dv/dr)^2 \sim ((v_{core} - v_{env})/(\delta(r)))^2 \\ \sim ((C-1)/C)^2((v_{core})/\delta(r)))^2. \end{aligned} \tag{2.4}$$

Using this approximation, the rotational mixing coefficient D_{rot} can be reduced by a factor 10^2-10^6 to account for the observed rotational velocities, hence -4 $\leq \log(D_{rot})(cm^2s^{-1}) \leq 0$. Six stellar models were calculated (indicated by the "-rotmix" suffix, see Table 3.1) using diffusion coefficients in the range defined above. It should be noted that this parameterisation is a major assumption and the efficiency of rotation as a mixing process is still under debate (Deheuvels et al. [55], den Hartogh et al. [56], Herwig [89], Straniero et al. [192]).

2.3 NuPPN's multi-zone post-processing suite, mppnp

The post-processing suite NuPPN (Pignatari et al. [169]) developed by the NuGrid Collaboration [nugrid.github.io] enables nucleosynthesis calculations for a single zone (PPN) or multiple zones (MPPNP). PPN calculates nucleosynthesis in one zone, using either a set time, constant temperature and density, or a trajectory (time dependent temperature and density). This approach is for example valid during ^{13}C-pocket burning, where no mixing occurs. The multi-zone driver MPPNP allows network calculations over several zones in the star, and allows for mixing material between the zones. Therefore, it provides the most realistic nucleosynthesis outputs. MPPNP, PPN use the same physics and solver packages. It is used to calculate the nucleosynthesis during the core collapse of a supernova where mixing processes are negligible over explosive nucleosynthesis timescales. In this thesis, nucleosynthesis results presented in Chapter 3 have been performed using MPPNP, while in Chapter 4 both PPN and MPPNP were used to estimate the uncertainties of surface abundances and stellar yields due to nuclear reaction rate uncertainties. Since PPN is essentially the same as MPPNP but with only one zone, the following sections will focus on a description of the MPPNP code.

MPPNP uses output files from the MESA stellar evolution code as an input. Reactions and decays of all stable isotopes plus unstable isotopes with half-

lives down to half a second were included in the calculations, any others were excluded. The stellar structure evolution is calculated using the smallest possible network large enough to accurately calculate the nuclear energy generation. For post-processing to work, the stellar evolution code needs to include an energy generation nuclear network using the same data sources as the full nuclear network used for post-processing. Post-processing offers many advantages, most notable are better flexibility and shorter computing times compared to fully coupled calculations. It allows to quickly switch between nuclear reaction rates to test their impact on nucleosynthesis without having to re-calculate the stellar structure, as long as these reaction rates are not important for nuclear energy generation. NuGrid's NuPPN modular2 branch provides a framework for performing both single-zone (PPN) and multi-zone parallel (MPPNP) simulations for specific inputs (Herwig et al. [91], Pignatari & Herwig [168]). The name modular2 refers to a major upgrade to the master branch version of MPPNP, where individual programs within NuPPN have been separated into specific modules for the program to call, this will aide implementing future updates. In addition, the solving method is upgraded (see Section 2.3.3) and the physics package includes an update to the electron screening method. The modular2 version is used in Chapter 4 and the master branch was retained for Chapter 3 to maintain consistency with the results of Ritter et al. [183].

The consistency between stellar evolution and post-processing network is checked by MPPNP through a comparison of abundance profiles for key isotopes from both cases, and generally show good agreement (Pignatari et al. [169]). This is illustrated in Figure 2.2, which shows a comparison of mass fraction of key isotopes as a function of mass coordinate for a 2 solar mass star. The ^{12}C abundance in the helium inter-shell and hydrogen burning ashes agree well indicating both scenarios are treated consistently between the stellar evolution and post-processing methods. The ^{14}N abundances agree for hydrogen burning ashes, hinting at a consistent treatment of the Bethe-Weizsäcker cycle (also known as the CNO cycle) burning. ^{14}N is key in this situation as it has a small proton capture cross section and represents a bottleneck in the reaction flow. On the other hand, the discrepancy between MESA and MPPNP for ^{14}N in the helium burning layers ($0.540 < m_r/M_\odot < 0.567$) is not a concern. ^{14}N is not consumed in helium burning and MPPNP is considered correct because of its more extensive nuclear network. This inconsistency is introduced because MESA uses a coupled solver and MPPNP does not as it solves mixing and nucleosynthesis separately. The only solution to this is to monitor the results as seen in Figure 2.2 with

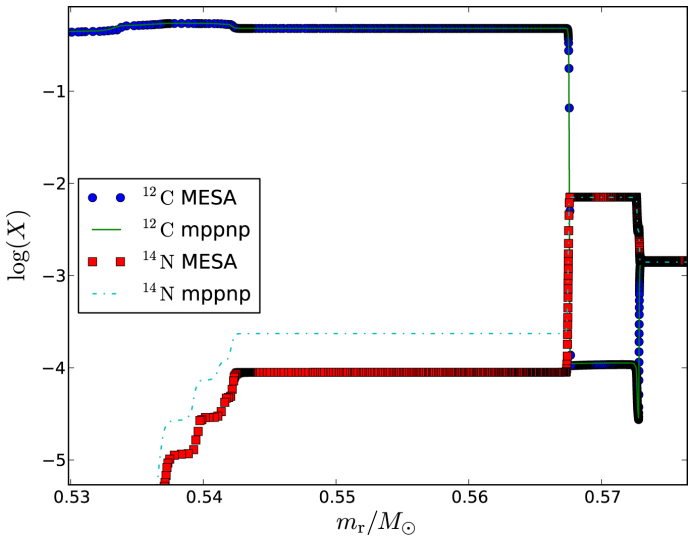

Figure 2.2 *Comparison of* MESA *and* MPPNP *abundance profiles for the 14^{th} thermal pulse convection zone of a $2M_\odot$, $Z = 0.02$ stellar model AGB sequence from Pignatari et al. [169]. In order from left to right, the mass range shown includes the top of the C/O core, the helium shell convection zone, the now extinct hydrogen burning shell, and the bottom of the convective envelope. The H-free core mass is 0.572 m_r / $M_\odot$ for that model. Taken from Pignatari et al. [169].*

abundance profile comparisons and if they escalate MPPNP can force sub-time steps. This has not been used for the models presented in this work, because they have a sufficiently high resolution to prevent this.

2.3.1 Parallel-programming

MPPNP employs Message-Passing Interface (MPI) parallel programming, were a group of processors the "workers" are controlled by a "master" processor. The advantage of MPI is the ability to utilise cluster networks. The master organises the basic operations; initialising, inputs, outputs, and the assignment of tasks to workers, using a first come first serve scheduler. The workers perform the calculations then return the results to the master. For MPPNP, the tasks performed are nuclear network calculations for a zone (a single spherical shell) per a time step. The process is initiated by passing data containing temperature, pressure, etc. for one zone to a worker, this happens for multiple zones per one time step, this is possible because zones are independent of other zones meaning workers do not need to communicate with each other. The work structure allows for a basic parallel implementation, promoting simple and fast

calculations, supporting this is a reduced amount of communication between the master and workers. MPPNP load balances work very well because MESA orders zones spatially, and MPPNP starts calculations of time steps from the centre through to the surface of the stellar model. This cycle is chosen since the higher temperature zones, close to the core, require the longest time to calculate and are therefore allocated to workers first (Pignatari et al. [169]).

The procedure of operation MPPNP adopts is as follows; firstly, the master performs an initialisation of the program. This loads the key data; the reaction rate list, input parameters and the first time step from the stellar model data. The data collected for the nuclear network are broadcast to all the workers, so they have their own private copy. The next step is to activate the scheduler and process the first time step. All workers are assigned calculations while the master awaits a reply notifying it of the completion of all tasks. When this notification is received the workers return the results of the tasks and write the data to file. The master will assign more tasks to the workers and await a reply, this will happen until all tasks for the first time step are complete, triggering a termination message signalling all tasks are complete to the workers. The master will then perform basic tasks, for example a mixing stage (only if the convection indicator is larger than zero). MPPNP reads the mixing coefficients calculated by MESA to recreate the convective volume for the abundance calculation. Mixing is solved with a diffusion calculation that is independent of the nuclear network calculation using the diffusion coefficient D(r) from the stellar structure calculation of MESA. During the next time step, the master re-schedules tasks and the procedure is repeated (Pignatari et al. [169]).

2.3.2 Physics Package

The physics package included in NuPPN provides the full list of isotopes and the reactions they can undergo. For all these reactions, the reaction rates/Maxwellian averaged cross sections are given as a function of stellar temperature, and radioactive decays as a function of stellar temperature and density are available. Reverse reactions are calculated using the detailed balance principle. The package ensures that the correct new reaction rates are used, according to the physical conditions detailed for each zone in each time-step.

The isotopes included in the network are defined by the database files and input parameters; this includes parameters the user can set, such as the maximum

number of isotopes in the network, and a lower limit for the half life of unstable species considered in the network. This feature is useful for speeding up calculations, for example the *s*-process does not involve reactions with nuclei far from stability, in contrast to nucleosynthesis processes in explosive environments.

Not relevant to AGB nucleosynthesis, but for temperatures above 6 GK, nuclear statistical equilibrium (NSE)[2] is assumed. Temperature-dependent partition function and mass excess are given by the REACLIB revision used for the simulations. The electron screening correction applies the method from Chugunov et al. [31]. The NSE implementation uses a Cash–Karp Runge–Kutta integration (Cash & Karp [27], Jones et al. [101]). Isomer states of isotopes can be considered by using the isomer module included. Ground states and long lived isomers are considered separately.

The nuclear reaction rate network

The nuclear reaction network available in NuPPN contains several libraries of recommended stellar reaction rates / cross sections, as well as weak interactions and radioactive decay half lives. The libraries available are:

- REACLIB (JINA (Cyburt et al. [51]) and Basel versions (also, called NON-SMOKER Rauscher & Thielemann [176])): charged particle and neutron induced reaction rates for stellar temperatures up to 10 GK, which can be calculated from seven parameters provided using the parameterisation by Thielemann et al. [200],
- Karlsruhe Astrophysical Database of Nucleosynthesis in Stars (KADoNiS) (Dillmann et al. [63]): compilation of experimental and theoretical Maxwellian averaged neutron capture cross sections for kT values between 5 keV and 100 keV,
- NACRE (Angulo et al. [4]): theoretical and experimental proton and alpha particle capture reactions for all isotopes between ^{1}H and ^{28}Si. Reaction rates for temperatures up to 10 GK with a high and low limit for the uncertainty.

[2] the balance between nuclei that are unstable and emitting particles against the nuclides absorbing the particles, such that the ratios between nuclides (i.e., a specific nuclear species) is preserved over time.

- CF88 (Caughlan & Fowler [28]): evaluated reaction rates based on experimental and theoretical information and as a function of temperature (0.001 to 10 GK) for charged particle reactions and some neutron capture reactions for isotopes of a proton number 1 to 14,

- Iliadis et al. [98]: evaluated reaction rates based on experimental information and theory for proton-induced reactions for 26 stable and 29 unstable nuclei in the atomic mass region of 20 to 40 for temperatures 0.01 to 10.0 GK (for reaction rate uncertainties see Thompson & Iliadis [202]),

- Fuller et al. [74]: experimental and theoretically determined weak interactions of leptons with neutrons up to ^{60}Zn for energies up to 100 GK,

- Oda et al. [154]: compilation of weak interactions; experimental electron and positron capture and decay reactions for hydrogen to potassium in the temperature range 0.01 to 30 GK,

- Goriely [78]: compilation of experimental and theoretical reaction rates for rapid neutron-capture process (r-process), they include (n,γ), (γ,α), electron and positron emission and capture. Useful to the s-process are the electron and positron emission rates which were merged from Takahashi & Yokoi [198]. For $26 \leq Z \leq 83$, and $59 \leq A \leq 210$ in the temperature range of 0.05 to 0.5 GK, typical for AGB nucleosynthesis, and

- Langanke & Martínez-Pinedo [117]: compilation of weak rates: electron capture, positron capture and beta-decay rates on more than 100 nuclei in the mass range A = 45 to 65 for temperature, T = 1 to 10 GK.

The reaction rate network used in this work takes most reaction rates from JINA REACLIB, NACRE, CF88 for charged particle reactions, and Goriely [78] for beta decays. For stellar neutron capture reaction rates, which are most relevant in this work, the Kadonis database v0.3 was used in most cases. Kadonis v0.3 was released in 2006 and is the latest release of the Kadonis compilation. Therefore, some of the recommended Maxwellian averaged cross sections are out of date, and improved data have become available in the meantime. The following MACS values were updated with respect to the Kadonis v0.3 recommendation: ^{20,21,22}Ne (Heil et al. [85]), ^{23}Na (Heil et al. [84]), ^{24,25,26}Mg (Massimi et al. [146]), ^{37}Cl (Guber et al. [80]), ^{45}Sc (Heil et al. [82]), ^{54}Fe (Coquard et al. [34]), ^{58}Ni (Žugec et al. [212]), ^{60}Ni (Corvi et al. [35]), ^{62}Ni (Lederer et al. [122]), ^{63}Ni (Lederer et al. [121]), ^{79,81}Br and ^{85,87}Rb (Heil et al. [83]), ^{80,82,83,84,86}Kr (Mutti et al.

[150]), ^{90,91,92,93,94,95,96}Zr (Lugaro et al. [139]), ^{116,120}Sn were taken from Bao et al. [7] and scaled to values from Koehler et al. [113], ^{152}Sm (Wisshak et al. [216]), ^{151,153}Eu (Best et al. [14]), ^{184,186}W (Marganiec et al. [141]), ^{185}W (Mohr et al. [149]), ^{204}Pb (Domingo-Pardo et al. [64]). There is a new version of Kadonis under development, Kadonis v1.0 (Reifarth [179]). This version is accessible online, but has not been released yet.

2.3.3 Solver Package

MPPNP calculates the abundance change of a specific isotope i, in a zone of a star by adding all nuclear production and destruction channels, such as reactions and radioactive decays. In a general form, the abundance change of isotope i, $\frac{dN_i}{dt}$, can be written as (Iliadis [97]):

$$\begin{aligned}\frac{dN_i}{dt} = &\left[\sum_{j,k} N_j N_k \langle\sigma\nu\rangle_{jk\to i} + \sum_{l} \lambda_{\beta,l\to i} N_l\right] \\ &- \left[\sum_{n} N_n N_i \langle\sigma\nu\rangle_{ni} + \sum_{o} \lambda_{\beta,i\to o} N_i\right]\end{aligned} \tag{2.5}$$

Here the first line represents production, and the second line destruction channels. The first term of the first line represents a sum over all reactions of isotopes $j+k$ leading to production of i, the second term represents radioactive decays of all isotopes l producing isotope i. The second line describes the equivalent for the destruction processes. $\langle\sigma\nu\rangle$ (already introduced in Chapter 1) is the reaction rate, λ_β is the beta decay constant. Photo disintegration reactions are negligible in AGB nucleosynthesis so were removed from this network.

To calculate abundance changes, the set of coupled differential equations for all isotopes i has to be solved. In case of MPPNP, this needs to be done for the amount of zones the model contains, thus parallel programming is essential to resolve the network in a timely manner. Initially the MPPNP code (master branch used for the stellar models) used the backward-Euler method (Bader & Deuflhard [6], Deuflhard [60], Longland et al. [131], Pignatari et al. [169], Timmes [203]). This has been used for results obtained in Chapter 3. Recently, a new version (modular 2) has been released implementing a superior solving algorithm, i.e. the Bader-Deuflhard (BD) time integration method (Bader & Deuflhard [6], Deuflhard [60], Jones et al. [101], Timmes [203]). This method has been used for results obtained

in Chapter 4. Time steps are adaptive for both the backward-Euler and the BD integration methods. They both use a dynamic nuclear network, this implies the size of the network can automatically grow to the required conditions. For example, when neutrons are produced in an AGB star the network will expand to include all isotopes and their reactions with a half life higher than the set threshold. This feature ensures that no reactions are missed, so any production or depletion of all isotopes are recorded.

The BD method facilitates high accuracy calculations with computational efficiency resulting in faster and improved results compared to the backward-Euler method. This is demonstrated in Figure 2.3, which shows the hydrogen mass fraction as a function of time for a hydrogen burning calculation. The different symbols and lines represent the number of time steps in each calculation, while the colours refer to either the semi-implicit extrapolation (BD method, red) or the backward Euler approach (grey). The BD method converges at around 4000 yrs, irrespective of the number of time steps. In contrast, while the backward Euler method would be considered converged in all cases (convergence for 38 time steps not visible on the plot), the same accuracy compared to BD can only be reached for a much higher number of time steps. The backward-Euler method can work well when the results can be checked against a more robust method and no deviations in time step sizes are found, this is something that can be done with MPPNP as time steps are handled by MESA, however this comes at the expense of computational efficiency. Also, MESA calculates some light isotope abundances for the energy generation of the star. So, isotopic abundance results exist in the MESA output and can be used as a reference and cross checked with MPPNP. The MESA calculation verifies the validity of the master branch results so there is no issue with those results shown in Chapter 3.

2.4 Stellar Yield Calculations using NuGridPy

Stellar yields are defined as the material lost from a star through its life. For low mass stars, mass loss occurs through stellar winds, most prominently during the AGB phase. Like surface abundances, stellar yields are enriched in *s*-process rich material produced in the stellar interiors, due to mixing processes during the TPs and TDUs. The abundance composition on the stellar surface and thus the ejected material is determined by the implementation of mixing in MPPNP, this is handled in MESA using the mixing length theory described in Cox & Giuli [40] and

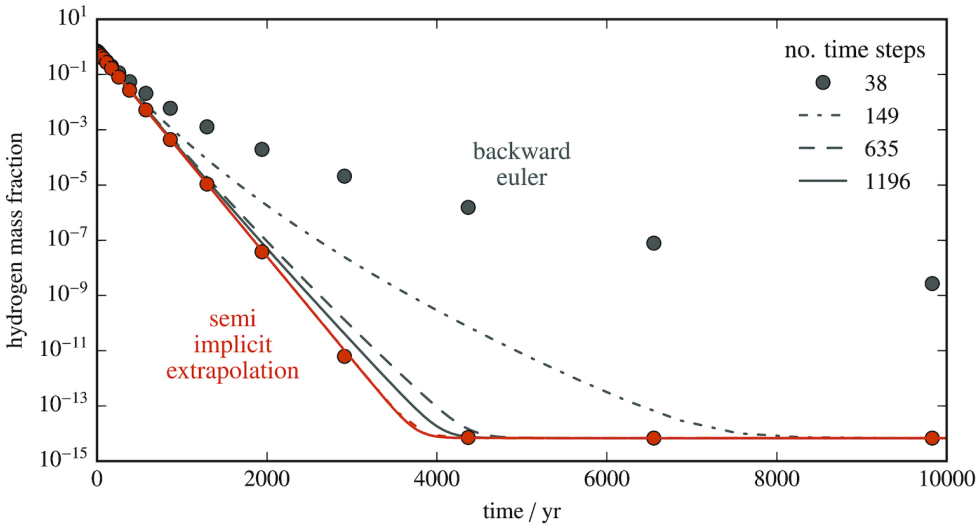

Figure 2.3 *A plot to show the speed of answer convergence between solver methods. Used is a quick hydrogen-burning calculation with temperature = 5.5 × 10^7 K and density, $\rho = 10^{\,2}$ g/cm^{-3} with a range of time steps. In all cases, the network is considered to have converged. All time steps cases for the semi implicit extrapolation method present similar results so all lines overlap. The backward-Euler method (grey dots and lines) requires substantially more time-steps to achieve the same level of accuracy as the Bader-Deuhard (semi implicit extrapolation) method (red dots and lines). Taken from Jones et al. [101].*

its free parameter is calibrated by reproducing the present radius, luminosity and age of the Sun. This is uncertain due to the parameterisation of a 3D process in a 1D simulation, and affects the TP, TDU and consequently the surface enrichment for stellar models of different masses and metallicities (Herwig [89], Rees et al. [178]).

The NugridPy tool provides the calculation of ejected masses for each isotope i, throughout its life. In this thesis, MESA stellar models are set to use the method outlined by Bloecker [16] for estimating the mass loss for AGB stellar models. Bloecker [16] considers observations to parameterise mass loss as a function of the total mass of the star, the star's current luminosity, and its stellar radius. Calculating the yield for an AGB star is rather simple as they only eject mass through stellar wind as opposed to massive stars which eject mass during a wind phase and supernova ejection stage (Hirschi, R. et al. [94], Karakas [104]). The net stellar yield for various isotopes in solar masses, mp_{im} of an AGB star with initial mass, m, for an element i is given by:

$$mp_{im}^{wind} = \int_0^{\tau(m)} \dot{M}(m,t)[X_i^S(m,t) - X_i^0]dt \tag{2.6}$$

where $\tau(m)$ is the final age of the star $\dot{M}(m,t)$ denotes the mass loss rate when the age of the star is equal to t provided by MESA as either the total mass of the star (in solar masses) and the mass loss rate (as solar masses lost per year) at each time step, and $X_i^S(m,t)$ is the surface abundance given in mass fraction of isotope i and X_i^0 is the isotopes initial mass fraction. The initial mass fraction term can be removed and this will calculate the total (gross) stellar yield, I will present total yields in Chapter 3.

Chapter 3

S-process nucleosynthesis from updated Asymptotic Giant Branch models

3.1 Asymptotic Giant Branch models and s-process efficiency

The Nucleosynthesis Grid (NuGrid) collaboration, develops and maintains tools for large scale post-processing of nucleosynthesis simulations. To ensure internal consistency for stellar models for a range of stellar masses and metallicities, NuGrid employs the use of a separate stellar evolution and post-processing code which share the same physics assumptions. The work of Ritter et al. [183] provided the first full data set of models with this consistency. These models will henceforth be referred to as RI18 models. Subsequently, Battino et al. [11] applied internal gravity wave (IGW) mixing (described in Denissenkov & Tout [59]) to convective boundaries to NuGrid's low-mass asymptotic giant branch (AGB) models with the aim of increasing the efficiency of the slow neutron-capture process (s-process), and this chapter will focus on their s-process nucleosynthesis. Part of the work presented here is published in Battino et al. [13]. I was responsible for post-processing the stellar models, interpreting the results and comparing to suitable stellar observables. I was researching and conducting sensitivity studies based on reaction rate uncertainties aiming at improving the

agreement between models and observables. This chapter also contains work published in Adsley et al. [3] where I performed post-processing calculations with newly evaluated ^{22}Ne(α,n)^{25}Mg and ^{22}Ne(α,γ)^{26}Mg reaction rates. The new models will henceforth be called "*set1-update*" and their properties are summarised in Table 3.1.

From this point onward all stellar models will be referred to by a code name which starts with an 'm' followed by a number indicating the initial mass in solar masses. After this, initial metallicity is expressed by what follows 'z'. As example, for *m3z2m2* the 'm3' refers to $3M_{\odot}$ meaning it is a three solar mass model, then the 'z2m2' is a shortened version of Z = 2×10^{-2}, where 'z2' is Z = 2, and 'm2' refers to the exponent in this case 'minus 2'. Other suffixes used in the new stellar model names refer to adjusted mixing parameters or additional mixing (described in Chapter 2.2.1): models with suffix hCBM have their mixing coefficient, D_2 being increased by a factor of 4.3 (this corresponds to the maximum uncertainty given by Denissenkov & Tout [59], see chapter 2.2.1). These models experience more efficient convective boundary mixing (CBM) and are able to form larger ^{13}C-pockets. Models with suffix rotmix have an added constant mixing coefficient, D_{rot} throughout the whole star. For rotmix.stx1.5 models this constant mixing coefficient is 1.5x stronger than the rotmix.st coefficient.

The introduction of IGW mixing in the *set1-update* models has a profound impact on the size of the ^{13}C pocket, compared to RI18 models, where a single exponential decay was adopted for the diffusive mixing scheme. Figure 3.1 compares a ^{13}C-pocket from the new *m2z1m2* model and another ^{13}C-pocket from the model with the same initial mass and metallicity in RI18, around the same mass coordinate at the beginning of the carbon-rich phase. The Figure clearly demonstrates the new model produces a larger pocket (by around a factor of three). This occurs due to a gentler gradient of the hydrogen profile formed by the CBM model (see Battino et al. [11] for more details) compared to RI18, when maximum penetration is reached by the convective envelope into the helium inter-shell during the third dredge-ups (TDUs). The Denissenkov & Tout [59] mixing method increases the hydrogen mass fraction further from the convective boundary than in the RI18 models. This allows the mass fraction of ^{13}C, X(^{13}C) to exceed 0.001 in a larger portion of the inter-shell, hence a larger ^{13}C-pocket is formed. In addition to a larger ^{13}C-pocket, another feature is the very similar abundance peak value of ^{13}C inside the pocket. This is due to the same CBM profile adopted at the inter-shell bottom during thermal pulses (TPs), leading to similar ^{12}C abundances

Name	M_{ZAMS} [$M_\odot$]	Z_{ZAMS}	Total TPs	O-rich TPs	D_2 [cm^2s^{-1}]	$Log_{10}(D_{rot})$
m2z1m2	2	0.01	25	18	10^{11}	–
m2z2m2	2	0.02	30	27	10^{11}	–
m2z3m2	2	0.03	30	29	10^{11}	–
m3z1m2	3	0.01	16	8	10^{11}	–
m3z2m2	3	0.02	24	15	10^{11}	–
m3z2m2-hCBM	3	0.02	24	15	4.3×10^{11}	–
m3z2m2-rotmix.stx2	3	0.02	24	17	10^{11}	–0.4
m3z2m2-rotmix.st	3	0.02	25	16	10^{11}	–0.7
m3z2m2-rotmix.std2	3	0.02	25	16	10^{11}	–1
m3z3m2	3	0.03	31	20	10^{11}	–
m3z3m2-hCBM	3	0.03	30	19	4.3×10^{11}	–
m3z3m2-rotmix.st	3	0.03	30	21	10^{11}	–0.7
m3z3m2-hCBM-rotmix.stx1p5	3	0.03	30	19	4.3×10^{11}	–0.5
m3z3m2-hCBM-rotmix.st	3	0.03	31	20	4.3×10^{11}	–0.7

Table 3.1 *List of AGB models and their properties, i.e. initial mass, initial metallicity, total number of TPs, number of O-rich TPs, CBM mixing coefficient D_2, and logarithmic value of constant mixing coefficient D_{rot}.*

in the inter-shell during the inter-pulse period and consequently, a similar ^{13}C peak value. A high peak abundance allows for the production of the heaviest *s*-process elements. ^{13}C-pockets larger than the ones produced here are found in stellar models from other groups (Cristallo et al. [44], Karakas [104], Lugaro et al. [138], Palmerini et al. [158], Vescovi et al. [209]).

Post processing calculations of *s*-process nucleosynthesis using the MPPNP code have been performed for *set1-update* models. In the following, the overproduction factors for *s*-process elements ($s/s_{\odot}$) are compared for different models (here, $s_{\odot}$ is the solar abundance and a $s/s_{\odot}$ value larger than 1 indicates a net production). Figure 3.2 shows a comparison of a $2M_{\odot}$ Z=0.02 and $3M_{\odot}$ Z=0.02 *set1-update* model (*m2z2m2* and *m3z2m2*) to same mass and metallicity models from RI18, and results from the FRUITY database (Cristallo et al. [44]). It is evident in both plots that RI18 has a much smaller *s*-process production than *m2z2m2*, *m3z2m2* and FRUITY. The *m2z2m2* model shows smaller production factors compared to FRUITY for all heavy elements. The *m3z2m2* model shows similar production factors to FRUITY in the barium mass region, however smaller production factors at the first *s*-process peak around Sr. This is due to FRUITY models not including any CBM at the base of the pulse driven convective zone (PDCZ). This leads to lower ^{12}C abundances in the inter-shell in FRUITY models, hence lower ^{13}C abundances and a lower neutron per iron seed ratio in the ^{13}C-pocket, which favours Sr-peak over Ba-peak elements (Cristallo et al. [47], Lugaro et al. [137]). For this same reason, FRUITY models have less carbon-rich TDUs compared to their comparative NuGrid models. With no CBM at the bottom of the inter-shell during the TDUs, no carbon is dredged up from the core. This makes TPs occur at a lower temperature because helium is more abundant in the inter-shell (see Battino et al. [13]), which leads to weaker triple alpha process activation producing less carbon. Therefore, when a TDU occurs, the mass that is dredged up to the envelope has a lower carbon content hence the star becomes carbon-rich later, i.e. closer to the end of its evolution. The production factors of all models are shown in Figure 3.3. As expected, lower metallicity models show a stronger production of the second (Ba region) and third (Pb region) *s*-process peaks, while the first peak (strontium region) is produced by higher metallicity models. In the following chapters, results from *set1-update* models will be compared to spectroscopic observations and pre-solar grain abundances.

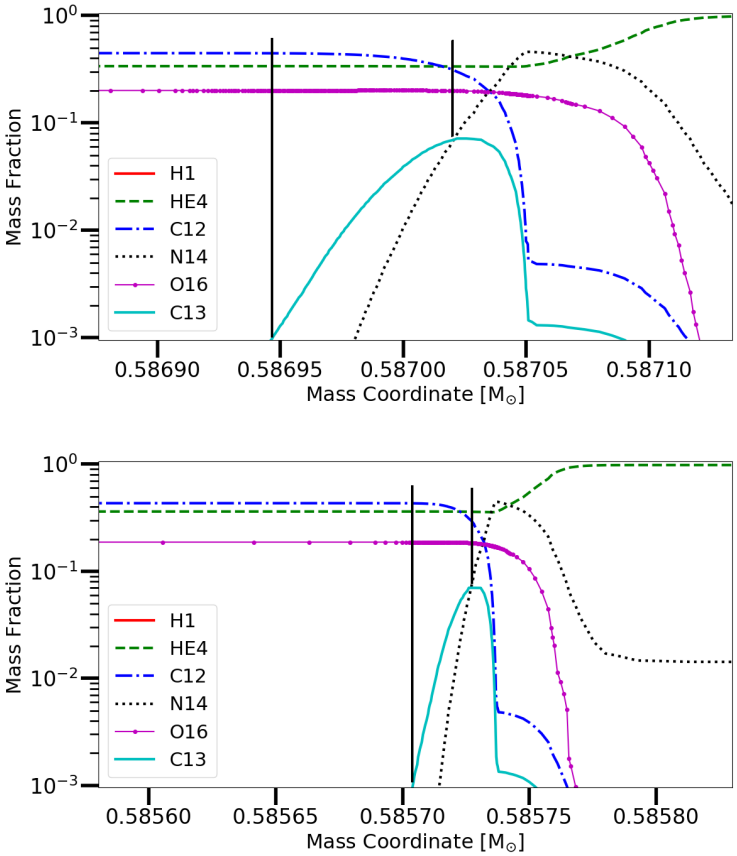

Figure 3.1 *Upper panel: the ^{13}C-pocket at the beginning of the carbon-rich phase from the m2z1m2 model. Lower panel: the ^{13}C-pocket at the beginning of the carbon-rich phase for a $M = 2M_{\odot}$, $Z = 0.02$ model from RI18 at a similar mass coordinate as the upper panel. The comparison shows m2z1m2 having a larger ^{13}C-pocket compared to RI18. The ^{13}C-pocket size shown between the two bold black lines is defined as the integrated mass difference between the points where the mass fraction of ^{13}C, $X(^{13}C)$, exceeds 0.001 and $X(^{13}C) \geq (^{14}N)$.*

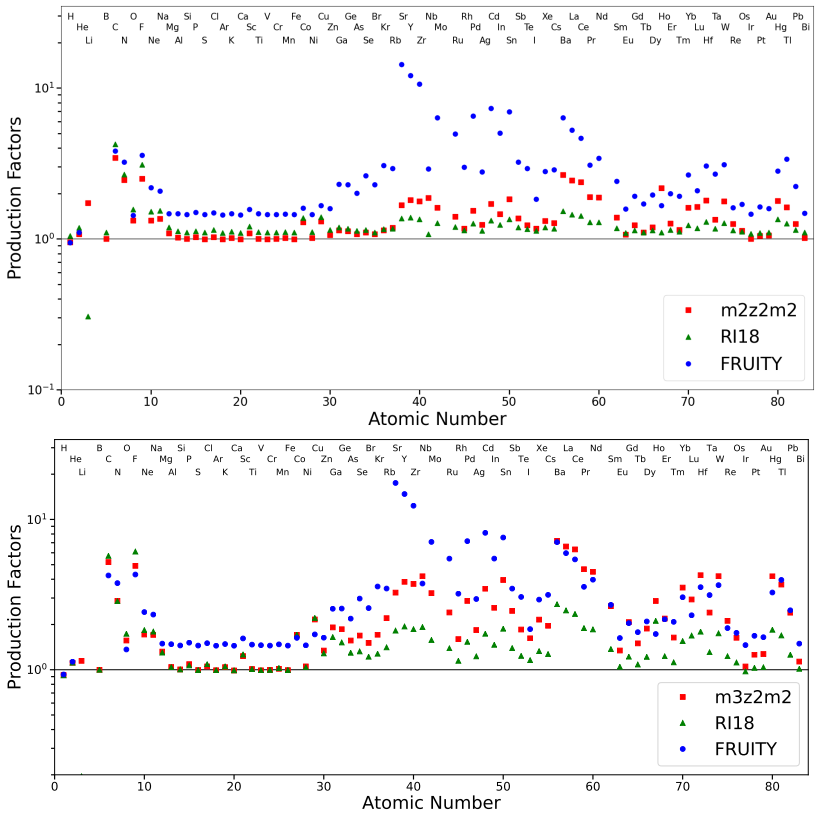

Figure 3.2 *Comparison of the elemental production factors for all elements. Upper panel: the comparison is between the m2z2m2, RI18 (Ritter et al. [183]) and FRUITY (Cristallo et al. [44]) for their respective $M = 2M_{\odot}$, $Z = 0.02$ models. Lower panel: is the same but for m3z2m2, RI18 (Ritter et al. [183]) and FRUITY (Cristallo et al. [44]) for their respective $M = 3M_{\odot}$, $Z = 0.02$ models.*

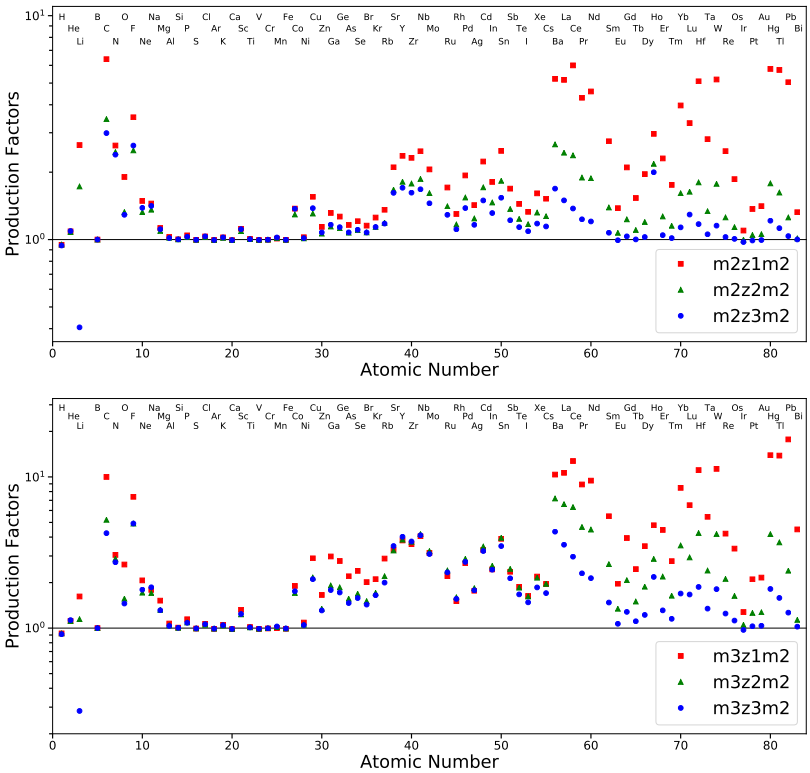

Figure 3.3 *Upper panel: Elemental production factors for $2M_{\odot}$ models with metallicities, $Z = 0.01$, 0.02, and 0.03. Lower panel: The same metallicities, but for $3M_{\odot}$ models.*

3.2 A comparison with spectroscopic observations

In the following, predictions from the *set1-update* models of surface abundances will be compared to spectroscopic observations. Elemental abundance ratios will be displayed using the square bracket notation:

$$[X/Y] = \log_{10}((X_*/Y_*)/(X_\odot/Y_\odot)) \tag{3.1}$$

where the subscript * denotes the stellar abundance, and subscript $\odot$ denotes the solar abundance, typically in mass fraction but any other abundance measurement can be used for ratios because the units cancel out. The unit of this notation is 'dex' or simply an order of magnitude. For Figures 3.4-3.6, observed abundance ratios from individual stars are shown as red solid circles and orange solid squares (with their error bars). For model predictions, a line indicates how surface abundances evolve over the whole evolution of the model, while symbols correspond to surface abundances at the beginning of each inter-pulse period (when the TDU has finished) for the carbon-rich AGB phase, this is the same for the FRUITY model.

3.2.1 Carbon stars

Carbon stars correspond to a late evolutionary stage of thermally pulsing AGB stars with surface abundances enriched in *s*-process products (Abia et al. [1], Busso et al. [21], Zamora et al. [220]). The name derives from the fact that the surface in the AGB phase turns from oxygen-rich to carbon-rich, due to convection in the star extending into the helium inter-shell, as a consequence causes ^{13}C to form, and leads to the *s*-process taking place around the core. This material then enriched the surface during TDUs. The products of the *s*-process have been directly observed using spectroscopy measurements for a large sample of carbon stars (also called R-type/N-type stars).

AGB stars produce the majority of *s*-process material during ^{13}C-pocket burning, while a smaller fraction of abundances are produced at higher neutron densities ($\geq 10^{11}$cm^{-3} neutrons) during the TP (Cristallo et al. [44], Raut et al. [177], Straniero et al. [191]). This environment is important for opening branching points and producing isotopes that are normally untouched by the *s*-process.

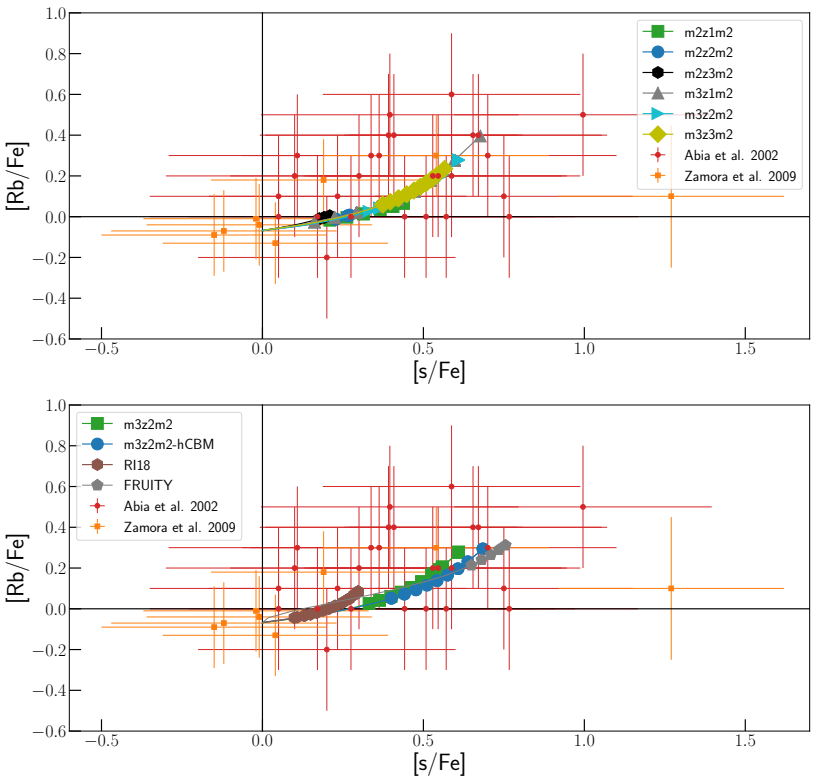

Figure 3.4 *Comparison of [Rb/Fe] versus [s/Fe], the upper panel shows set1-update models with initial masses of 2 and 3 $M_{\odot}$ and metallicities, $Z = 0.01$, 0.02 and 0.03 to carbon star spectroscopic data from Abia et al. [1] and Zamora et al. [220], and the lower panel: compares m3z2m2 with models from RI18 and FRUITY with the same mass and metallicity. The line corresponds to the surface abundance after a TDU, where the symbols signify carbon-rich TDUs.*

Rubidium production is mostly determined by the abundance of ^{85}Rb, but at high neutron densities, the branching at ^{86}Rb ($T_{1/2}$=18.6 days) is enabling the production of ^{87}Rb. ^{87}Rb is neutron magic (N=50) hence it has a low neutron capture cross section. This means it is less likely for the *s*-process to progress from this isotope. Figure 3.4 shows [Rb/Fe] over [s/Fe] abundances for a set of carbon stars observed by Abia et al. [1] and Zamora et al. [220]. Here "s" denotes the averaged abundance between first and second *s*-process peak elements. Assuming that the initial [Rb/Fe] abundance in these stars was solar (i.e. the solar composition is typical for the solar neighbourhood), the higher than solar [Rb/Fe] ratios found in carbon stars indicate that Rb is produced in these stars[1]. The observations are compared to several of the *set1-update* models (upper panel of Figure 3.4), as well as RI18 and FRUITY (lower panel). The evolution tracks of the *set1-update* models can extend throughout the center of the cloud of data points reproducing their values within the 1σ uncertainty provided, resulting in a better agreement with observations over the RI18 model with the same mass and metallicity. The *m3z2m2-hCBM* model with increased CBM produces higher [Rb/Fe] and [s/Fe] values, nearly matching predictions by FRUITY. The FRUITY model produces more rubidium as it has larger ^{13}C-pockets compared to *m3z2m2*, so more *s*-process material is produced. The ^{13}C-pockets have a lower peak ^{13}C value which favours Sr-peak elements, this occurs because CBM is not active at the bottom of the helium inter-shell in FRUITY models.

3.2.2 Barium stars

Barium stars are the secondary star of a binary system that has captured the stellar wind of the primary companion, an AGB star. The barium star has not enriched its surface as it is less evolved than the primary star. A barium star's surface spectrum can be used to study the *s*-process nucleosynthesis of its companion (Cseh et al. [49, 50], den Hartogh et al. [58], Pereira et al. [164], Roriz et al. [186]). Spectroscopic measurements of these distant stars using modern space and high altitude observatories can provide excellent high resolution spectra, allowing for accurate analysis of more absorption lines compared to the older measurements of carbon stars, contributing to a lower uncertainty (Cseh et al. [49, 50], den Hartogh et al. [58], Pereira et al. [164], Roriz et al. [186]). Due to the high quality of these data, it is possible to directly compare individual

[1]also unstable technetium is observed in these stars, which is evidence of ongoing nucleosynthesis

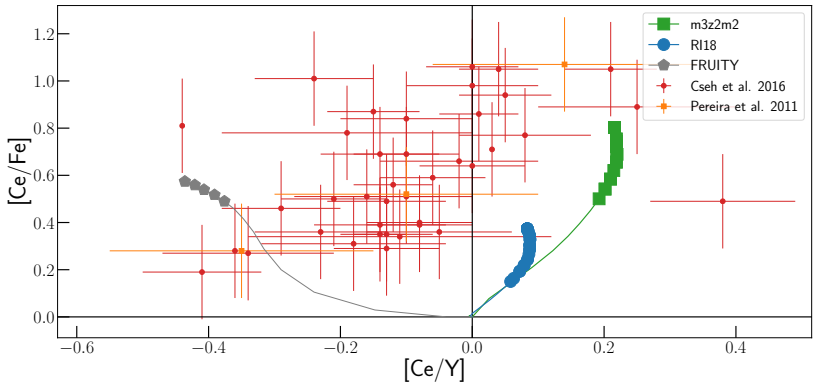

Figure 3.5 *Comparison of [Ce/Fe] versus [Ce/Y] for m3z2m2 with the same mass and metallicity models from RI18 and the FRUITY data base. The observational data of barium stars is taken from Cseh et al. [49] and Pereira et al. [164]. Considering the observational data, only stars that are comparable with the stellar models are included (i.e.* $-0.05 \leq$ *[Fe/H]* ≤ 0.15*).*

elemental ratios rather than the traditionally adopted hs and ls ratios (here hs refers to the abundance of some/all barium peak elements (Ba, La, Ce, Pr, Nd) and ls refers to the abundance of some/all strontium peak elements (Sr, Y, Zr)).

The ratio [Ce/Fe] describes the relation of second *s*-process peak element production with reference to the iron seeds of the *s*-process. [Ce/Y] presents the ratio of second peak to first peak elements. The correlation between these ratios allow an analysis of *s*-process production efficiencies. Figure 3.5 shows [Ce/Fe] versus [Ce/Y] ratios for the largest homogeneous set of barium star observations (Cseh et al. [49], Pereira et al. [164]). This is compared to the evolution of *m3z2m2* and the equivalent in mass and metallicity RI18 and FRUITY models. *m3z2m2* was chosen so a direct comparison with RI18 and other data sets was possible, and because *m3z2m2* produced the highest [Ce/Fe] of *set1-update*. The plot demonstrates that *set1-update* models produce more second peak elements compared to RI18, while the FRUITY model shows the opposite trend to *set1-update* and RI18 owing to a low hs production. All models have difficulty reproducing the observed abundance ratios. As mentioned in chapter 3.2.1, FRUITY models do not include CBM under the PDCZ, therefore the ^{12}C abundance in the inter-shell, and as a consequence the ^{13}C abundance in the ^{13}C-pocket is lower. This makes the FRUITY model diverge from RI18 and *set1-update* models, as FRUITY produces more first peak than second peak *s*-process material after each TDU.

From observations, rotating stars are common in the galaxy (den Hartogh et al.

[57], Herwig et al. [93], Langer et al. [119], Piersanti et al. [166], Siess et al. [188]). Rotation in stars reduces the neutron exposure produced by the ^{13}C-pocket because more of the neutron poison ^{14}N is mixed into the ^{13}C-pocket from the ^{14}N-pocket. A lower neutron exposure means heavier elements are either; not produced, or are produced in a lower abundance. So, stellar models that do not simulate rotation should reproduce the highest observable [Ce/Y], while including the effects of rotation should account for all of the lower values (Herwig [89], Piersanti et al. [166]). Figure 3.6 shows [Ce/Y] versus [Fe/H] (i.e. metallicity, Z) for all *set1-update* models with the addition of models with constant mixing, compared to FRUITY and Monash group models (Karakas & Lugaro [106]). Models without rotational mixing clearly reproduce the high values of [Ce/Y] and the models replicating a rotation effect can reproduce the lower values. Similar to FRUITY models, the Monash models do not include any CBM at the base of the PDCZ, hence they produce a lower final [Ce/Y] compared to the NuGrid models.

3.3 Comparison with mainstream silicon carbide (SiC) pre-solar grains

Presolar grains are 1 to 3 micrometer sized inclusions in meteorites. They condensed in the atmospheres/out flowing gasses of stars before the formation of the solar system and carry the unique isotopic signature of nucleosynthesis processes of the parent star. SiC grains of pre-solar origin condensed in the atmospheres of old AGB stars, and were ejected by AGB winds that polluted the interstellar medium, which also consists of molecular clouds in which new stars and planets are formed. When a planetary system forms, meteorites and asteroids form too, they carry grains with the signature of the pristine composition of the nebula to celestial bodies in the new solar system. Later when the meteorites are found on the Earth's surface, the grains can be extracted from them (Liu et al. [128], Lugaro et al. [136], Zinner [222]). The majority ($\sim$90%) of grains found are "mainstream" (Lugaro et al. [135], Palmerini et al. [158], Zinner [221]) grains, the majority carry the signature of the *s*-process in AGB stars of around solar metallicity in the mass range of two to three solar masses (Lewis et al. [123], Lugaro et al. [138]). The analysis of pre-solar grains has allowed the study of the origin and production of many different elements, such as Zr, Mo (Barzyk et al. [8]), Ba, Sr (Liu et al. [128], Liu et al. [129]), C, Si (Barzyk et al. [8], Liu

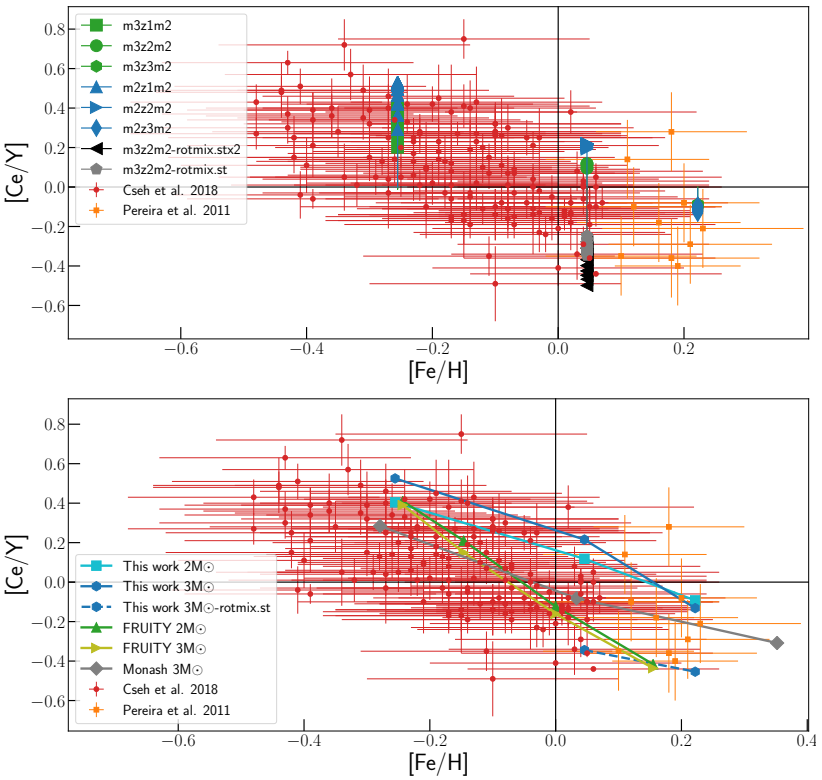

Figure 3.6 *Comparison of [Ce/Y] versus [Fe/H] results from the surface abundances after the last TDU of the standard models in Table 3.1 adding also m3z3m2-rotmix.st and m3z2m2-rotmix.st (lower panel only), which include an artificial mixing to replicate stellar rotation effects. The values inferred from spectroscopy analysis of barium stars by Cseh et al. [49] and Pereira et al. [164] are also shown as comparison. Also, in the lower panel results from the FRUITY data base and Monash Karakas & Lugaro [106] models are shown.*

et al. [128], Liu et al. [129], Zinner et al. [223]). Recently Lewis et al. [123] and Lugaro et al. [138] showed that AGB stars of solar to super-solar (a term denoting a metallicity significantly higher than solar metallicity) metallicity are the main producers of dust in the Galaxy and hence the grains that form from it. It should also be noted, Cristallo et al. [41] found using FRUITY models in galactic chemical evolution calculations, around solar metallicity models can produce a super-solar *s*-only abundance distribution (around 45% higher than observed).

Measurements from grains are given in δ-value notation to represent isotopic ratios, i.e. the permil variation with respect to the solar ratio (for which δ=0), so for these calculations δ(ratio)=((ratio/solar ratio)-1)×1000. In Figures 3.7-3.9 and 3.11-3.21, the line marking a theoretical prediction track corresponds to results per inter-pulse period, with large symbols corresponding to the carbon-rich phase, which is a necessary condition for AGB stars to form SiC grains and to produce strong stellar wind.

3.3.1 Barium

Barium is a key identifying element for the second *s*-process peak. Barium has five stable isotopes; ^{134}Ba, ^{135}Ba, ^{136}Ba, ^{137}Ba, and ^{138}Ba. The most abundant barium isotope in the solar system is ^{138}Ba, which is a neutron magic isotope (N=82). Its (n,γ) Maxwellian averaged cross-section (MACS) is a factor of over 10 smaller than the MACS for ^{136}Ba. ^{134}Ba and ^{136}Ba are considered as *s*-only nuclei, as they are shielded from the rapid neutron-capture process (*r*-process) by their stable xenon isobars. The relative abundances of ^{134}Ba and ^{136}Ba produced during AGB nucleosynthesis are affected by the branching point at ^{134}Cs (Barzyk et al. [8], Li et al. [124], Lugaro & Chieffi [133], Taioli et al. [197]). The stellar β-decay rate of ^{134}Cs has a strong temperature dependence (Li et al. [124], Lugaro & Chieffi [133], Taioli et al. [197], Takahashi & Yokoi [198]), increasing almost two orders of magnitude as the temperature rises to $\sim 3 \times 10^8$K during TPs. Its shorter half-life at higher stellar temperatures, can be overcome with the relatively high peak neutron density during TPs due to the marginal activation of the ^{22}Ne neutron source (with a neutron density $\sim 10^{9-11}$ cm^{-3}, compared to 10^7 - 10^8 cm^{-3} for the ^{13}C neutron source (Cristallo et al. [44, 46], Herwig [89], Karakas & Lattanzio [105], Karakas & Lugaro [106], Straniero et al. [191])). The neutron capture rate of ^{134}Cs can increase above its β-decay rate, so that ^{135}Cs production is favored over ^{134}Ba production. ^{135}Cs is stable ($T_{1/2}$ = 2.3 million years) on the

timescale of the *s*-process in AGB stars (t $\sim$ 20 thousand years; Gallino et al. [75], Lugaro & Chieffi [133], Taioli et al. [197]) and continues to undergo neutron capture to form unstable ^{136}Cs ($T_{1/2}$ = 13 days), almost all of which decays to ^{136}Ba. Consequently, high neutron fluxes can partially bypass both ^{134}Ba and ^{135}Ba, to accumulate ^{136}Ba while little change can be seen for ^{137}Ba or ^{138}Ba (Barzyk et al. [8], Lugaro & Chieffi [133], Lugaro et al. [136], Taioli et al. [197]). This implies barium isotopic ratios are a good probe for how neutron densities evolve during the *s*-process in the ^{13}C-pocket and TPs.

The panels in Figure 3.7 display a number of barium isotopic ratios. Measured ratios for mainstream SiC grains (Liu et al. [128], Liu et al. [129]) are compared to *set1-update* model predictions. There is good agreement with measured values for ^{134}Ba/^{136}Ba and ^{137}Ba/^{136}Ba versus ^{135}Ba/^{136}Ba ratios while for ^{138}Ba/^{136}Ba only the highest values can be reproduced. In general the agreement is best for models with higher mass and higher metallicity, so these models with M=3 $M_{\odot}$ and Z = 0.02 and 0.03 will be used in subsequent plots.

Figure 3.8 shows ^{138}Ba/^{136}Ba versus ^{135}Ba/^{136}Ba again for the aforementioned models, but also includes models with additional mixing, i.e. higher CBM, and higher CBM in conjunction with rotational mixing. In these cases, the evolution track is pushed to lower ^{138}Ba/^{136}Ba values, leading to a better match with observations. The *m3z3m2-hCBM-rotmix.st* model can reproduce the higher ^{138}Ba/^{136}Ba and ^{135}Ba/^{136}Ba values simultaneously, while *m3z2m2-rotmix.st* (the lower metallicity model without higher CBM but with rotational mixing), can reproduce the mean ^{138}Ba/^{136}Ba value from Liu et al. [129]. Another explanation for a disagreement between model and observation may be the use of an erroneous nuclear reaction rate. ^{22}Ne(α,n)^{25}Mg is the main neutron source during the TP and its reaction rate is very uncertain. The default ^{22}Ne(α,n)^{25}Mg rate adopted in the models is by Jaeger et al. [100] however, a 2 sigma uncertainty is estimated to correspond to a factor of about 0.5 (Iliadis et al. [99], Jaeger et al. [100]). A recent new evaluation of the ^{22}Ne(α,n)^{25}Mg rate by Adsley et al. [3] recommend a reaction rate that is 0.4x Jaeger et al. [100] (see the first panel of Figure 3.8). Thus, isotopic ratios were calculated for the m3z3m2-hCBM using a 2 times smaller ^{22}Ne(α,n)^{25}Mg rate in MPPNP (model denoted with suffix 0.5x22Ne(alpha,n)). This results in a decrease of ^{138}Ba/^{136}Ba ratios in the models.

A reaction rate that affects particularly ^{137}Ba/^{136}Ba abundances is ^{137}Ba(n,γ). The standard MPPNP package uses the stellar cross section recommended in the Kadonis v0.3 (Dillmann et al. [63]) database for this reaction, however the

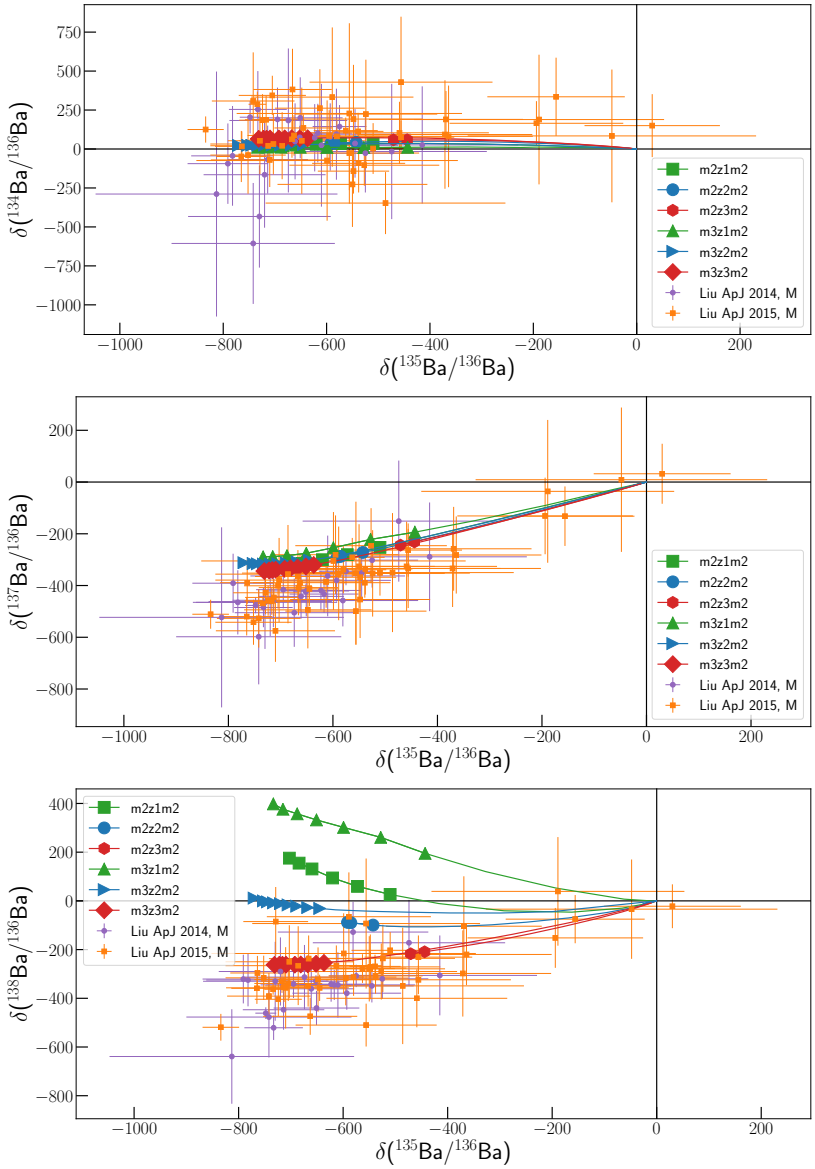

Figure 3.7 *Comparison of stellar models presented in this work with measured barium isotopic ratios from mainstream pre-solar silicon carbide grains (Liu et al. [128], Liu et al. [129]). Each line representing a theoretical prediction corresponds to an inter-pulse period, while symbols correspond to the carbon-rich phase.*

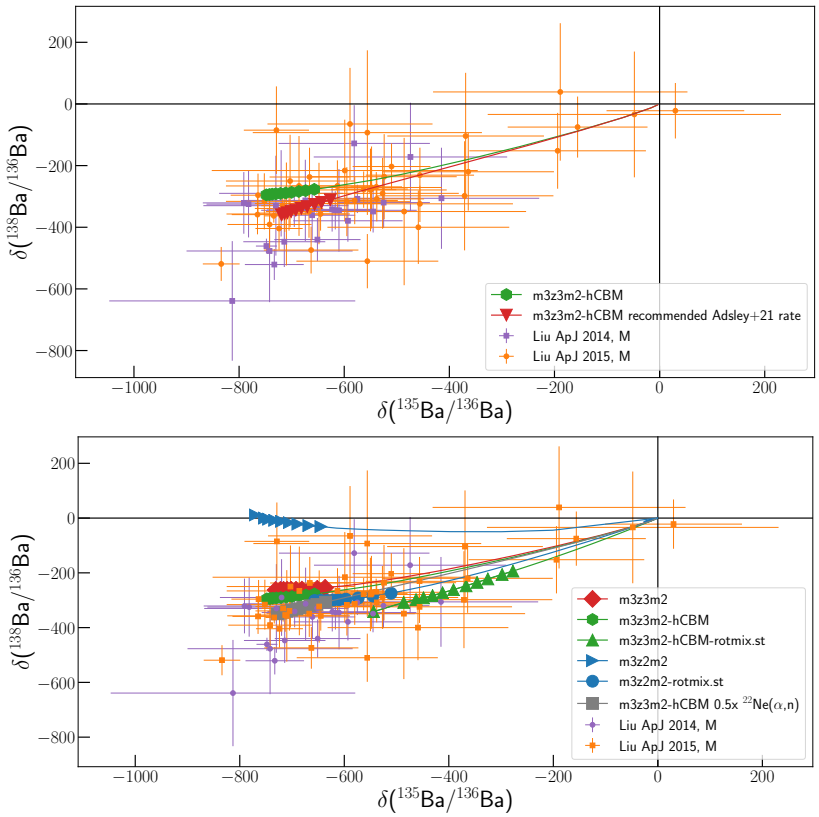

Figure 3.8 *Comparison of $\delta(^{138}Ba/^{136}Ba)$ versus $\delta(^{135}Ba/^{136}Ba)$; in the upper panel, For clarity the m3z3m2-hCBM default and with the Adsley et al. [3] recommended rate including the Ota et al. [155] measurement. And in the lower panel, m3z2m2, m3z3m3, and m3z3m3-hCBM. Also, included is the m3z3m3-hCBM model with a reaction rate test, set to the Adsley et al. [3] recommended high rate. And two model including artificial rotation induced mixing, m3z2m2-rotmix.st and m3z3m3-hCBM-rotmix.st.*

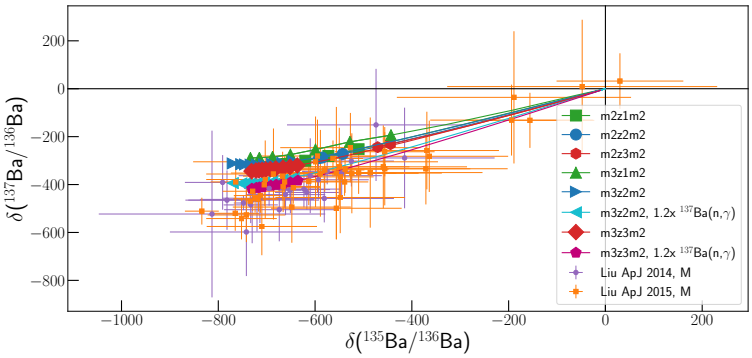

Figure 3.9 *Comparison of m3z2m2 and m3z3m2 for $\delta(^{137}Ba/^{136}Ba)$ versus $\delta(^{135}Ba/^{136}Ba)$ with measurements from SiC grains: shown are results obtained when adopting the $^{137}Ba(n,\gamma)^{138}Ba$ given by Kadonis v0.3 (*MPPNP*'s standard case) to what is recommended in Kadonis v1.0 (i.e. a factor of 1.2 higher than Kadonis v0.3).*

updated Kadonis v1.0 (Reifarth [179]) has revised this recommendation to a 20% larger cross section. The new recommendation was tested on both the m3z2m2 and m3z3m2 models. Scaling the ^{137}Ba(n,γ)^{138}Ba rate by a factor 1.2 leads to a better agreement of ^{137}Ba/^{136}Ba ratios (see Figure 3.9).

Summarising, *set1-update* models reproduce ^{134}Ba/^{136}Ba values very well. For ^{137}Ba/^{136}Ba a better agreement can be reached if the ^{137}Ba neutron capture cross section was a factor 1.2x higher. Additional mixing applied to the models does not impact on ^{134}Ba/^{136}Ba and ^{137}Ba/^{136}Ba ratios, but lead to lower ^{138}Ba/^{136}Ba values which is more in line with observations.

3.3.2 Strontium

Strontium is a constituent element of the first *s*-process peak, like barium it has a neutron magic isotope, ^{88}Sr (Käppeler et al. [116], Lugaro & Chieffi [133], Straniero et al. [191]). And two other isotopes only produced by the *s*-process, ^{86}Sr and ^{87}Sr. In the krypton–rubidium–strontium region, two branching points exist at ^{85}Kr and ^{86}Rb, seen in Figure 3.10. ^{85}Kr possesses an isomeric state with a short $\beta-$ decay half-life ($T_{1/2}$ = 4.5 hours) compared to the ground state ($T_{1/2}$ =11 years). The isomer and the ground state are not in thermal equilibrium at the helium-shell temperature in AGB stars. The proton-rich nuclide ^{84}Sr is off the *s*-process path and is therefore destroyed by neutron captures during the *s*-process in AGB stars. AGB stars are believed to be responsible for: 60% of solar system ^{86}Sr and ^{87}Sr, and 70% of neutron-magic ^{88}Sr (Bisterzo et al. [15], Travaglio et al.

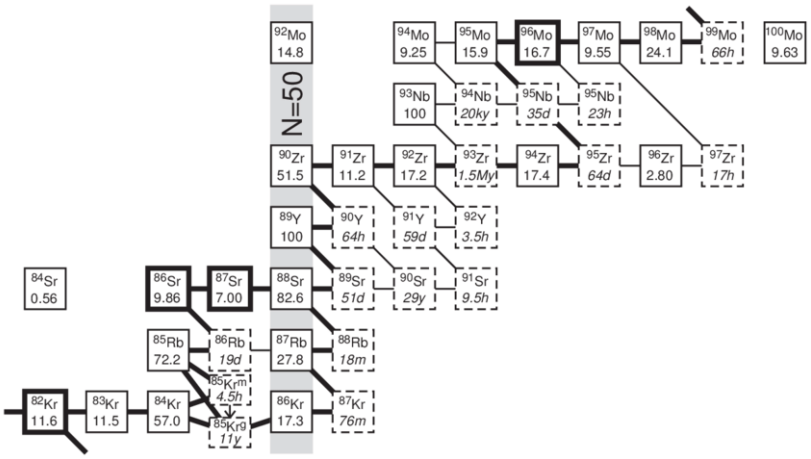

Figure 3.10 *The Kr to Mo section of the chart of the nuclides. The main path of the s-process is shown with thick interconnecting lines. Alternative paths are indicated with thin lines. Stable nuclides are solid boxes and unstable nuclides are dashed boxes. Abundances in percent are shown for the stable and half-lives for the unstable nuclides. Taken from Lugaro et al. [136].*

[204]).

The lowest ^{84}Sr/^{86}Sr values observed in mainstream grains are due to a ^{86}Sr overproduction during the ^{13}C-pocket burning (Liu et al. [129], Lugaro et al. [135]). The abundance distribution of ^{86}Sr and ^{87}Sr is affected by the preceding branching points ^{85}Kr and ^{86}Rb: ^{86}Sr and ^{87}Sr are produced in the ^{13}C-pocket, but then partially destroyed during the the TP as neutron captures on ^{85}Kr and ^{86}Rb bypass ^{86}Sr and ^{87}Sr. Thus, the ^{22}Ne(α,n) neutron source rate impacts on these abundances. Neutron magic ^{88}Sr has a much smaller (>factor 10) neutron capture cross section than the Sr isotopes discussed before, and thus behaves as a bottleneck of the *s*-process flow. The lowest panel of Figure 3.11 shows the ^{88}Sr/^{86}Sr value is also affected by stellar uncertainties, such as mixing.

In Figure 3.11 strontium isotopic ratios in meteoritic grains are compared with the standard *set1-update* models of this study. From the second and fourth panels, rotational mixing could help to cover a wider range of grains, particularly for ^{88}Sr/^{86}Sr, where the neutron-magic ^{88}Sr is depleted because of a higher concentration of ^{14}N inside the ^{13}C-pocket. Notably, the lowest panel in Figure 3.11 presents also *m3z3m2-rotmix.st* and *m3z3m2-rotmix.stx1p5* models, which are representative for a range of diffusion coefficients. Rotation may also improve the comparison to measured ^{84}Sr/^{86}Sr ratios, moving the evolution track of the models closer to the cloud of values beyond -800 in delta values. Lower

destruction of ^{86}Sr is a consequence of the lower neutron-exposure, while ^{84}Sr is unaffected only being produced by the proton-capture process (p-process) (Arnould & Goriely [5], Battino et al. [12], Nishimura et al. [152], Travaglio et al. [205]). With the average experimental uncertainty of the grains for values of -1000<δ(^{84}Sr/^{86}Sr)<-800 being around 100, the predictions cover a large portion of the pre-solar grain measurements.

If models with the rotational mixing parmeterisation provide a better match to Sr isotopic abundances, these models would be expected to match the Ba abundances determined in the same grain. Figure 3.12 shows such a comparison, with ^{88}Sr/^{86}Sr plotted against ^{138}Ba/^{136}Ba. While the *set1-update* models do not reproduce Sr isotopic ratios and only the highest metallicity models reproduce some of the Ba isotopic ratios, the models including rotational mixing reproduce the large spread observed for Ba isotopic ratios, while also showing a better agreement with Sr isotopic ratios.

3.3.3 Zirconium

Zirconium belongs to the first s-process peak and its isotopic abundances are sensitive to AGB stellar conditions. The s-process path in the Zr-Mo region is shown in Figure 3.10. Zirconium isotopes lie close to a magic number of neutrons (N=50) where ^{90}Zr is neutron magic. This results in ^{90,91,92,94}Zr abundances being sensitive to the neutron exposure. ^{96}Zr is preceded by the s-process branching point ^{95}Zr ($T_{1/2}$=64 days), and therefore its abundance is highly sensitive to the peak neutron density. Additionally ^{90,91}Zr/^{94}Zr ratios may be affected by the branching points at the unstable ^{89,90}Sr and ^{91}Y (see Karakas & Lattanzio [105], Lugaro & Chieffi [133], Lugaro et al. [136], Straniero et al. [191]). Neutron capture cross sections on these branching points are uncertain as only theoretical estimations are available, which impact on the accuracy of ^{96}Zr, and ^{90,91}Zr/^{94}Zr predictions.

Figure 3.13 shows the predictions of zirconium isotopic ratios for the *set1-update* models compared to grains data by Barzyk et al. [8]. The isotopes of zirconium with atomic mass 90, 91, 92, and 94 are wholly produced in the ^{13}C-pocket, while ^{96}Zr is exclusively produced during the TP, where neutron densities are high enough to overcome unstable ^{95}Zr. As expected, higher metallicity models produce the lower ^{96}Zr/^{94}Zr values, since they produce more first peak elements compared to the second peak (lower neutron/seed ratio) increasing the ^{94}Zr

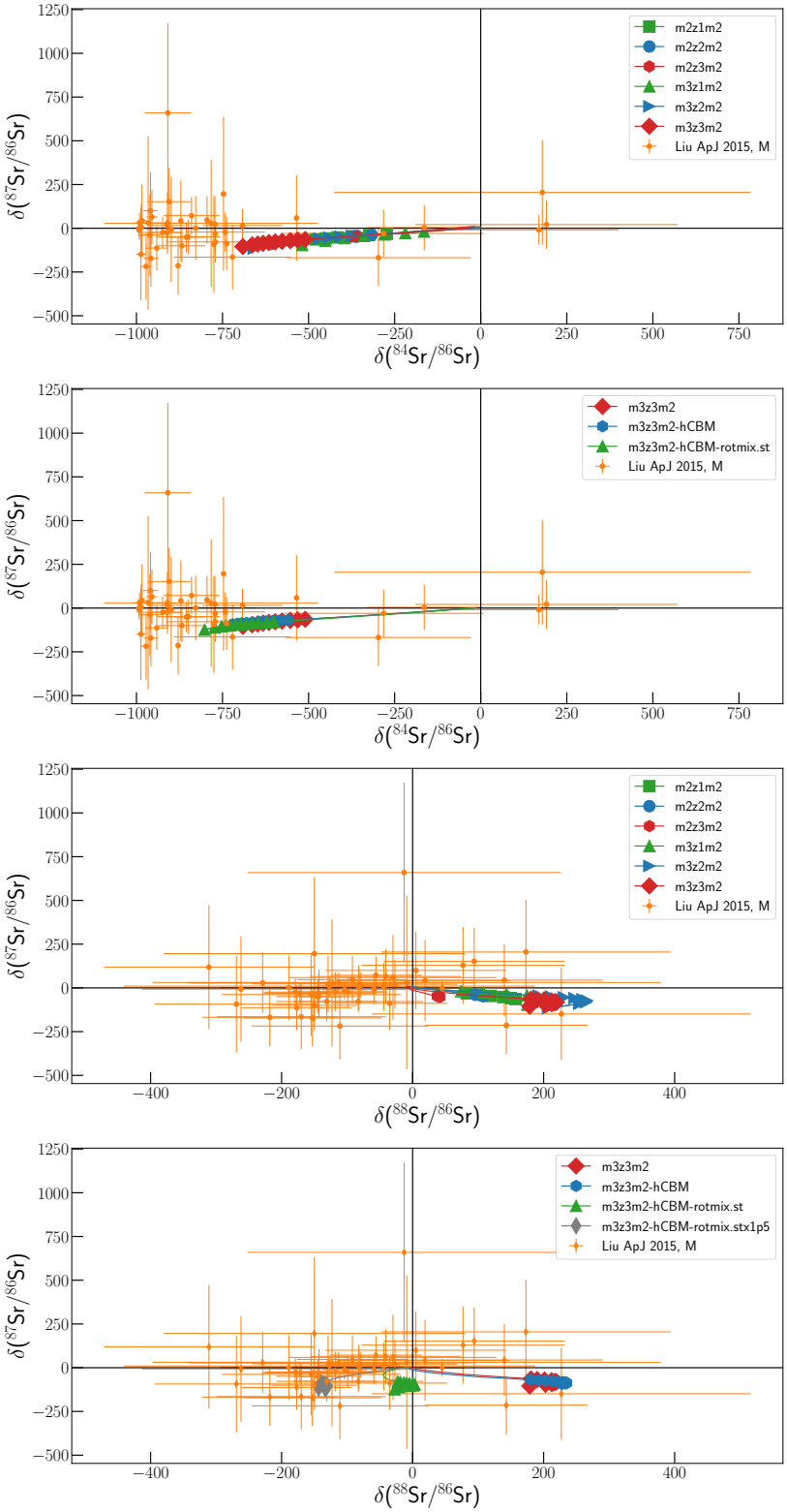

Figure 3.11 *Comparison of stellar models presented in this work with measured Sr isotopic ratios from mainstream pre-solar SiC grains (Liu et al. [129]). It is visible how rotation-induced mixing may help self-consistently cover the whole observed range, in particular in* $^{88}Sr/^{86}Sr$*. Error bars account for a* 2σ *uncertainty.*

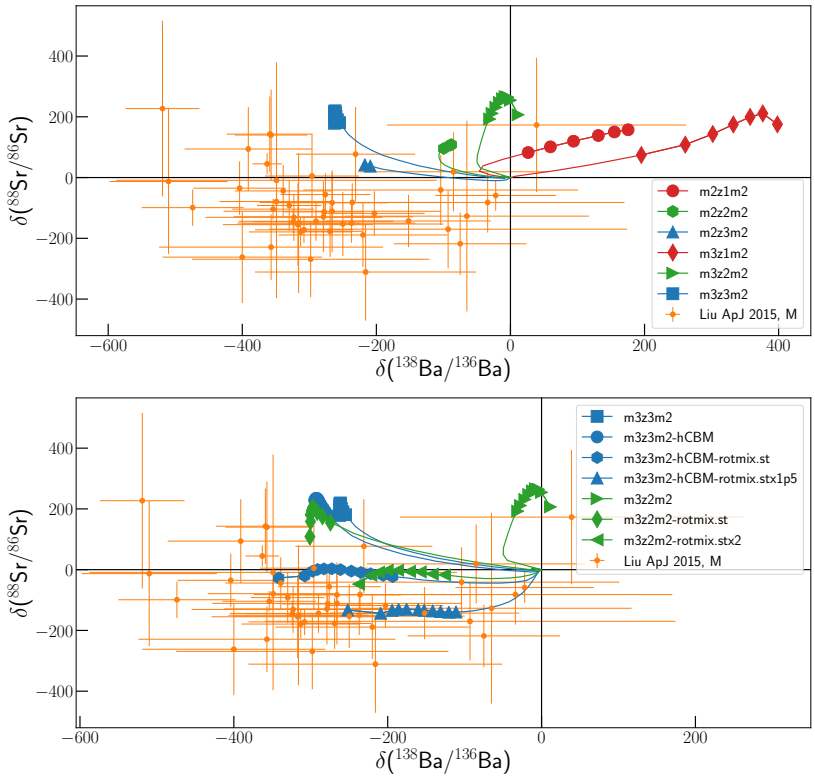

Figure 3.12 *Comparison of correlated measurements of Sr and Ba from Liu et al. [129], compared to the standard model set in the upper panel and to models including artificial rotation-induced mixing in the lower panel.*

abundance, and they exhibit lower temperatures during the TPs which limits the production of ^{96}Zr through a weaker activation of the ^{22}Ne(α,n)^{25}Mg neutron source resulting in a smaller peak neutron density. Both the standard and rotmix models perform poorly only touching a few grains. In general, $^{90;91;92}$Zr/^{94}Zr measured in grains are reproduced well in the models. However, both standard and rotmix models are not able to reproduce the lowest ^{96}Zr/^{94}Zr ratios observed, only matching the highest measured ratios.

The discrepancy with ^{96}Zr/^{94}Zr could be explained when considering uncertainties in the CBM mixing parameterisation. Therefore, in Figure 3.14 grains data is compared to the models with increased CBM mixing. In addition, results from RI18 are added for reference. The hCBM model reproduces the lower values of ^{96}Zr/^{94}Zr achieving a good correlation with the data points at the edge of the grain cloud. The ^{13}C-pocket sizes in *m3z3m2-hCBM* are around 10^{-4}M$_{\odot}$in mass coordinate, this is a factor of 1.5 larger than the typical pocket size in the *m3z3m2* stellar model. This enables a higher production of ^{94}Zr therefore lowering the ^{96}Zr/^{94}Zr with every subsequent TDU. It should be noted that the CBM parametrisation in Battino et al. [13] is calibrated to a M = 3M$_{\odot}$, Z = 0.02 model, and assumed to be valid for other metallicity models (Denissenkov & Tout [59] assumed IGW mixing is metallicity independent but a recent study from Battino et al. [10] suggested otherwise). This may introduce additional uncertainty to the predictions of high metallicity models.

Another source for the discrepancies between model predictions and measured grains abundances may be uncertainties in the nuclear reaction rates used in the models. As ^{94}Zr is used in all the isotopic ratios considered, the ^{94}Zr(n,γ) cross section is considered first. For Figures 3.13, and 3.14, the ^{94}Zr MACS from a measurement by Tagliente et al. [196] was used. However, another recent measurement by Dillmann [61] obtains a smaller MACS. Therefore, the MPPNP runs were repeated using 0.8 times the ^{94}Zr(n,γ) MACS, which corresponds to the lower limit (value minus 1σ) from Dillmann [61]. For this scenario, the lowest values of ^{91}Zr/^{94}Zr and ^{92}Zr/^{94}Zr are now reproduced, as shown in Fig. 3.15. Also, when applying the rotmix models the highest values can be explained.

Concerning ^{96}Zr/^{94}Zr, the most uncertain neutron capture rate is from unstable ^{95}Zr, where no experimental data are available. A factor 2 uncertainty is assumed for the ^{95}Zr(n,γ)^{96}Zr MACS, which is consistent with other studies (Lugaro et al. [139]). Thus, the predictions for a 2 times smaller ^{95}Zr(n,γ)^{96}Zr rate were tested. As ^{96}Zr is produced exclusively in the TP where neutron densities exceed those

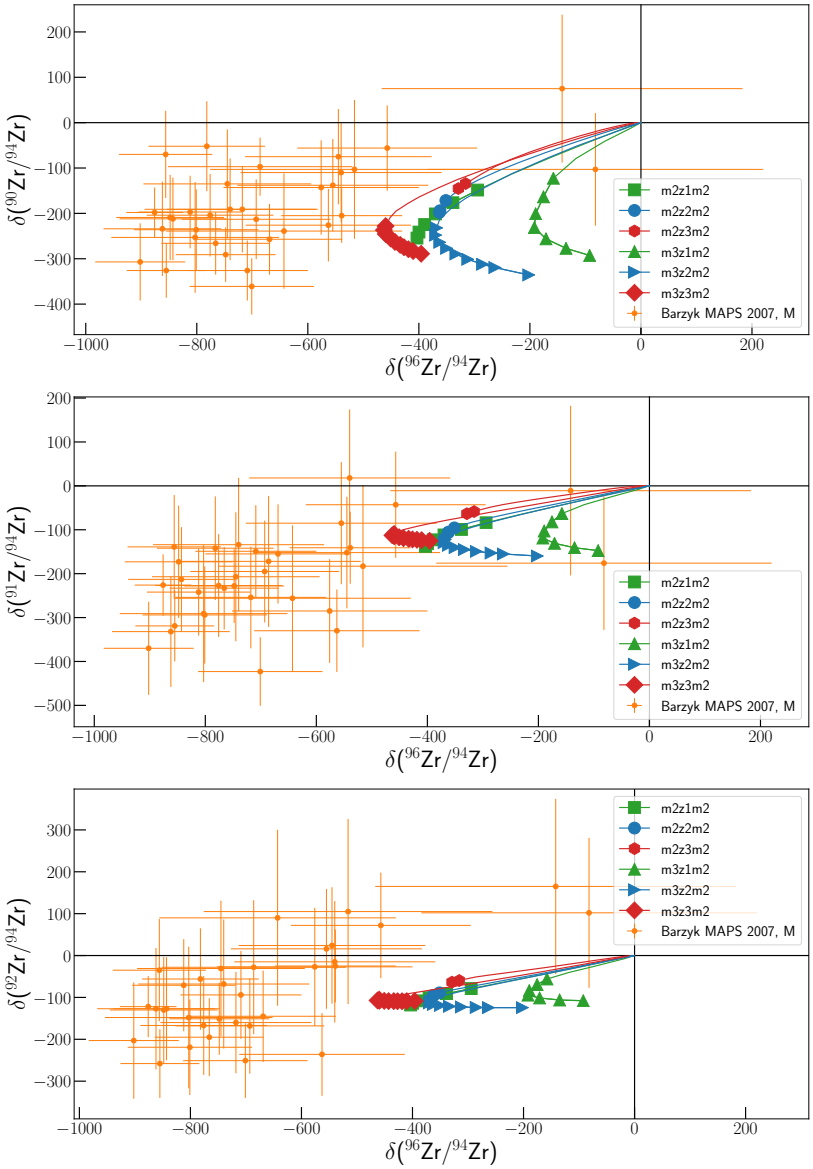

Figure 3.13 *Comparison of stellar models presented in this work with Barzyk et al. [8] measured zirconium isotopic ratios from mainstream presolar silicon carbide grains.*

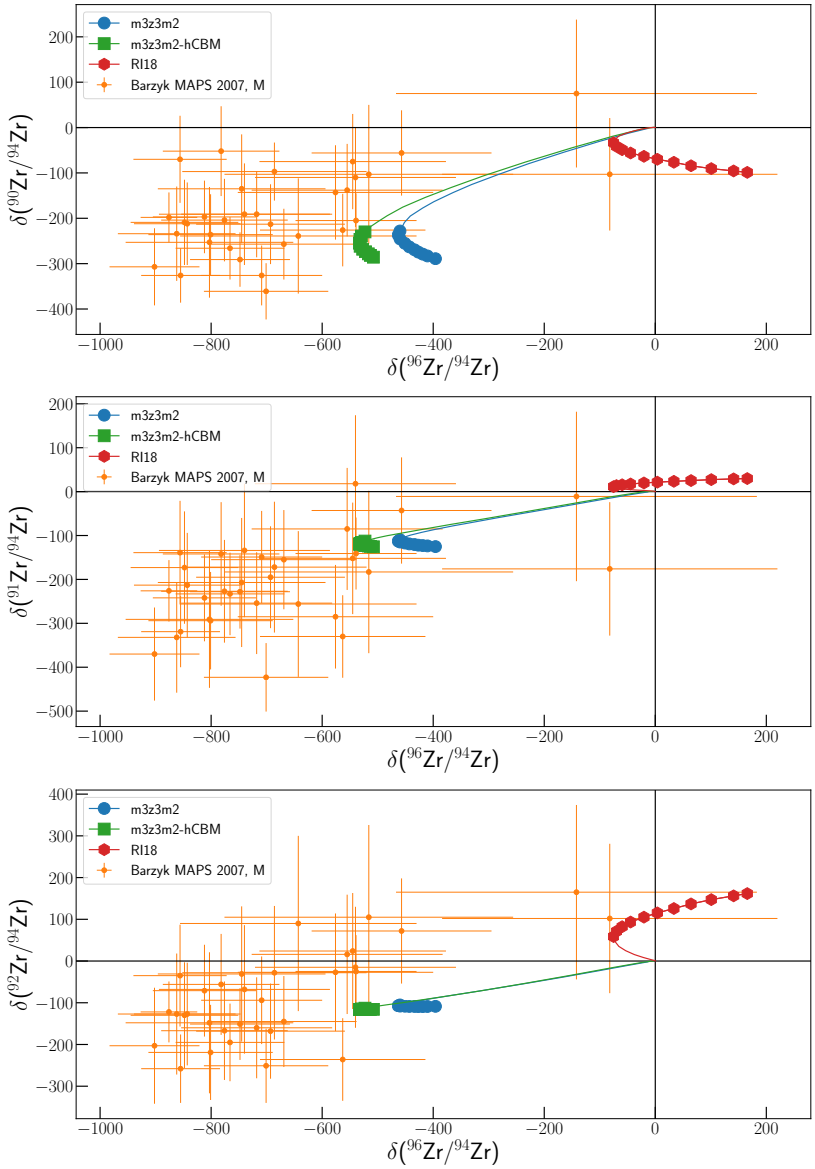

Figure 3.14 *Same as in Figure 3.13, but the results are shown for models m3z3m2, RI18, and m3z3m2-hCBM. The larger s-process production in m3z3m2-hCBM is a result of a* ^{13}C*-pocket that is a factor 1.5 larger in mass-coordinate compared to m3z3m2, this leads to a stronger production of* ^{94}Zr *and thus decreases the* $^{96}Zr/^{94}Zr$ *isotopic ratio.*

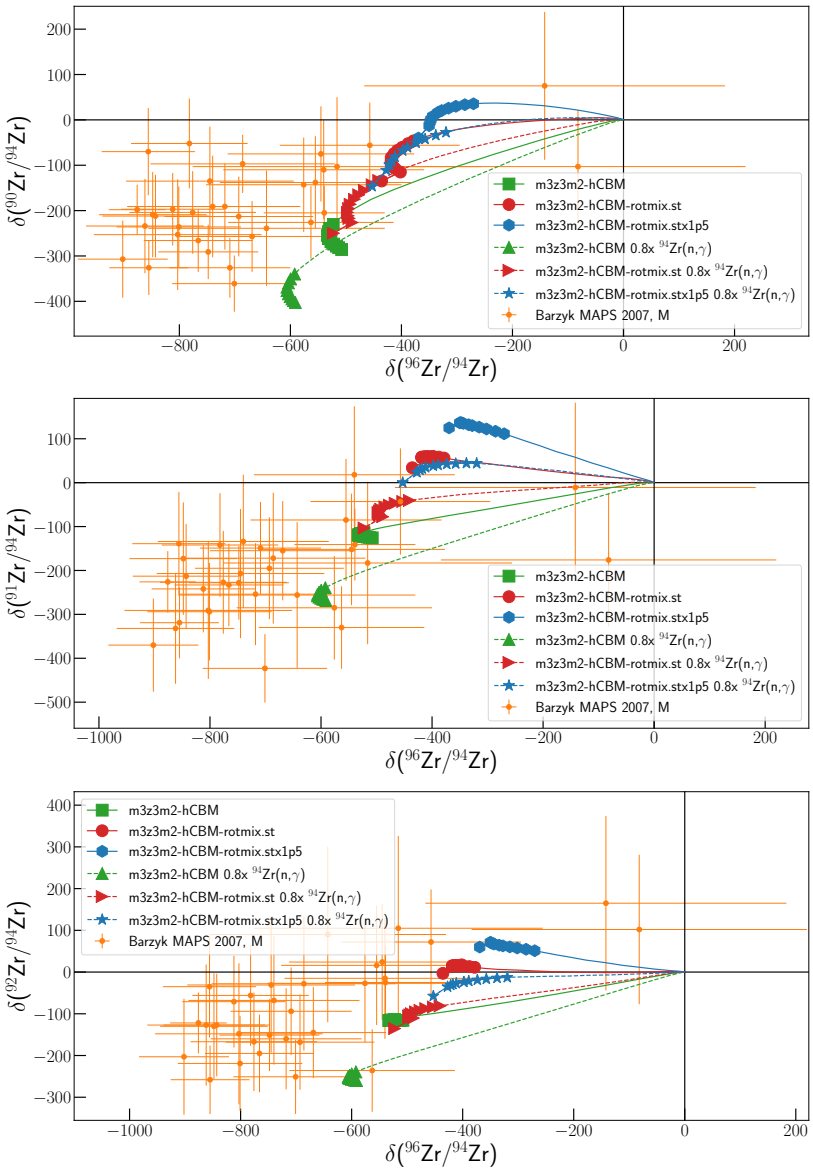

Figure 3.15 *Same as in Figure 3.13, but shown is the impact of the uncertainty from the neutron capture rate of ^{94}Zr on the theoretical predictions. To be specific, applying a factor of 0.8 to the $^{94}Zr(n,\gamma)^{95}Zr$ reaction rate to test the value recommended by the lower limit (value minus 1σ) from Dillmann [61], as it is 20 per cent lower than the Lugaro et al. [139] recommended reaction rate adopted. Also, shown is the effect of rotation-induced mixing, which combined with the neutron capture reaction rate uncertainties: can effectively reproduce the whole range of measured $^{90}Zr/^{94}Zr$ (these can be reproduced by the standard models as can be seen in Figure 3.13), $^{91}Zr/^{94}Zr$, and $^{92}Zr/^{94}Zr$ values.*

of the ^{13}C-pocket, also, considered are the uncertainties of the ^{22}Ne(α,n)^{25}Mg rate, and scale this reaction rate also by a factor 0.5 (what has been done for barium, see chapter 3.3.1). Figure 3.16 shows the result when the Adsley et al. [3] reaction rate can move the evolution track into the cluster of grain measurements. Figure 3.17 shows that results applying both the: ^{22}Ne(α,n)^{25}Mg and ^{95}Zr(n,γ) scaling factors can move the evolution track further into the cluster of grain measurements. The majority of grains data have -800< $\delta(^{96}Zr/^{94}Zr)$ <-600 within experimental uncertainty, which the *m3z3m2-hCBM* model with both reaction tests included can successfully reproduce as its track is carbon rich between -750 and -650 in delta values.

To summarise, *set1-update* models reproduce ^{90}Zr/^{94}Zr values very well. For $^{91;92}$Zr/^{94}Zr improvements can be made with the inclusion of a 0.8x lower factor on the ^{94}Zr neutron capture cross section. Rotational mixing can be used to reach the few grains with the highest values of $^{90;91;92}$Zr/^{94}Zr. Only the middle of ^{96}Zr/^{94}Zr values can only be achieved through the use of higher mixing and manipulation of the ^{95}Zr(n,γ) and ^{22}Ne(α,n) MACS. So, it is not possible to match the few grains that exhibit an extreme deficiency of ^{96}Zr. Accurate stellar rates of ^{95}Zr(n,γ) and ^{22}Ne(α,n) are therefore crucial to benchmark stellar models against measured zirconium abundances in grains. Alternatively, solutions to this problem are proposed from different models in which other mixing mechanisms are implemented e.g magnetic buoyancy induced mixing (see Palmerini et al. [156, 157], Palmerini et al. [158], Vescovi [208], Vescovi et al. [209]), exponential decay of convective velocities (see Cristallo et al. [42, 43, 45]) and partial mixing zone (see Karakas [104], Karakas & Lugaro [106], Lugaro et al. [138, 139]).

3.3.4 Molybdenum

Molybdenum consists of seven stable isotopes; ^{96}Mo is only produced by the *s*-process, ^{92}Mo and ^{94}Mo are only produced by the *p*-process (Battino et al. [12], Lugaro & Chieffi [133], Travaglio et al. [205]), and ^{100}Mo is produced by the *r*-process. This leads to ^{92}Mo, ^{94}Mo, and ^{100}Mo only being depleted in AGB stars. Many branching points can alter the distribution of molybdenum isotopic ratios; ^{93}Zr, ^{95}Zr, ^{94}Nb, and ^{95}Nb can block the production of specific molybdenum isotopes, namely ^{94,95,96}Mo (Barzyk et al. [8], Lugaro & Chieffi [133]). From Figure 3.10, ^{93}Nb the sole stable isotope of the element Nb is only produced by the decay of ^{93}Zr (half-life = 1.5 million years, down to 0.3 million years at 300

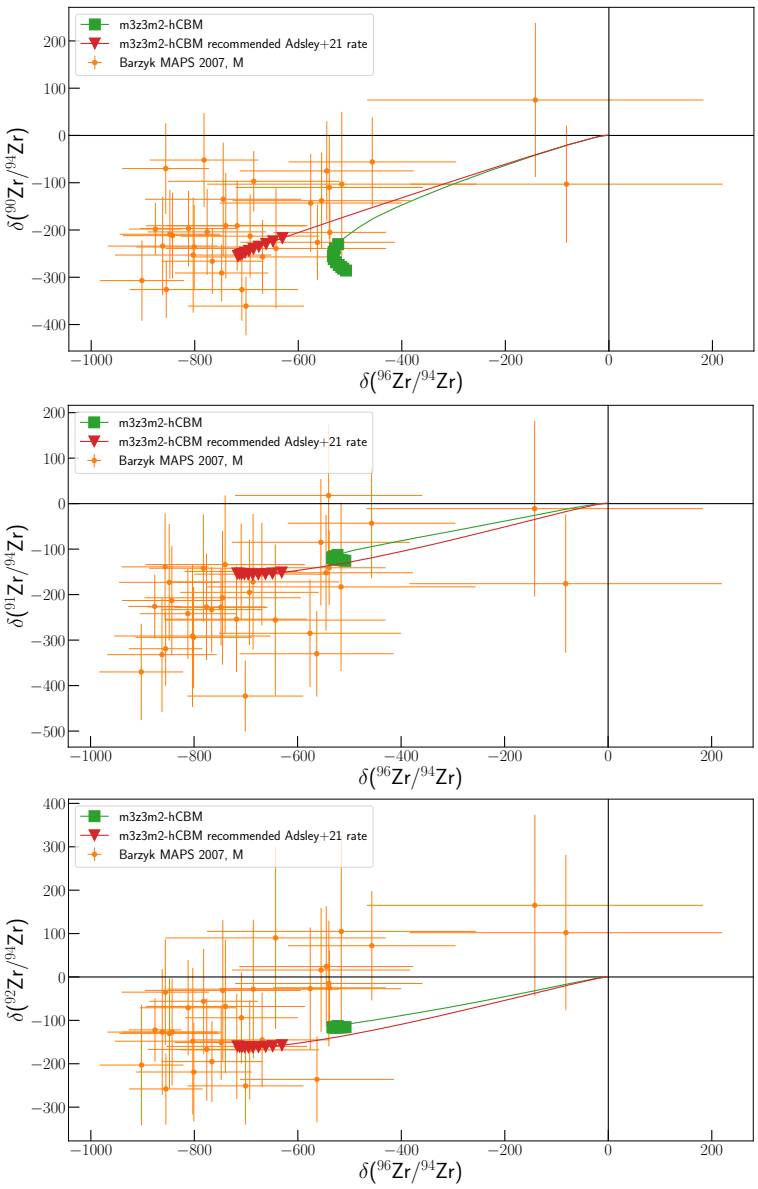

Figure 3.16 *The same as Figure 3.13, for m3z3m2-hCBM with and without the Adsley et al. [3] recommended reaction rates for* $^{22}Ne(\alpha,n)$ *and* $^{22}Ne(\alpha,\gamma)$.

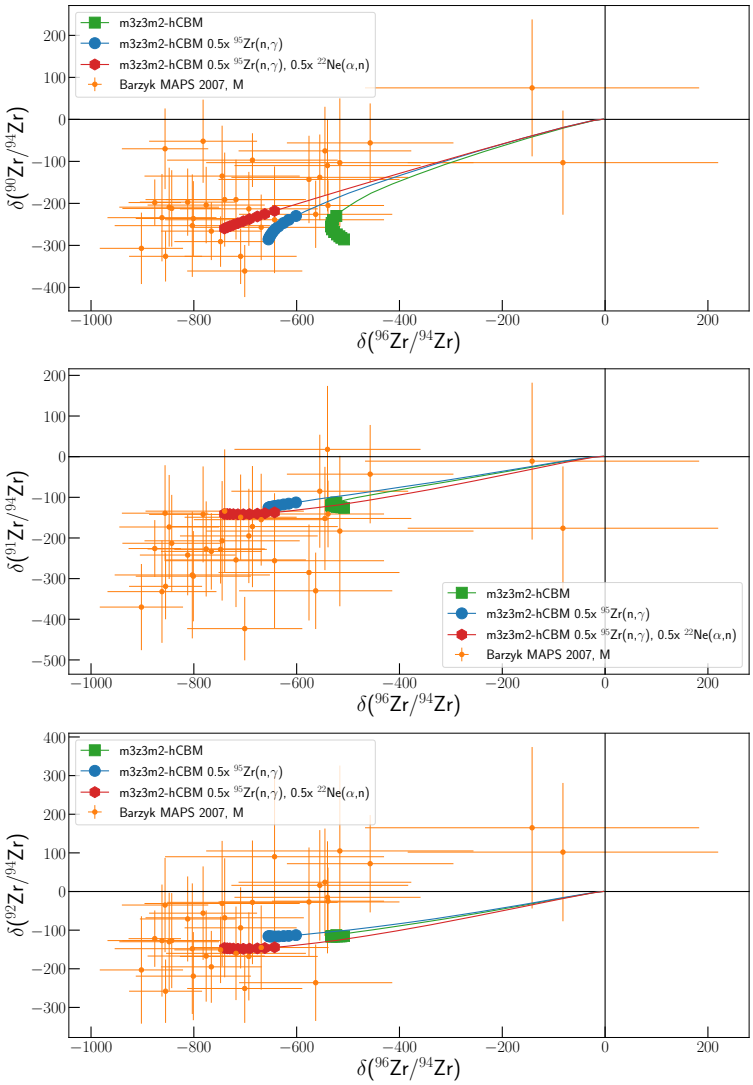

Figure 3.17 *The same as Figure 3.13, though the results show models calculated with a variation of key reaction rates that impact the observed isotopic ratios.*

MK; see Lugaro & Chieffi [133], Takahashi & Yokoi [198]). Due to the long half life of ^{93}Zr, this isotope is essentially stable on *s*-process time-scales, hence ^{94}Mo is only produced by the depletion of pre-existing ^{93}Nb. In addition, ^{94}Nb and ^{95}Nb are branching points and part of the reaction flow is bypassing ^{94}Mo and ^{95}Mo.

Figures 3.18-3.20 show predictions of isotopic ratios compared to Barzyk et al. [8] measurements. In general, the *set1-update* models reproduce data points from the grains data with the exception of ^{95}Mo/^{96}Mo and ^{100}Mo/^{96}Mo. This could be explained by the nuclear reaction rates used in the model. The default cross sections for Mo isotopes come from Kadonis v0.3. However the new version Kadonis v1.0 recommends a cross section that is 20% smaller for ^{13}C-pocket temperatures (kT=10 keV). In general, there are only few experimental data available for this reaction, from over 30 years ago. Hence, in Figure 3.19 the impact of using Kadonis v1.0 for all the Mo reaction rates is explored (model denoted with suffix kad1). The change to Kadonis v1.0 gives a better comparison to the grains data, but the best fit to the observed ratios can be obtained when using a 0.75x factor on the default ^{96}Mo(n,γ)^{97}Mo MACS, which is within the uncertainty of the Kadonis v1.0 cross section. The plots also include result from the hCBM models with scaled ^{96}Mo(n,γ)^{97}Mo, and RI18 for reference. *set1-update* models generally perform better compared to RI18. The *set1-update* models perform best when the 0.75x scale factor is adopted, where the models evolution track intersect the grain measurement data points. The models are not able to reproduce the measured spread of ^{95}Mo/^{96}Mo and ^{100}Mo/^{96}Mo. The $m3z2m2$ model without the scale factor covers most of the mean range of ^{98}Mo/^{96}Mo, but the $m3z2m2 - hCBM$ model with the scaling factor can reach the most deficient values. The other models still cover a good portion of the grains data without any scale factors. The impact of the ^{96}Mo(n,γ)^{97}Mo reaction rate is significant as it affects all ratios presented, hence new experimental data on this cross section are essential for improving stellar model predictions. Finally, it can be noted that the lowest ^{92}Mo/^{96}Mo value from the grains measurements could be reproduced with one extra TDU event, this is possible within the uncertainty of the *m3z2m2-hCBM* model combined with the Kadonis v1.0 reaction rate.

It should be noted that there is now new experimental data on ^{95}Mo stellar cross section (Koehler [112]), resulting in a 24% higher cross section for ^{95}Mo(n,γ) compared to the NuGrid default rate. A test of using the new rate, i.e. scaling the default rate by 1.24 leads to a better agreement of ^{95}Mo/^{96}Mo isotopic ratios

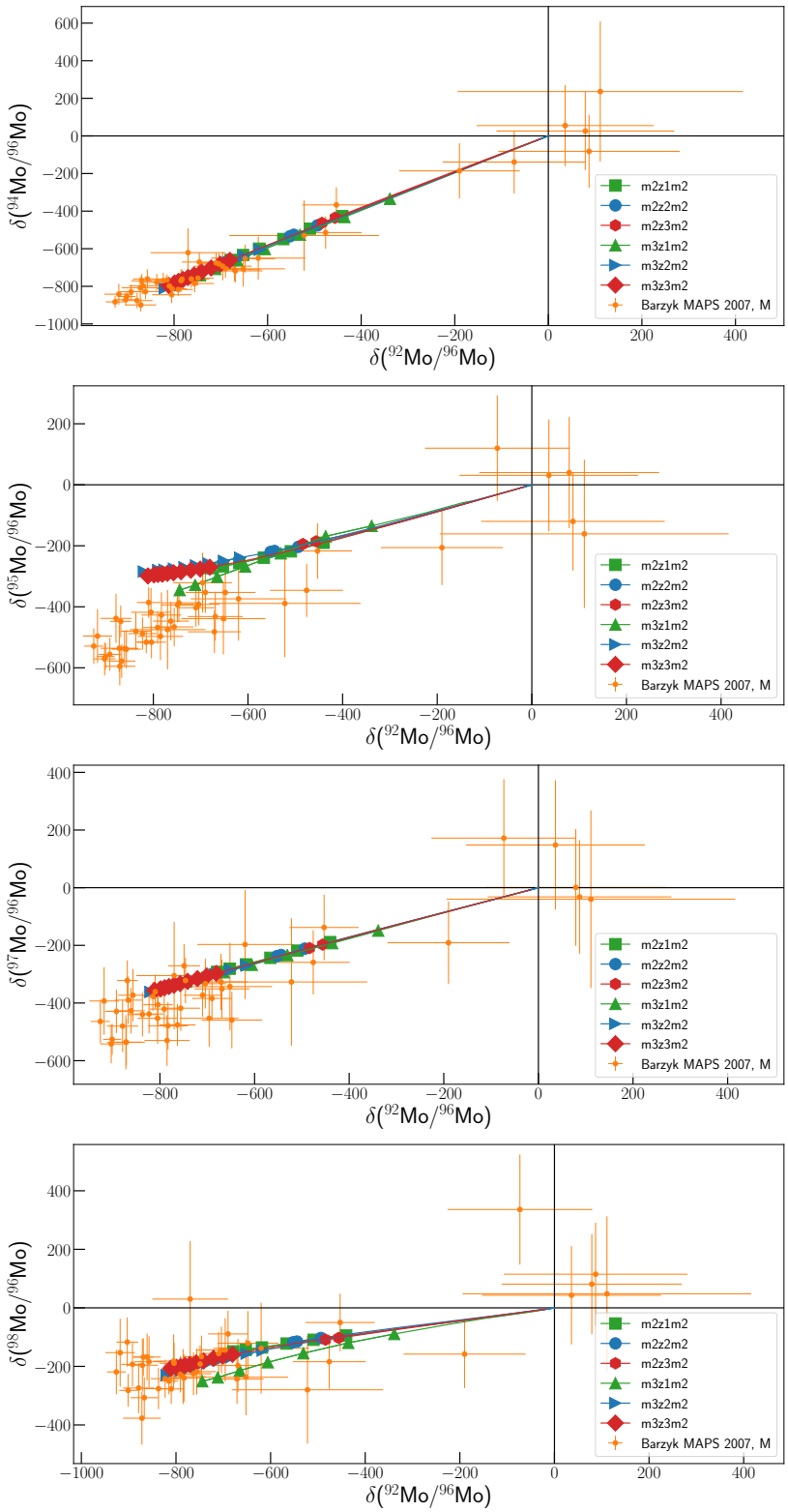

Figure 3.18 *Comparison of stellar models presented in this work with Barzyk et al. [8] measured molybdenum isotopic ratios from mainstream pre-solar silicon carbide grains.*

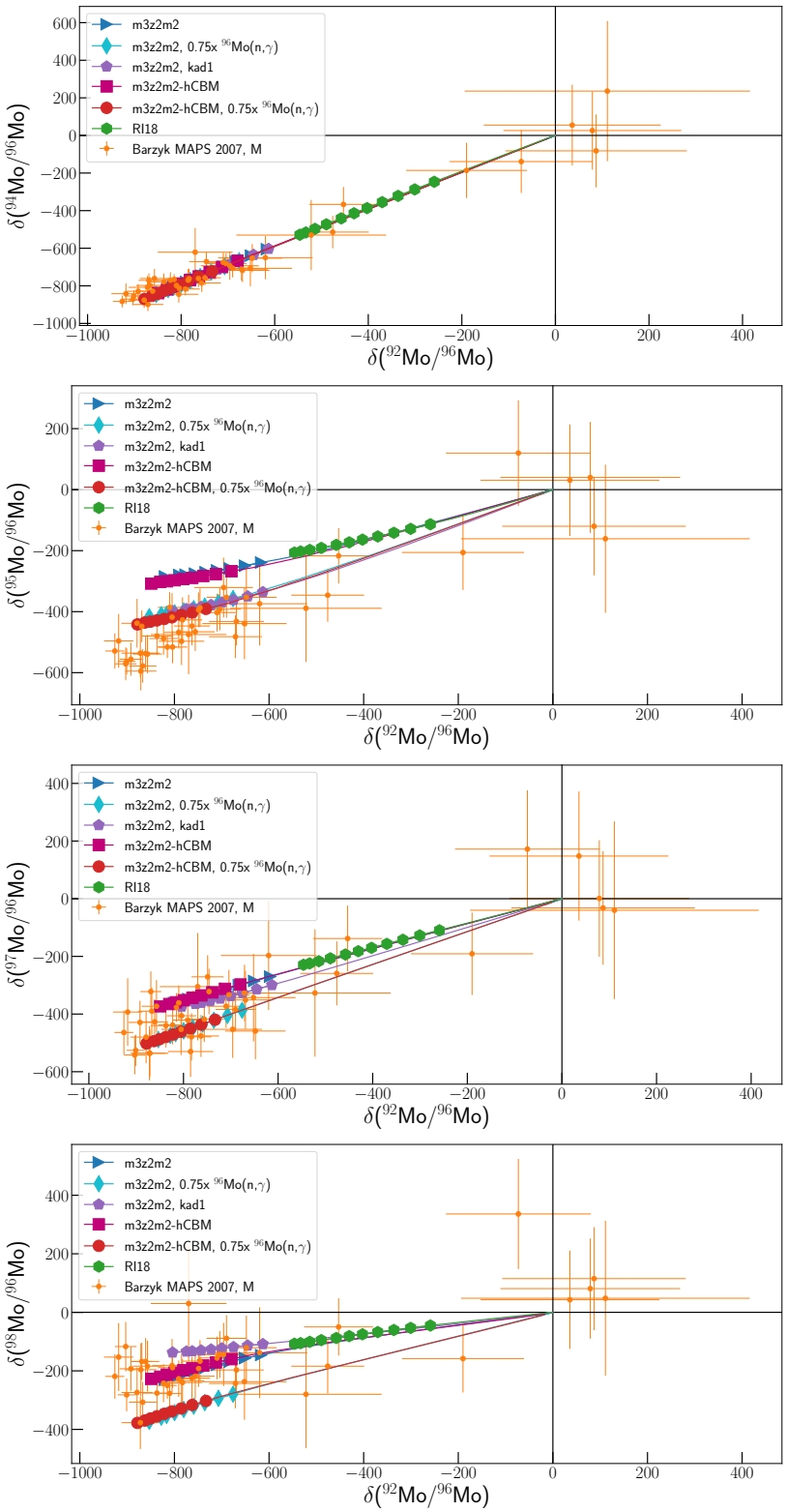

Figure 3.19 *The same as Figure 3.18, but the m3z2m2 model predictions are calculated with Kadonis v1.0, the m3z2m2 and m3z2m2-hCBM are calculated with the $^{96}Mo(n,\gamma)^{97}Mo$ Mo set to its lower limit of Kadonis v0.3 (i.e. multiplied by a factor 0.75).*

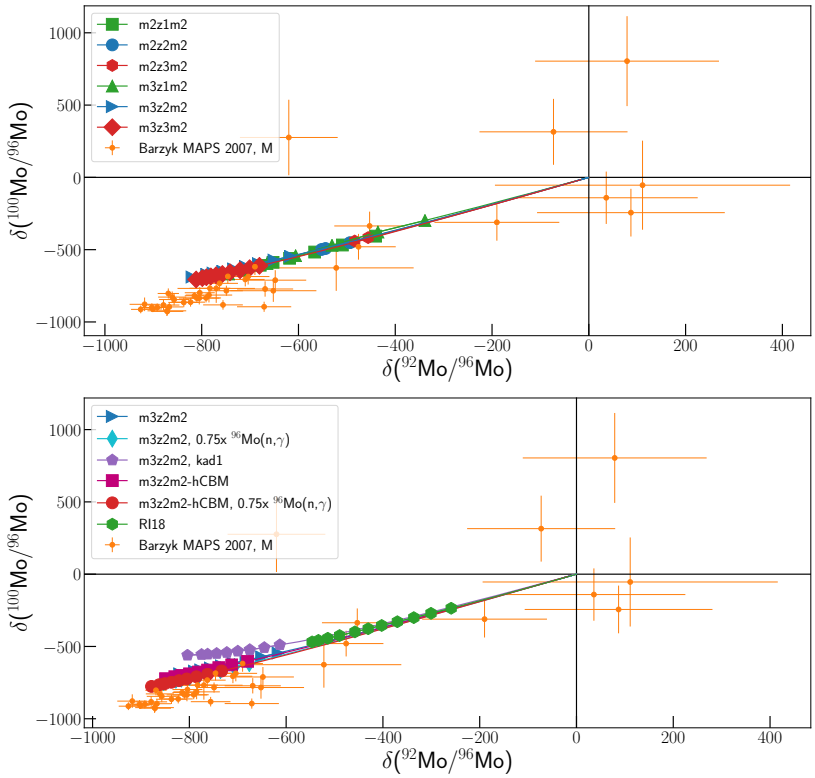

Figure 3.20 *The same as Figure 3.18, but the predictions are for $^{100}Mo/^{96}Mo$ versus $^{92}Mo/^{96}Mo$ ratios, included are the reaction rate test covered in Figure 3.19.*

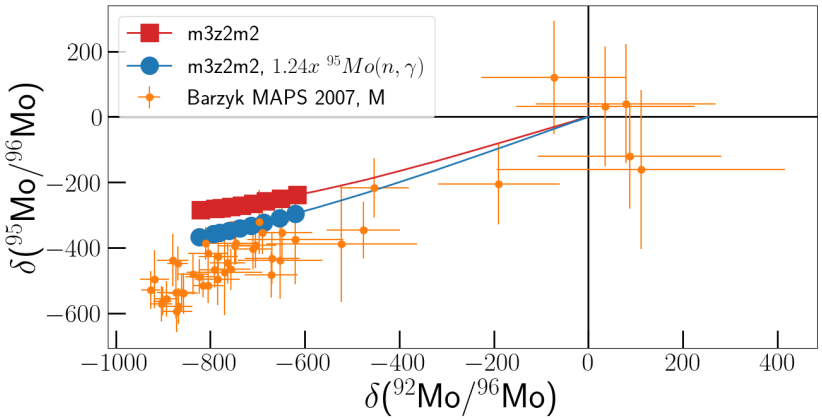

Figure 3.21 *$^{95}Mo(n,\gamma)$ adopting a factor of 1.24 to update the Kadonis v0.3 reaction rate to the Koehler [112] with a comparison to the Kadonis v0.3 reaction rate.*

as shown in Figure 3.21.

3.4 Ejected Yields

Mass loss occurs through the life of an AGB stars. The material ejected (yield) has been calculated for all *set1-update* and RI18 models using the NuGrid python tool NuGridPy (https://github.com/NuGrid/NuGridPy). The yields provided for Cr11 (Cristallo et al. [44]) are available from the FRUITY database (http://fruity.oa-teramo.inaf.it/) and Ka10 (Karakas [104]) are provided as supplementary data online. Table 3.2 shows a comparison of yield results for *m3z2m2* and the model with same initial mass and metallicity from RI18, Cr11 and Ka10. Investigating ^{12}C, ^{14}N, and ^{16}O in ejected yields are used as "tracers" for CNO cycling, the energy production cycle in the convective hydrogen envelope of AGB stars (Cristallo et al. [46, 47], Karakas [104]), and hence these isotopes are compared for all 4 models. Figure 3.22 presents light isotopes at the end of the AGB phase, comparing ^{12}C (the seed for ^{13}C), ^{14}N and ^{16}O between $m3z2m2$, RI18, Cr11 and Ka10. ^{12}C and ^{16}O achieve significantly higher yields in $m3z2m2$ and RI18 compared to Cr11 and Ka10. This comes from the different CBM scheme applied to the bottom of the helium inter-shell during the TP. In m3z2m2 and RI18, CBM is active at the bottom of the PDCZ leading to mixing of the helium burning products carbon and oxygen from the core into the inter-shell. Yields for the neutron poison ^{14}N, which comes from CNO burning, are similar between all models, with the largest difference being 20% with Ka10,

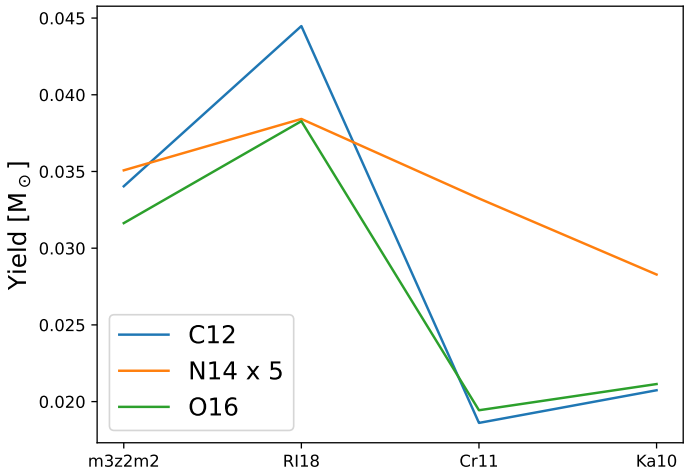

Figure 3.22 *A comparison of the ejected yield for key light isotopes between set1-update, RI18, FRUITY, and the Monash group for a $3M_{\odot}$ with metallicity, $Z = 0.02$. Values taken from Table 3.2.*

while agreeing with the other models within 10%.

Figure 3.23 compares the key *s*-process isotopes ^{88}Sr, ^{138}Ba, and ^{208}Pb between the models, representative of first, second and third *s*-process peaks. For all 3 isotopes, RI18 yields are about a factor of 2 smaller than $m3z2m2$ coming from the smaller ^{13}C-pockets. Similar yields to $m3z2m2$ are obtained by Cr11 for Ba and, whereas Sr is around 5 times larger, due to the larger ^{13}C-pockets in the FRUITY model. When comparing overall values in Table 3.2, $m3z2m2$ ejects more light elements than Cr11 and Ka10, but slightly less than RI18, while $m3z2m2$ ejects more *s*-process material than RI18, and is comparable to Cr11.

Isotope	m3z2m2 [$M_\odot$]	RI18 [$M_\odot$]	Cr11 [$M_\odot$]	Ka10 [$M_\odot$]
^{12}C	3.4035341E-02	4.448E–02	1.86110E–02	2.0739544E–02
^{13}C	2.2231664E-04	2.252E–04	2.20200E–04	1.9436399E–04
^{14}N	7.0151267E-03	7.685E–03	6.64840E–03	5.6565693E–03
^{15}N	4.4046608E-06	4.207E–06	4.29400E–06	5.0818235E–06
^{16}O	3.1633632E-02	3.828E–02	1.94360E–02	2.1144016E–02
^{17}O	6.2956708E-05	5.194E–05	7.91850E–05	5.5763638E–05
^{18}O	3.4374702E-05	3.364E–05	3.12110E–05	3.6596495E–05
^{19}F	4.9649986E-06	7.655E–06	3.68770E–06	4.3487280E–06
^{20}Ne	4.2225594E-03	4.356E–03	3.63520E–03	3.7571993E–03
^{21}Ne	1.2744558E-05	1.270E–05	9.90460E–06	1.0039988E–05
^{22}Ne	2.7187524E-03	3.937E–03	2.32210E–03	2.1113991E–03
^{23}Na	1.4976682E-04	1.772E–04	1.87730E–04	1.2845088E–04
^{24}Mg	1.3712457E-03	1.421E–03	1.84710E–03	1.1949923E–03
^{25}Mg	2.9955618E-04	2.915E–04	2.43210E–04	1.6784266E–04
^{26}Mg	4.5746367E-04	4.726E–04	2.88120E–04	1.9374024E–04
^{27}Al	1.5420979E-04	1.585E–04	2.08100E–04	1.3861095E–04
^{28}Si	1.7175335E-03	1.770E–03	2.36270E–03	1.5164100E–03
^{29}Si	9.2162458E-05	9.501E–05	1.24570E–04	7.9920115E–05
^{30}Si	6.7840128E-05	6.975E–05	8.60130E–05	5.5390818E–05
^{31}P	1.7451779E-05	1.771E–05	2.28230E–05	1.9017965E–05
^{33}S	7.9125730E-06	8.331E–06	1.04160E–05	7.6937777E–06
^{34}S	4.5194069E-05	4.601E–05	5.91400E–05	4.3391171E–04
^{54}Fe	1.8268714E-04	1.874E–04	2.49280E–04	1.6390771E–04
^{56}Fe	3.0096567E-03	3.100E–03	4.08090E–03	2.7071363E–03
^{57}Fe	8.1660429E-05	8.781E–05	1.02140E–04	7.2351380E–05
^{58}Fe	2.9018441E-05	3.211E–05	1.76610E–05	1.1919641E–05
^{59}Co	1.3762730E-05	1.441E–05	1.33220E–05	8.5931824E–06
^{58}Ni	1.2853806E-04	1.317E–04	1.71330E–04	1.1363259E–04
^{60}Ni	5.5129775E-05	5.698E–05	6.93570E–05	4.5602490E–05
^{61}Ni	3.9916327E-06	4.122E–06	3.46150E–06	8.8770785E–06
^{62}Ni	1.0936648E-05	1.056E–05	1.04870E–05	5.0042019E–08
^{64}Ni	4.0636092E-06	3.165E–06	3.32430E–06	-
^{88}Sr	3.3440015E-07	1.978E–07	1.63060E–06	-
^{89}Y	9.2306586E-08	5.072E–08	3.17410E–07	-
^{90}Zr	9.6840845E-08	5.726E–08	3.24600E–07	-
^{136}Ba	2.1123224E-08	9.317E–09	2.79920E–08	-
^{138}Ba	1.9605483E-07	7.581E–08	1.68590E–07	-
^{139}La	2.2851196E-08	9.138E–09	2.00170E–08	-
^{208}Pb	3.2787968E-08	2.243E–08	4.82470E–08	-

Table 3.2 *Total yield abundances for key s-process isotopes from m3z2m2, RI18, Cr11 and Ka10 for a 3$M_\odot$ with Z=0.02 stellar model.*

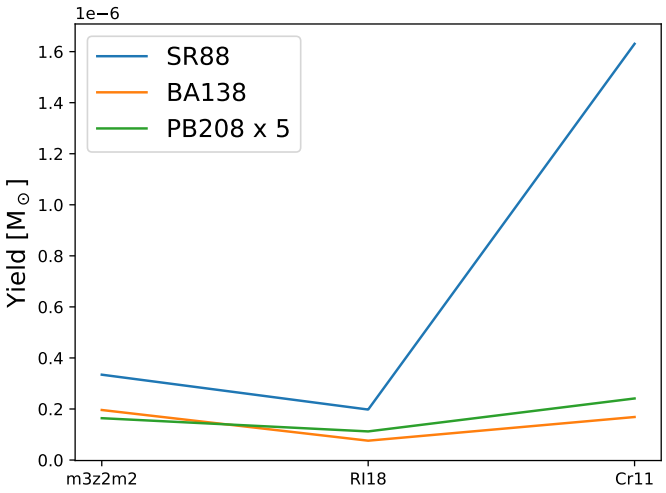

Figure 3.23 *Comparison of key isotopes from the three s-process peaks between set1-update, RI18, FRUITY, and the Monash group for a $3M_{\odot}$ with metallicity, $Z = 0.02$. Values taken from Table 3.2.*

Chapter 4

Uncertainties of Surface Abundances and Stellar Yields

4.1 Introduction

Uncertainties in predicted surface abundances and stellar yields can come from the assumptions and/or approximations made in stellar models, and from uncertainties in the nuclear physics input. In Chapter 3, the impact of uncertainties in the mixing descriptions was discussed for specific cases. In this chapter, a novel approach is described aimed at realistically estimating uncertainties of stellar yields and surface abundances due to uncertainties in the nuclear physics input, specifically neutron capture rates, neutron poison reactions and neutron production reactions. Studying abundance uncertainties due to nuclear physics uncertainties is essential to interpret how well a stellar model reproduces observables (as discussed already in Chapter 3), while uncertainties in stellar yields are of significant interest to galactic chemical evolution studies. Yields from stellar models are used in galactic chemical evolution simulations to investigate abundance distributions in our Galaxy (Côté et al. [36, 37], Cristallo et al. [41], Kobayashi & Ibrahim [110], Kobayashi et al. [111], Pignatari et al. [170]). This can, for example, be used to find regions with similar abundance to the solar neighbourhood which lie in the galactic habitable zone. Earth sized planets formed in the galactic habitable zone could have conditions similar to Earth so could support carbon based life like on Earth (Lineweaver et al. [126], Spitoni et al. [189]).

The methodology presented here is based on determination of the most important (key) reaction rates for a particular abundance ratio using Monte Carlo techniques and single zone calculations in PPN (this is a similar approach described by Cescutti et al. [29], Nishimura et al. [151, 152], Rauscher et al. [174, 175]). Subsequently, the effect of these key reaction rates on surface abundances and stellar yields are studied using full multi-zone nucleosynthesis calculations which include mixing. Section 4.2 describes the method of identifying key reactions, Section 4.3 presents the MPPNP studies for the key reaction rates, and the deduced uncertainties of surface abundances and stellar yields for one of the asymptotic giant branch (AGB) models (M=3 $M_{\odot}$ and Z=0.02) introduced in Chapter 3.

In this chapter, uncertainties are presented for specific isotopic and elemental ratios, which are relevant for pre-solar grain measurements and observed stellar spectra. All of these have already been discussed also in Chapter 3, with the exception of Zr/Fe, Y/Fe, La/Fe and Nd/Fe. These elemental ratios have been added as they are commonly used in comparisons of models and observations (Cseh et al. [49], de Castro et al. [53]).

4.2 Finding Key Reactions using Monte Carlo Approaches

4.2.1 Method

The first step is to find the most important (key) nuclear reaction rates that affect the abundances calculated from the stellar model, taking uncertainties of these reaction rates into consideration. The study is restricted to abundances that can be observed, i.e. isotopic ratios measured in meteoritic grains, and elemental ratios observed in stellar spectra (discussed in Chapter 3). Key reaction rates are identified using a Monte Carlo approach, which consists of running a nucleosynthesis simulation many times, where in each run reaction rates are randomly varied within their uncertainties. Rauscher et al. [174] has found that using 10000 Monte Carlo iterations can ensure that all possible combinations of reaction rates are well sampled. Since MPPNP simulations take a long time to run, the Monte Carlo study can only be completed in a realistic time frame by using single zone calculations, e.g. the PPN code. The single zone approach can give reliable results for nucleosynthesis in an environment where mixing

does not occur, such as the slow neutron-capture process (s-process) in the ^{13}C-pocket. For this study, a single zone model of an AGB star inter-pulse period was extracted from the $3M_{\odot}$ and Z=0.02 model (see Section 4.2.3). The importance of a nuclear reaction rate for a particular observable (isotopic or elemental ratio) was determined using the Pearson correlation coefficient, r which is defined as,

$$r_{xy} = \frac{\Sigma x_i y_i - n\bar{x}\bar{y}}{(n-1)s_x s_y} \tag{4.1}$$

where n is the size of the sample, and x_i is the individual sample points indexed by i. The mean $\bar{x}$ is defined as

$$\bar{x} = \frac{1}{n}\Sigma_{i=1}^{n} x_i, \tag{4.2}$$

with a standard deviation s_x defined as

$$s_x = \sqrt{\frac{1}{(n-1)}\Sigma_{i=1}^{n}(x_i - \bar{x})^2}, \tag{4.3}$$

with equivalent definition for the mean $\bar{y}$ and s_y. The Pearson correlation coefficient is a measure of the strength and direction of the relationship between two variables. Thus, it is essentially a normalized measurement of the covariance, such that the result always has a value between -1 and 1. Figure 4.1 demonstrates how the Pearson coefficient categorises data in a scatter plot, with values close to 1 and -1 showing a clear linear relationship or 0 representing no relationship. It is also assumed that a change in one reaction rate does not change the effect a change of another reaction rate has on the abundance.

Figure 4.2 shows how two reaction rates affect the abundance of a given isotope or element. It is not only important how sensitive a reaction rate is to the resultant abundance, but also how uncertain this reaction rate is. In this case rate B dominates the abundance uncertainty due to its larger reaction rate uncertainty although the abundance is less sensitive to reaction B compared to reaction A (i.e. the slope is less steep). While a single reaction rate test determines the importance of a rate according to the gradient $\frac{dY}{dR}$, a Monte Carlo variation test of multiple reaction rates varied within their uncertainties reveals the scatter of the correlation between reaction rate variation and abundance. From the Monte Carlo method, a Pearson correlation coefficient closer to -1 would be obtained for rate B compared to A (negative, because the gradient is negative).

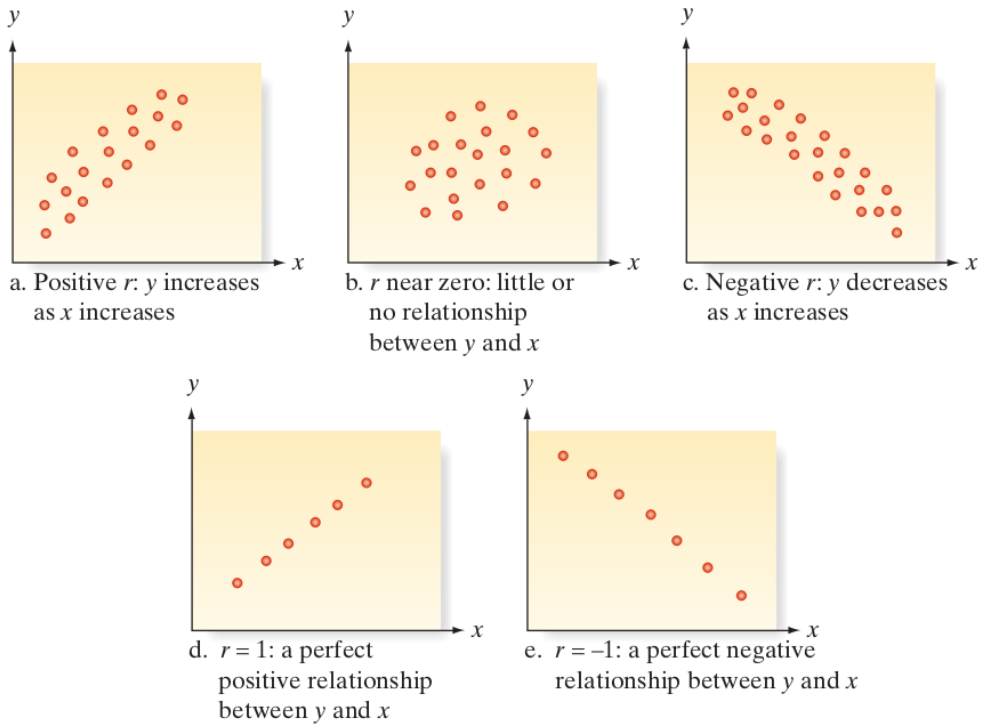

Figure 4.1 *Comparison of Pearson coefficients for different scatter plots. Taken from page 646 of McClave & Sincich [148].*

In Rauscher et al. [174], where the technique of using Pearson correlation coefficients to define what is a key reaction rate was applied for the first time, a correlation of r > 0.65 or r < -0.65 was considered significant. In this work, any correlation of r < -0.5 or r > 0.5 is considered important, taking into consideration that the correlations found using PPN could be different compared to MPPNP. Reactions with these r values are called key rates.

4.2.2 Nuclear Reaction Network and Uncertainties

The nuclear reaction network used in this work is the standard NuGrid reaction network (Battino et al. [10, 11, 13]). The neutron capture reactions in this network are largely based on recommendations listed in the Kadonis 0.3 database (Dillmann et al. [63]), which also contains uncertainties of the stellar cross sections, which have been adopted for the Monte Carlo study. However, other data have been used for a few selected reactions:

- For ^{80}Kr(n,γ) and ^{83}Kr(n,γ) MACS were taken from Mutti et al. [150], however only statistical uncertainties were given so a 5% uncertainty was assumed following the recommendation in Kadonis 1.0 (Reifarth [179]).

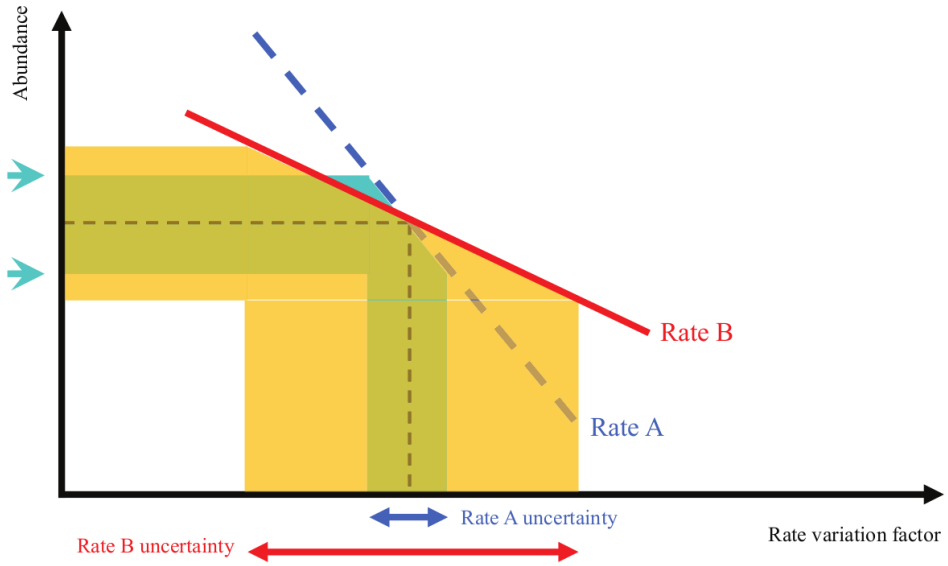

Figure 4.2 *Schematic showing the impact of reaction rate variations on the variation of a final abundance. Both reactions are assumed to contribute to the variation in the final abundance and the gradient of the two lines is given to represent the change in the reaction rates. Positive gradients are for production reactions, and negative gradients for reactions reducing the abundance of a nuclide. In a Monte Carlo study, the abundance scatters for changes in rate A (dashed blue line) due because rate B (full red line) changes in random amounts at the same time with a larger variation. From the plot the final abundance is more sensitive to rate A because of its steeper gradient, but the final abundance uncertainty is dominated by rate B because its reaction rate uncertainty is larger than the that of rate A. Taken from Rauscher et al. [174].*

- For ^{84}Sr the older theoretical value in Bao et al. [7] was used. Since ^{84}Sr is a p-only nucleus this will not impact on the final results.
- For Zr isotopes the new evaluation from Lugaro et al. [139] was used.
- The stellar ^{14}N(n,p) cross section is by default the theoretical value from Caughlan & Fowler [28]. Recently, a measurement by Wallner et al. [213] obtained a 15% smaller value with an uncertainty of 3%. Thus, a 20% uncertainty was assumed for the default ^{14}N(n,p) stellar cross section in this study.
- The ^{13}C(α,n) reaction rate (and uncertainty) is taken from Heil et al. [86]. It should be noted that since this study, there have been new results by the JUNA (Liu et al. [130]) and LUNA (Ciani et al. [32], Csedreki et al. [48]) collaborations, both of which are within 1 σ of the uncertainty quoted by Heil et al. [86]. With either rate mentioned the ^{13}C-pocket is completely consumed during the inter-pulse period.
- The ^{22}Ne(α,n) reaction rate comes from Jaeger et al. [100], and ^{22}Ne(α,γ) from the NACRE compilation. There is a new evaluation of these reaction rates by Adsley et al. [3], suggesting significantly smaller reaction rates. Uncertainties for these rates have been assumed as a factor of 320% and 400% for ^{22}Ne(α,n) and ^{22}Ne(α,γ), respectively. This is to include the lower bound of the rates given in Adsley et al. [3] in the Monte Carlo tests. The reactions are not significant on ^{13}C-pocket burning, hence did not produce Pearson coefficients above the threshold. While they are important in the thermal pulse, this uncertainty was investigated in MPPNP runs and hence is not included in the uncertainties shown later. However, the impact of the Adsley et al. [3] evaluation is shown for specific isotopic and elemental ratios in Chapter 3, Figures 3.8 and 3.16.
- For theoretical reaction rates, a factor 2 was assumed for the uncertainty. This affects mainly neutron capture on unstable nuclei, i.e. branching point nuclei, where experimental measurements are extremely challenging. Branching points are most impactful during the thermal pulse, when neutron densities are typically 2 orders of magnitude higher compared to the ^{13}C-pocket. A list of branching points and their uncertainties is in Table 4.1.

A full list of reactions and uncertainties is in Appendix A.1.

Reaction	Factor	Reaction	Factor	Reaction	Factor
^{35}S(n,γ)	2.000	^{36}Cl(n,γ)	2.000	^{41}Ca(n,γ)	2.000
^{45}Ca(n,γ)	2.000	^{59}Fe(n,γ)	2.000	^{63}Ni(n,γ)	1.301
^{64}Cu(n,γ)	2.000	^{65}Zn(n,γ)	2.000	^{71}Ge(n,γ)	2.000
^{79}Se(n,γ)	2.000	^{80}Br(n,γ)	2.000	^{81}Kr(n,γ)	2.000
^{85}Kr(n,γ)	2.000	^{86}Rb(n,γ)	2.000	^{89}Sr(n,γ)	2.000
^{90}Sr(n,γ)	2.000	^{91}Y(n,γ)	2.000	^{93}Zr(n,γ)	1.093
^{95}Zr(n,γ)	2.000	^{94}Nb(n,γ)	2.000	^{95}Nb(n,γ)	2.000
^{99}Tc(n,γ)	1.064	^{107}Pd(n,γ)	1.045	^{128}I(n,γ)	2.000
^{133}Xe(n,γ)	2.000	^{134}Cs(n,γ)	2.000	^{135}Cs(n,γ)	1.063
^{136}Cs(n,γ)	2.000	^{137}Cs(n,γ)	2.000	^{141}Ce(n,γ)	2.000
^{142}Pr(n,γ)	2.000	^{143}Pr(n,γ)	2.000	^{147}Nd(n,γ)	2.000
^{147}Pm(n,γ)	1.141	^{148}Pm(n,γ)	2.000	^{151}Sm(n,γ)	1.022
^{153}Sm(n,γ)	2.000	^{152}Eu(n,γ)	2.000	^{154}Eu(n,γ)	1.152
^{155}Eu(n,γ)	1.064	^{153}Gd(n,γ)	2.000	^{163}Dy(n,γ)	1.010
^{163}Ho(n,γ)	1.045	^{164}Ho(n,γ)	2.000	^{169}Er(n,γ)	2.000
^{170}Tm(n,γ)	2.000	^{171}Tm(n,γ)	2.000	^{176}Lu(n,γ)	1.009
^{177}Lu(n,γ)	2.000	^{179}Hf(n,γ)	1.009	^{181}Hf(n,γ)	2.000
^{179}Ta(n,γ)	2.000	^{180}Ta(n,γ)	1.068	^{182}Ta(n,γ)	2.000
^{183}Ta(n,γ)	2.000	^{185}W(n,γ)	1.108	^{186}Re(n,γ)	2.000
^{191}Os(n,γ)	2.000	^{192}Ir(n,γ)	2.000	^{193}Pt(n,γ)	2.000
^{204}Tl(n,γ)	2.000	^{205}Pb(n,γ)	2.000	^{210}Bi(n,γ)	2.000

Table 4.1 *The list of isotopes that are branching points during TP nucleosynthesis with there respective uncertainty factor. The list of isotopes is taken from Lugaro & Chieffi [133]. It is of note that many reactions have a factor 2, since only theoretical estimations are available.*

4.2.3 Monte Carlo Simulations and Results

The Monte Carlo code was written in python from the ground up, with options to select; the reaction types, the multiplication factors, the specific isotopes of interest, and the total number of reactions. The Monte Carlo framework structures each PPN with a uniquely defined networksetup.txt file. The networksetup.txt files contains all reactions used in the simulation with any factor used for specific reaction rates. Using the setup program prep_mc_network.py, any number of samples can be generated, it is recommended to use at least 10000 as stated previously. Running the Monte Carlo simulations is similar to performing a PPN simulation, but is started by running the bash script onezone_MC_sims.sh rather than the PPN executable file. Each run will have a numbered output and setup file ending in _n.txt where n is a number between 0 and the maximum number of runs, in this case 10000 is the default, these output files are located in the output and the initial networksetup files are contained in the setup folder. PPN is then run, and the last cycle number is then copied from the PPN directory to a results directory, any output file, this includes the x-time.dat file which contains the abundance data from all output cycle files can be chosen. This is easily done by editing the last line of the bash script. The analysis is handled by a few python scripts written to organise the raw data and filter non essential data.

In the Monte Carlo framework reaction rates are varied randomly within the range of its uncertainty. The Monte Carlo framework generates a list of 10,000 random factors for each reaction rate, there are 359 reactions relevant to the *s*-process not including beta decay rates, of which 355 are neutron capture reaction rates for the *s*-process and 4 reaction rates involving charged particles, which correspond to neutron source or poison reactions. The experimentally derived reaction rates, usually of stable isotopes are varied in a log normal distribution (Carobbi et al. [25], Iliadis et al. [99], Žerovnik et al. [224]) with a 1σ standard deviation corresponding to the reaction uncertainty. The theoretically evaluated reaction rate factors which are assumed to have a factor of 2 uncertainty use a uniform distribution. Figure 4.3 shows an example distribution of reaction rate factors for an experimentally known reaction (^{13}C(α,n)), and a reaction where only theoretical estimations are available (^{14}N(n,γ)). Table 4.2 lists the key reactions for observables discussed in Chapter 3, obtained from the PPN simulations, i.e. reactions which exhibited a Pearson coefficient above 0.5 or below -0.5 (see Figure 4.4 for an illustration of Pearson coefficients).

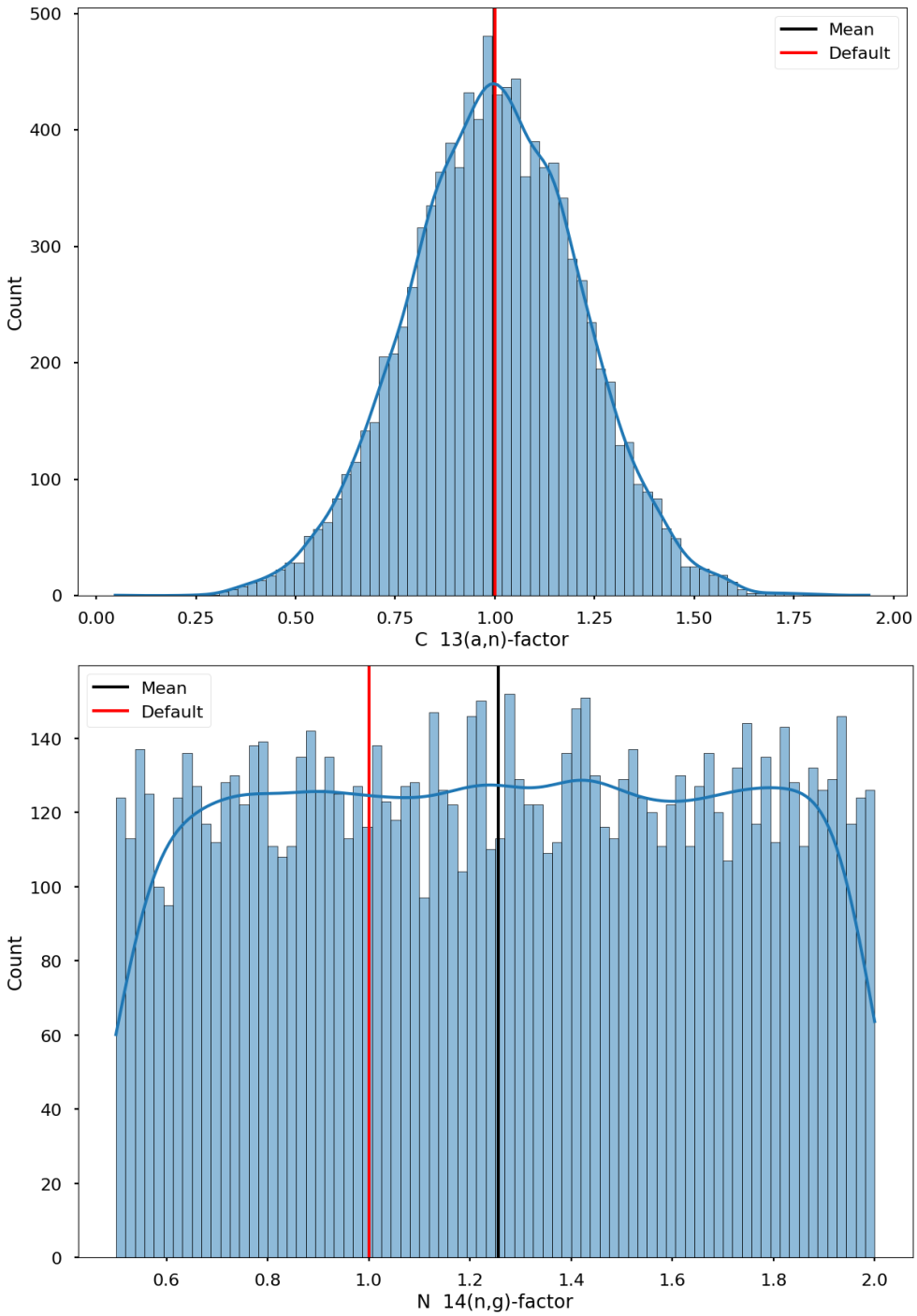

Figure 4.3 *Example of the reaction rate variation factors applied for the $^{13}C(\alpha,n)$ (top) and $^{14}N(n,\gamma)$ (bottom) reaction rates. In the case of $^{13}C(\alpha,n)$ the stellar cross section is known experimentally, so the reaction rate was varied following a log normal distribution with 1 σ corresponding to the 1 σ uncertainty. For the case of $^{14}N(n,\gamma)$, the cross section is only know theoretically, so an uncertainty of a factor 2 was assumed and the distribution was sampled uniformly between minimum and maximum possible value.*

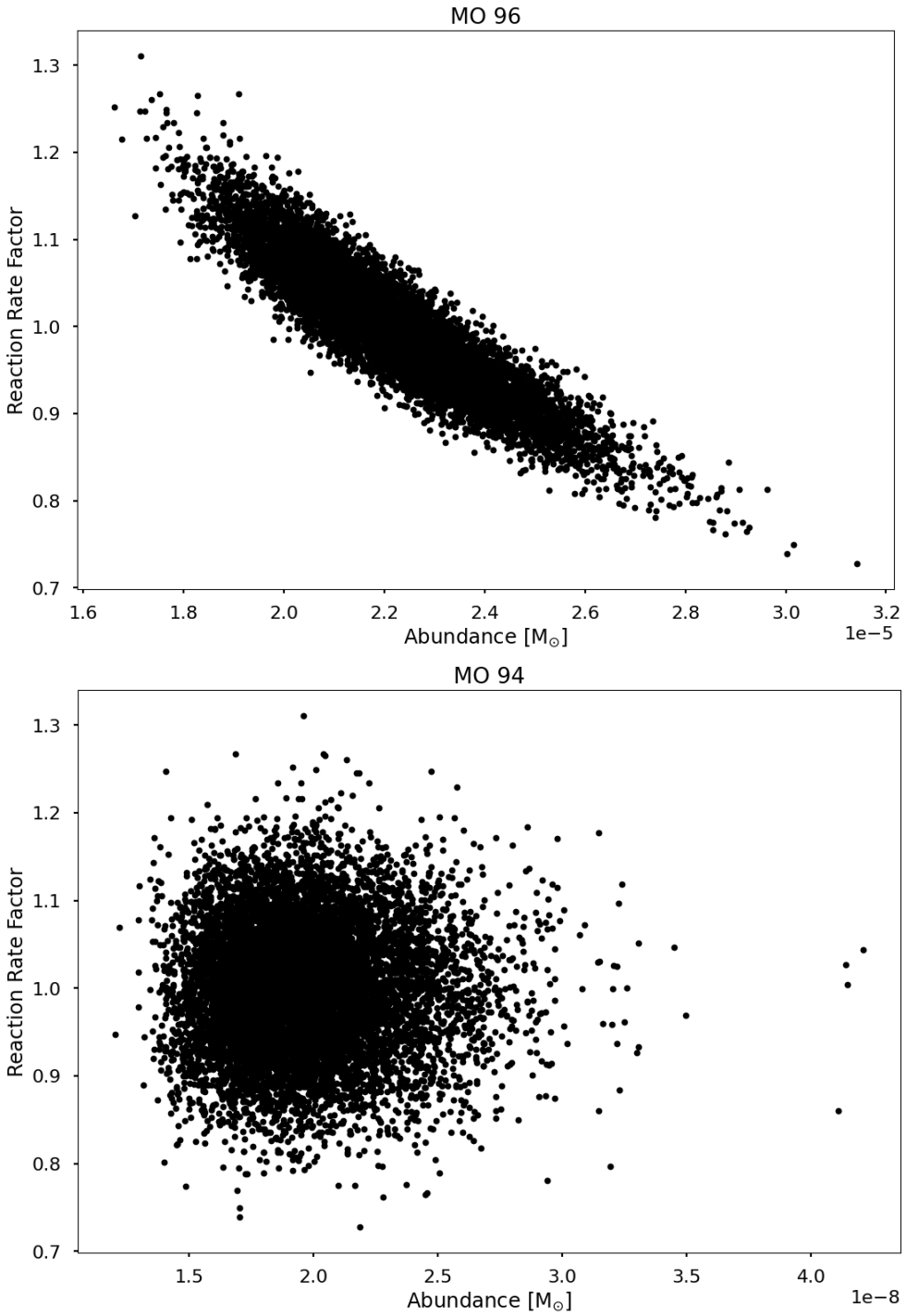

Figure 4.4 *Final abundances vs. reaction rate variation for a particular reaction obtained from 10000 Monte Carlo runs. The upper panel presents the ^{96}Mo abundances against $^{96}Mo(n,\gamma)$ factors with a Pearson coefficient of close to -1, while the lower panel shows the ^{94}Mo abundance for different $^{96}Mo(n,\gamma)$ rates, where no correlation is expected, and indeed, observed.*

The trajectory used in this study was taken from the $m3z2m2$ model at the center of the ^{13}C-pocket formed after the 16^{th} thermal pulse (TP) had ended. This ^{13}C-pocket was chosen because it was large but early in the carbon-rich phase of the evolution so the star had not been heavily polluted by the s-process, so comparisons with more polluted ^{13}C-pocket could be made. Abundances were taken after the TP, this is to ensure all material in the helium inter-shell is homogeneous. Other trajectories were tested from the ^{13}C-pockets of the 6^{th}, 20^{th}, and 23^{rd} TPs. Results from the 20^{th} and 23^{rd} pulses only showed slight differences to the 16^{th}, and all inter-pulse periods were analysed for identification of key reactions. The 6^{th} inter-pulse period produced different results, however it is early in the AGB phase evolution and the ^{13}C-pocket is below the average size with a smaller ^{13}C peak value. For these reasons it was not used for further analysis. The initial abundance for each trajectory was taken from the first time step and at the same mass coordinate of the trajectory from the multi-zone simulation model.

Table 4.2 lists the key reactions found for the different ratios, obtained from the PPN simulations, i.e. reactions which exhibited a Pearson coefficient above 0.5 or below -0.5 (see Figure 4.4 for an illustration of Pearson coefficients). To identify secondary key reactions, the Monte Carlo run was repeated after removing the variation for specific key reactions affecting abundances globally, those reactions were ^{13}C(α,n), ^{14}N(n,p) and ^{56}Fe(n,γ).

As noted in the introduction, the approach used here is similar to the methodology developed in Rauscher et al. [175] and related publications. In particular, Cescutti et al. [29] have performed a similar sensitivity study for the main s-process in AGB stars. This study has some important differences to Cescutti et al.'s work: this work uses an AGB model of higher metallicity (Z=0.02 rather than Z=0.014), and focuses on the impact of nuclear reaction rate uncertainty on observable abundances, i.e. isotopic ratios that can be measured in meteoritic grains, and elemental abundances observed in stellar spectra. In addition, this work considers uncertainties in neutron capture, neutron source and neutron poison reactions, while Cescutti et al. [29] considers neutron capture and beta decay rates. None of the beta decay rate uncertainties were found to have a large impact in Cescutti et al. [29]'s study, therefore it was decided to not include them in the present study. Hence, small differences in the key reactions identified can be expected due to using a different stellar model, a slightly different stellar network, and a different definition of what represents a key reaction. For isotopic abundances, a

Ratio	Key reactions
^{84}Sr/^{86}Sr	^{84}Sr(n,γ)
^{87}Sr/^{86}Sr	^{86}Sr(n,γ), ^{87}Sr(n,γ)
^{88}Sr/^{86}Sr	^{88}Sr(n,γ), ^{86}Sr(n,γ), ^{14}N(n,p)
^{90}Zr/^{94}Zr	^{94}Zr(n,γ), ^{90}Zr(n,γ), ^{14}N(n,p)
^{91}Zr/^{94}Zr	^{94}Zr(n,γ), ^{91}Zr(n,γ)
^{92}Zr/^{94}Zr	^{92}Zr(n,γ), ^{94}Zr(n,γ)
^{96}Zr/^{94}Zr	^{95}Zr(n,γ)
^{92}Mo/^{96}Mo	^{92}Mo(n,γ)
^{94}Mo/^{96}Mo	^{94}Mo(n,γ), ^{93}Zr(n,γ)
^{95}Mo/^{96}Mo	^{96}Mo(n,γ), ^{95}Mo(n,γ)
^{97}Mo/^{96}Mo	^{96}Mo(n,γ), ^{97}Mo(n,γ)
^{98}Mo/^{96}Mo	^{98}Mo(n,γ), ^{96}Mo(n,γ)
^{100}Mo/^{96}Mo	^{100}Mo(n,γ), ^{99}Mo(n,γ)
^{134}Ba/^{136}Ba	^{134}Ba(n,γ), ^{136}Ba(n,γ), ^{14}N(n,p)
^{135}Ba/^{136}Ba	^{136}Ba(n,γ), ^{135}Ba(n,γ)
^{137}Ba/^{136}Ba	^{137}Ba(n,γ), ^{136}Ba(n,γ)
^{138}Ba/^{136}Ba	^{14}N(n,p), ^{136}Ba(n,γ)
Y/Fe	^{56}Fe(n,γ), ^{89}Y(n,γ), ^{14}N(n,p)
Zr/Fe	^{56}Fe(n,γ), ^{14}N(n,p)
La/Fe	^{139}La(n,γ), ^{14}N(n,p)
Ce/Fe	^{14}N(n,p), ^{16}O(n,γ)
Nd/Fe	^{14}N(n,p), ^{16}O(n,γ)

Table 4.2 *The key reactions identified by the Pearson correlation tests. The Monte Carlo run has also been performed without the reactions $^{13}C(\alpha,n)$, $^{14}N(n,p)$ and $^{56}Fe(n,\gamma)$. These reactions have a global impact on s-process abundances and may mask secondary key reactions. In the situation where reactions were removed, $^{16}O(n,\gamma)$ replaced $^{14}N(n,p)$ as a possible alternative neutron poison.*

direct comparison with the results from the ^{13}C-pocket of Cescutti et al. [29] is possible:

- Strontium ratios: Cescutti et al. [29] studied the impact of nuclear uncertainties on ^{86,87,88}Sr abundances and found that (n,γ) reactions on ^{86,87,88}Sr, respectively represented the most important uncertainties. This is in agreement with this work. Cescutti et al. [29] identified ^{56}Fe(n,γ) and ^{64}Ni(n,γ) as secondary important reactions, which was not replicated in this work. In addition this study found ^{14}N(n,p) to represent an important reaction, which was not considered in Cescutti et al. [29].

- Cescutti et al. [29] found that (n,γ) reactions on ^{90,92,94}Zr represented the most important uncertainties for ^{90,92,94}Zr abundances, respectively. For the isotopic ratios including those isotopes in this work, the same results are observed, with the addition of ^{14}N(n,p) for the ^{90}Zr/^{94}Zr isotopic ratios. Cescutti et al. [29] identified ^{64}Ni(n,γ) as a secondary important reaction for all isotopes, which was not replicated in this work.

- Molybdenum ratios: Only a comparison for ^{95,96,97,98}Mo can be made, which show the same findings. In addition Cescutti et al. [29] finds that ^{64}Ni(n,γ) is a secondary key rate, which is not obtained in this work.

- Barium ratios: Cescutti et al. [29] does not include ^{135}Ba abundances, but the other isotopes match with the following exceptions: the result for ^{134}Ba/^{136}Ba and ^{138}Ba/^{136}Ba includes ^{14}N(n,p) as an important reaction while Cescutti et al. [29] found ^{138}Ba(n,γ) to be a secondary key rate rate for ^{138}Ba abundances.

4.3 Determination of Abundance Uncertainties

For a realistic estimation of uncertainties in stellar surface abundances and stellar yields full calculations need to be performed using multi-zone simulations which take mixing processes into consideration. This is achieved by running MPPNP varying the most important reaction rates one at a time (1 σ up, 2 σ up, 1 σ down, 2 σ down) and extracting the resultant change in surface abundance and yield. The change in abundance due to a change in the nuclear reaction rate is considered as the uncertainty of that abundance due to a particular rate. To estimate the combined uncertainty due to uncertainties in several different reaction rates, the

individual abundance uncertainties are added in quadrature. This is assuming that the abundance uncertainty due to the uncertainty of one reaction rate is independent of the value/uncertainty of any other reaction rate. A more realistic estimation of the total uncertainty would require a Monte Carlo run with MPPNP. In Section 4.2 several nuclear reactions have been identified which significantly affect abundances predicted in the one-zone model PPN, called "key reactions". However, differences are expected for the MPPNP simulation which mimics the full evolution of a star including several repeated ^{13}C-pocket burning episodes, *s*-process during the thermal pulses, and mixing effects. In general reactions that have a global effect on *s*-process abundances (neutron source reactions, neutron poison reactions and neutron capture reactions with small cross sections) were found to have differing importance in MPPNP compared to PPN. Also, *p*-only and *r*-only nuclei showed differences between PPN and MPPNP. Therefore, PPN was not used for identifying key reactions during thermal pulse conditions. The thermal pulse does not contribute much to the overall abundances, but is responsible for modifying isotopic ratios since the higher neutron densities result in the opening of new branching points. Due to time constraints, the effect of branching point reactions was studied by simultaneously increasing or decreasing all branching points by 1σ and 2σ using MPPNP. The relevant reactions are shown in Table 4.1. This approach is only valid if branching points are sufficiently far apart from each other and are not affecting the abundances of the same isotopes. As will be discussed later, this is not the case for some of the isotopes studied.

Table 4.3 shows all the nuclear reactions which were used to calculate uncertainty abundances. They are listed in order of importance, i.e. the first reaction contributed most to the abundance uncertainty. In addition, the branching point reactions most likely to contribute to the uncertainty are listed in a separate column. These have been deduced from the flux plots shown in Figures 4.5 and 4.6. The plots show the reaction flows during ^{13}C-pocket burning at peak neutron density (top), and reaction flows during the 6^{th} TP at peak neutron density. The 16^{th} TP was chosen because the associated third dredge-up (TDU) is efficient enough to form a ^{13}C-pocket that is large enough to be representative of all other TDUs and ^{13}C-pockets that contribute to the surface enrichment. The TP plot was produced by extracting a trajectory from the bottom of the TP in the multi-zone model. The differences between the key reactions from the Monte Carlo study (Table 4.2) and the final list of stable isotope reactions used for the uncertainty calculation (Table 4.3) using the multi-zone calculations from MPPNP are the described here:

Ratio	Important ^{13}C-pocket Reactions	Branching Point Reactions
^{84}Sr/^{86}Sr	^{86}Sr(n,γ)	^{85}Kr(n,γ), ^{86}Rb(n,γ)
^{87}Sr/^{86}Sr	^{86}Sr(n,γ), ^{87}Sr(n,γ)	^{85}Kr(n,γ), ^{86}Rb(n,γ)
^{88}Sr/^{86}Sr	^{88}Sr(n,γ), ^{86}Sr(n,γ), ^{14}N(n,p), ^{13}C(a,n)	^{85}Kr(n,γ), ^{86}Rb(n,γ)
^{90}Zr/^{94}Zr	^{94}Zr(n,γ), ^{90}Zr(n,γ)	
^{91}Zr/^{94}Zr	^{94}Zr(n,γ), ^{91}Zr(n,γ)	
^{92}Zr/^{94}Zr	^{92}Zr(n,γ), ^{94}Zr(n,γ), ^{14}N(n,p)	
^{96}Zr/^{94}Zr		^{95}Zr(n,γ)
^{92}Mo/^{96}Mo	^{96}Mo(n,γ), ^{14}N(n,p)	^{95}Zr(n,γ)
^{94}Mo/^{96}Mo	^{96}Mo(n,γ), ^{14}N(n,p)	^{95}Zr(n,γ), ^{94}Nb(n,γ), ^{95}Nb(n,γ)
^{95}Mo/^{96}Mo	^{96}Mo(n,γ), ^{95}Mo(n,γ)	^{95}Zr(n,γ), ^{94}Nb(n,γ), ^{95}Nb(n,γ)
^{97}Mo/^{96}Mo	^{96}Mo(n,γ), ^{97}Mo(n,γ)	^{95}Zr(n,γ)
^{98}Mo/^{96}Mo	^{98}Mo(n,γ), ^{96}Mo(n,γ)	^{95}Zr(n,γ)
^{100}Mo/^{96}Mo	^{99}Mo(n,γ), ^{100}Mo(n,γ), ^{96}Mo(n,γ)	^{95}Zr(n,γ)
^{134}Ba/^{136}Ba	^{136}Ba(n,γ), ^{134}Ba(n,γ)	^{13}Xe(n,γ), ^{136}Cs(n,γ), ^{134}Cs(n,γ)
^{135}Ba/^{136}Ba	^{136}Ba(n,γ), ^{14}N(n,p)	
^{137}Ba/^{136}Ba	^{137}Ba(n,γ), ^{136}Ba(n,γ)	^{136}Cs(n,γ)
^{138}Ba/^{136}Ba	^{14}N(n,p), ^{136}Ba(n,γ), ^{138}Ba(n,γ), ^{13}C(a,n)	
Y/Fe	^{89}Y(n,γ), ^{14}N(n,p), ^{88}Sr(n,γ), ^{64}Ni(n,γ)	^{85}Kr(n,γ), ^{89}Sr(n,γ)
Zr/Fe	^{14}N(n,p), ^{90}Zr(n,γ), ^{94}Zr(n,γ), ^{92}Zr(n,γ), ^{88}Sr(n,γ), ^{64}Ni(n,γ)	
La/Fe	^{14}N(n,p), ^{139}La(n,γ), ^{13}C(a,n)	
Ce/Fe	^{14}N(n,p), ^{13}C(a,n), ^{140}Ce(n,γ), ^{138}Ba(n,γ), ^{16}O(n,γ)	
Nd/Fe	^{14}N(n,p), ^{13}C(a,n), ^{138}Ba(n,γ)	

Table 4.3 *The reactions used for the uncertainty estimation for isotopic and elemental ratios relevant to grains and observed values in Chapter 3. All reactions found to be key reactions in Table 4.2 were investigated for all ratios, and reactions that produce abundance changes of the order of a few % or more are listed here. The important stable reactions are provided in order of largest contribution to overall uncertainty (upper limit). For branching points, all reactions are varied simultaneously in the simulation, hence the table lists the reactions most likely to contribute.*

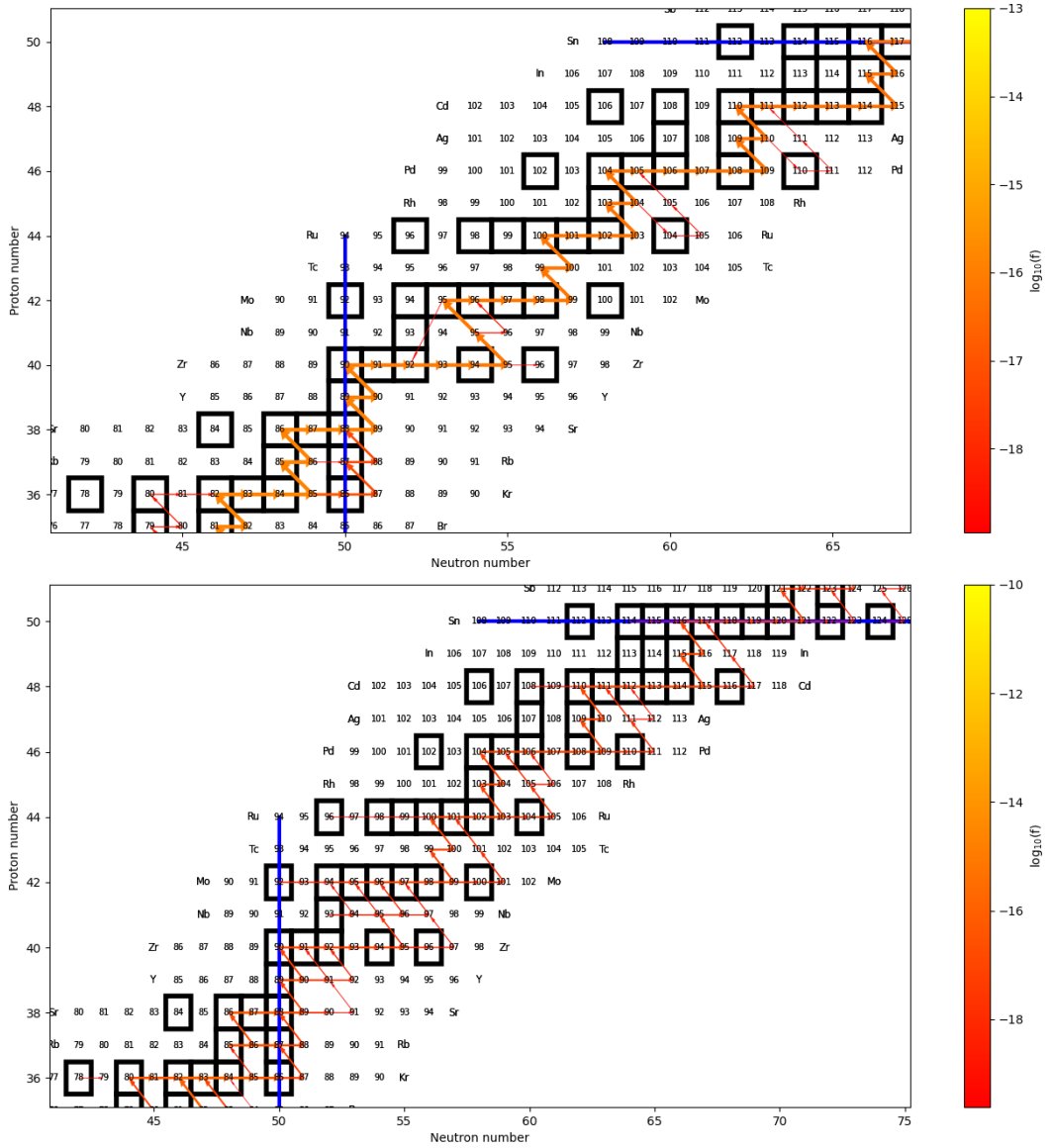

Figure 4.5 *Flux plot of the reaction flow in the Kr to Sn mass region. The strength of the reaction path indicated by the colour panel showing $log_{10}(f)$ values. The upper panel shows the 16^{th} inter-pulse period at the peak neutron density with* PPN*, while the lower panel shows the 6^{th} TP at peak neutron density.*

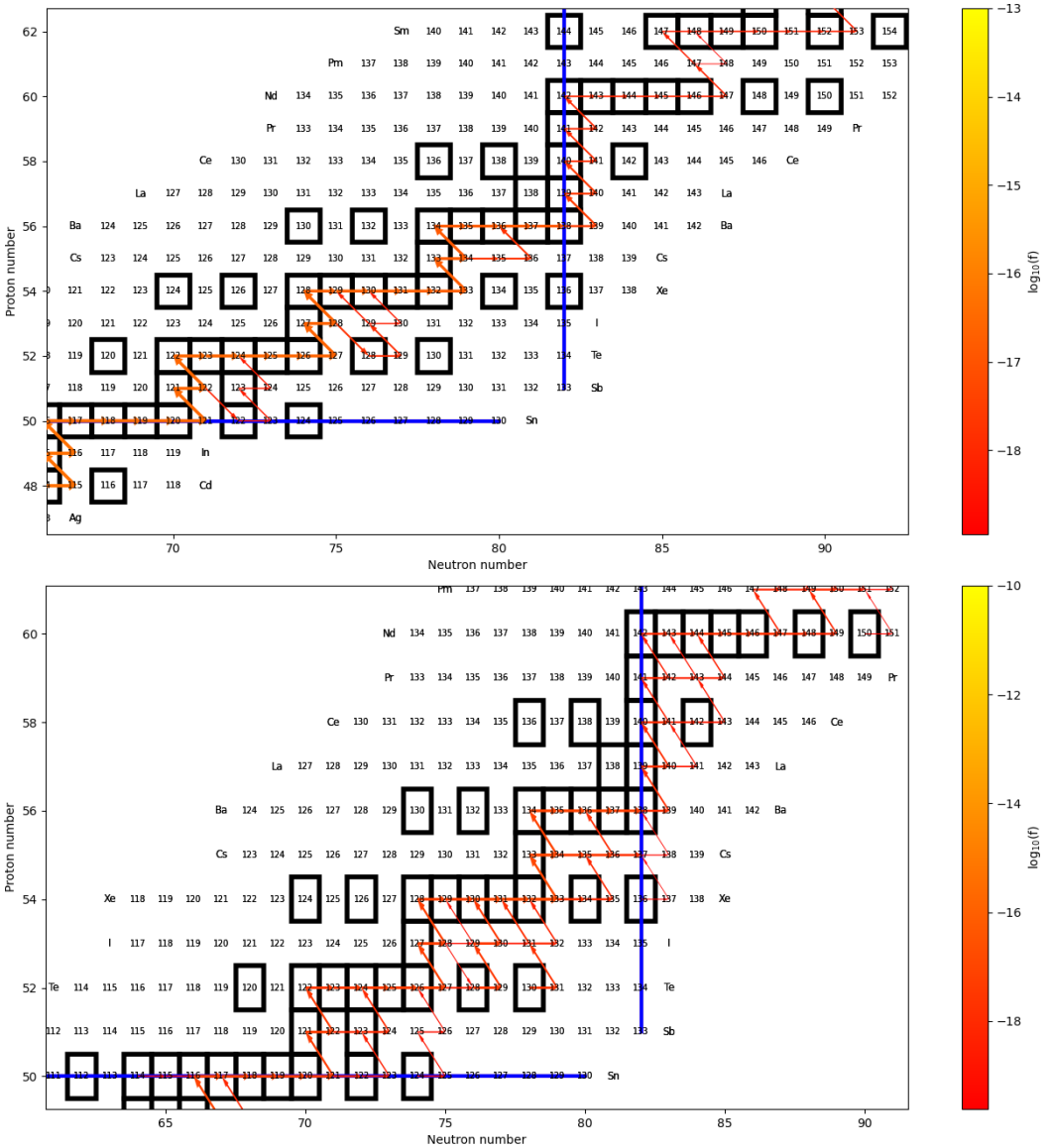

Figure 4.6 *Same as Figure 4.5, but for the Sn to beyond Nd mass region.*

- ^{84}Sr/^{86}Sr: For this isotopic ratio, the PPN Monte Carlo study revealed just one reaction with a significant correlation, namely ^{84}Sr(n,γ). However, the MPPNP study varying this reaction resulted in very little change of the ^{84}Sr/^{86}Sr ratio. This can be explained by the fact that ^{84}Sr is a *p*-only nucleus which gets destroyed in a single zone simulation. For the MPPNP simulation, this isotope will experience much less depletion due to mixing processes. The other obvious reaction which may affect this ratio is ^{86}Sr(n,γ), which indeed was found to contribute significantly to the uncertainty of this isotopic ratios.

- ^{88}Sr/^{86}Sr, ^{90}Zr/^{94}Zr, ^{138}Ba/^{136}Ba, and Y/Fe: For all these ratios, the numerator isotope (Y has just one stable isotope, ^{89}Y) has a magic neutron number, which results in comparably small neutron capture cross sections, and hence these isotopes represent bottlenecks in the *s*-process flow, which are more realistically simulated in MPPNP. For ^{88}Sr/^{86}Sr, reactions which globally affect *s*-process abundances (^{56}Fe(n,γ) and ^{13}C(alpha,n)) were also found to be important. For ^{90}Zr/^{94}Zr the ^{14}N(n,p) identified initially as a key rate was found to have a negligible impact on the abundances. For ^{138}Ba/^{136}Ba, the bottleneck ^{138}Ba(n,γ) and neutron source ^{13}C(α,n) reaction was found to be important. In addition, for Y/Fe, it turned out that ^{56}Fe has only a minor impact, while ^{64}Ni(n,γ) and ^{88}Sr(n,γ) were added to the uncertainty calculation, both of these reactions have small cross sections.

- ^{92}Mo/^{96}Mo, and ^{94}Mo/^{96}Mo: Similar to ^{84}Sr/^{86}Sr, these ratios include *p*-only isotopes (^{92}Mo and ^{94}Mo) and therefore differences between PPN and MPPNP are expected. In the MPPNP simulation, neutron capture rates on the *p*-only isotopes had only a small impact (as expected), and instead ^{96}Mo(n,γ) was found to be important. In addition some neutron poison / bottleneck reactions were found to play a role (^{64}Ni(n,γ) for ^{92}Mo/^{96}Mo and ^{14}N(n,p) for ^{94}Mo/^{96}Mo).

The reactions in Table 4.3 listed under "Important ^{13}C-pocket Reactions" were varied one by one using MPPNP. Due to the large number of branching points, varying each one separately was not feasible, and hence the branching points were varied simultaneously. This means that a particular key reaction cannot be assigned to a particular uncertainty, but the branching point reactions that are responsible for an abundance uncertainty can be guessed from looking at the

Abundance	TP 16 [$M_\odot$]	TP 18 [$M_\odot$]	TP 20 [$M_\odot$]	TP 22 [$M_\odot$]	TP 24 [$M_\odot$]	Yield [$M_\odot$]
$^{84}Sr/^{86}Sr$	$0.0345^{+0.0050}_{-0.0032}$	$0.0310^{+0.0056}_{-0.0035}$	$0.0277^{+0.0059}_{-0.0036}$	$0.0241^{+0.0062}_{-0.0036}$	$0.0188^{+0.0063}_{-0.0032}$	$0.0227^{+0.0063}_{-0.0035}$
$^{87}Sr/^{86}Sr$	$0.727^{+0.042}_{-0.037}$	$0.719^{+0.049}_{-0.042}$	$0.711^{+0.055}_{-0.047}$	$0.697^{+0.061}_{-0.051}$	$0.672^{+0.067}_{-0.055}$	$0.688^{+0.062}_{-0.091}$
$^{88}Sr/^{86}Sr$	$10.22^{+1.37}_{-0.98}$	$10.55^{+1.75}_{-1.20}$	$10.80^{+2.14}_{-1.41}$	$10.84^{+2.57}_{-1.60}$	$10.35^{+3.14}_{-1.77}$	$10.54^{+2.61}_{-1.58}$
$^{90}Zr/^{94}Zr$	$2.18^{+0.20}_{-0.20}$	$2.09^{+0.22}_{-0.22}$	$2.01^{+0.23}_{-0.22}$	$1.95^{+0.23}_{-0.23}$	$1.88^{+0.25}_{-0.23}$	$1.94^{+0.23}_{-0.23}$
$^{91}Zr/^{94}Zr$	$0.549^{+0.058}_{-0.056}$	$0.540^{+0.065}_{-0.061}$	$0.534^{+0.069}_{-0.065}$	$0.530^{+0.074}_{-0.069}$	$0.525^{+0.079}_{-0.073}$	$0.529^{+0.075}_{-0.070}$
$^{92}Zr/^{94}Zr$	$0.86^{+0.11}_{-0.09}$	$0.85^{+0.12}_{-0.10}$	$0.85^{+0.13}_{-0.11}$	$0.85^{+0.14}_{-0.12}$	$0.85^{+0.15}_{-0.13}$	$0.85^{+0.14}_{-0.12}$
$^{96}Zr/^{94}Zr$	$0.104^{+0.077}_{-0.028}$	$0.105^{+0.098}_{-0.036}$	$0.110^{+0.120}_{-0.042}$	$0.118^{+0.140}_{-0.061}$	$0.131^{+0.181}_{-0.071}$	$0.124^{+0.151}_{-0.061}$
$^{92}Mo/^{96}Mo$	$0.327^{+0.050}_{-0.032}$	$0.270^{+0.050}_{-0.031}$	$0.227^{+0.049}_{-0.028}$	$0.191^{+0.047}_{-0.026}$	$0.154^{+0.042}_{-0.023}$	$0.185^{+0.046}_{-0.026}$
$^{94}Mo/^{96}Mo$	$0.214^{+0.030}_{-0.019}$	$0.178^{+0.030}_{-0.072}$	$0.150^{+0.030}_{-0.017}$	$0.127^{+0.028}_{-0.015}$	$0.103^{+0.026}_{-0.013}$	$0.123^{+0.028}_{-0.015}$
$^{95}Mo/^{96}Mo$	$0.719^{+0.063}_{-0.067}$	$0.701^{+0.069}_{-0.071}$	$0.689^{+0.072}_{-0.074}$	$0.681^{+0.075}_{-0.076}$	$0.676^{+0.077}_{-0.078}$	$0.683^{+0.075}_{-0.076}$
$^{97}Mo/^{96}Mo$	$0.423^{+0.048}_{-0.042}$	$0.405^{+0.053}_{-0.045}$	$0.392^{+0.057}_{-0.046}$	$0.381^{+0.061}_{-0.048}$	$0.370^{+0.067}_{-0.050}$	$0.379^{+0.062}_{-0.048}$
$^{98}Mo/^{96}Mo$	$1.26^{+0.18}_{-0.15}$	$1.23^{+0.20}_{-0.16}$	$1.20^{+0.22}_{-0.17}$	$1.17^{+0.23}_{-0.18}$	$1.139^{+0.25}_{-0.18}$	$1.16^{+0.22}_{-0.19}$
$^{100}Mo/^{96}Mo$	$0.274^{+0.091}_{-0.042}$	$0.243^{+0.11}_{-0.05}$	$0.221^{+0.12}_{-0.05}$	$0.203^{+0.13}_{-0.06}$	$0.187^{+0.14}_{-0.06}$	$0.202^{+0.13}_{-0.06}$
$^{134}Ba/^{136}Ba$	$0.312^{+0.065}_{-0.052}$	$0.311^{+0.069}_{-0.056}$	$0.311^{+0.072}_{-0.060}$	$0.311^{+0.073}_{-0.062}$	$0.310^{+0.076}_{-0.065}$	$0.311^{+0.073}_{-0.063}$
$^{135}Ba/^{136}Ba$	$0.296^{+0.031}_{-0.027}$	$0.259^{+0.025}_{-0.025}$	$0.233^{+0.021}_{-0.023}$	$0.213^{+0.019}_{-0.023}$	$0.191^{+0.016}_{-0.023}$	$0.210^{+0.019}_{-0.023}$
$^{137}Ba/^{136}Ba$	$1.005^{+0.163}_{-0.079}$	$0.989^{+0.182}_{-0.088}$	$0.984^{+0.202}_{-0.104}$	$0.985^{+0.221}_{-0.121}$	$0.991^{+0.251}_{-0.139}$	$0.991^{+0.230}_{-0.122}$
$^{138}Ba/^{136}Ba$	$8.98^{+0.99}_{-0.81}$	$9.06^{+1.07}_{-0.86}$	$9.16^{+1.14}_{-0.90}$	$9.23^{+1.19}_{-0.94}$	$9.37^{+1.24}_{-0.97}$	$9.28^{+1.20}_{-0.94}$
Y/Fe	$(1.738^{+0.104}_{-0.066}) \times 10{-}5$	$(2.024^{+0.141}_{-0.090}) \times 10{-}5$	$(2.341^{+0.194}_{-0.117}) \times 10{-}5$	$(2.71^{+0.26}_{-0.15}) \times 10{-}5$	$(3.31^{+0.37}_{-0.21}) \times 10{-}5$	$(2.80^{+0.28}_{-0.16}) \times 10{-}5$
Zr/Fe	$(4.24^{+0.15}_{-0.16}) \times 10{-}5$	$(4.93^{+0.21}_{-0.20}) \times 10{-}5$	$(5.68^{+0.26}_{-0.25}) \times 10{-}5$	$(6.56^{+0.33}_{-0.30}) \times 10{-}5$	$(7.88^{+0.42}_{-0.40}) \times 10{-}5$	$(6.72^{+0.34}_{-0.31}) \times 10{-}5$
La/Fe	$(3.96^{+1.04}_{-0.81}) \times 10{-}6$	$(4.84^{+1.35}_{-1.02}) \times 10{-}6$	$(5.77^{+1.67}_{-1.24}) \times 10{-}6$	$(6.77^{+2.04}_{-1.49}) \times 10{-}6$	$(8.28^{+2.57}_{-1.85}) \times 10{-}6$	$(6.92^{+2.09}_{-1.52}) \times 10{-}6$
Ce/Fe	$(1.02^{+0.29}_{-0.22}) \times 10{-}5$	$(1.24^{+0.37}_{-0.27}) \times 10{-}5$	$(1.46^{+0.46}_{-0.32}) \times 10{-}5$	$(1.70^{+0.55}_{-0.38}) \times 10{-}5$	$(2.05^{+0.68}_{-0.46}) \times 10{-}5$	$(1.73^{+0.56}_{-0.38}) \times 10{-}5$
Nd/Fe	$(6.23^{+1.73}_{-1.22}) \times 10{-}6$	$(7.38^{+2.22}_{-1.52}) \times 10{-}6$	$(8.55^{+2.74}_{-1.82}) \times 10{-}6$	$(9.78^{+3.30}_{-2.13}) \times 10{-}6$	$(1.16^{+0.41}_{-0.26}) \times 10{-}5$	$(9.96^{+3.36}_{-2.16}) \times 10{-}6$

Table 4.4 *The total uncertainty (the ^{13}C-pocket test results plus the branching point test results) for both isotopic ratios and elemental ratios observed from grains and in stellar spectra from AGB stars. Provided are alternate carbon enrichment surface data points from the surface plots in Chapter 3 as well as the net yield with an uncertainty calculated from reaction rate uncertainties. The uncertainty provided is for 2σ of reaction rate uncertainty value.*

s-process reaction flow. The branching point listed in Table 4.3 represent the reactions most likely to contribute to the uncertainty, either because opening of a branching point adds an additional production channel, or because it bypasses production of a particular isotope. The change in the resultant surface abundances after the 16^{th}, 18^{th}, 20^{th}, 22^{nd}, and 24^{th} TP as well as the change in the yield was analysed for each MPPNP run. The total uncertainty for the isotopic and elemental ratios was then determined as the square root of the individual changes added in quadrature. The resultant ratios and their total uncertainties are shown in Table 4.4. Tables B.1-B.3 in Appendix B shows contributions to the uncertainty for selected reactions. Tables B.4 and B.5 show uncertainties from reactions listed in the column "Important ^{13}C pocket Reactions" in Table 4.3, and from the MPPNP run varying all branching points simultaneously, respectively.

The large uncertainties of neutron capture cross sections on branching point nuclei impact all abundance ratio uncertainties in this work, with the exception of ^{90}Zr/^{94}Zr, ^{91}Zr/^{94}Zr, ^{92}Zr/^{94}Zr, ^{135}Ba/^{136}Ba, ^{138}Ba/^{136}Ba, Zr/Fe, La/Fe, Ce/Fe and Nd/Fe. In the next few paragraphs, the individual cases will be discussed in more detail:

Strontium ratios: Both strontium ratios ^{84}Sr/^{86}Sr and ^{88}Sr/^{86}Sr have a total uncertainty above 20%, dominated by uncertainties due to branching points. From the flux plot the relevant branching points are ^{85}Kr and ^{86}Rb, which both can bypass ^{86}Sr production. Since these branching point rates were varied in the same direction for the MPPNP run, the uncertainty here represents the worst case scenario. ^{87}Sr/^{86}Sr are well constrained below 10%, as branching points have only a small impact on the overall uncertainty.

Zirconium ratios: All Zr ratios except for ^{96}Zr/^{94}Zr are well constrained with total uncertainties from 10-16%. ^{96}Zr/^{94}Zr is strongly affected by the uncertainty in the ^{95}Zr(n,γ) reaction cross section, therefore resulting in uncertainties of +120% and -49%. The ^{92}Zr/^{94}Zr uncertainty could be further reduced by using an updated ^{14}N(n,p) cross section with decreased uncertainty.

Molybdenum ratios: Uncertainties for Mo isotopic ratios range from 10% to 20%, with the exception of ^{100}Mo/^{96}Mo, which has a high uncertainty of +64% and -30%, due to the uncertainty in the cross section on unstable ^{99}Mo(n,γ). For the other ratios, the branching point uncertainty is dominated by the ^{95}Zr(n,γ) reaction, which leads to bypassing ^{95}Mo, and ^{96}Mo production. Also some impact from branching at ^{94}Nb and ^{95}Nb can be expected. The impact of an increased

^{95}Mo(n,γ) value on the stellar models of this work was discussed already in Chapter 3 (see Figure 3.21).

Barium Ratios: ^{135}Ba/^{136}Ba and ^{138}Ba/^{136}Ba ratios have a low uncertainty of around 10%, while uncertainties for ^{134}Ba/^{136}Ba and ^{137}Ba/^{136}Ba exceed 20%. For both latter ratios, the branching point run contributed most to the overall uncertainty. There are a number of branching points around Cs and Xe which will affect Ba isotopic ratios. For example, branching points at ^{133}Xe and ^{134}Cs lead to bypassing the ^{134}Ba production. There is also a branching at ^{136}Cs which would impact on the ^{137}Ba/^{136}Ba ratio. For a proper analysis however, the branching points in question would need to be varied separately in MPPNP. The case of Ba isotopic ratios is further complicated by the fact that the neutron capture cross sections on stable Ba isotopes have been re-evaluated to an update in the cross section used as a reference reaction (Reifarth et al. [180]). The new evaluation recommends rates that are 10%, 8%, 15% and 45% higher for ^{134}Ba(n,γ), ^{135}Ba(n,γ), ^{136}Ba(n,γ), ^{137}Ba(n,γ), respectively. The impact of these updated values on the stellar models of this work was discussed already in Chapter 3 (see Figure 3.9). However, this means that Ba isotopic ratios and their uncertainties using the default rates should be treated with caution, and updated rates should be included in the stellar models in the future. The impact of an increased ^{137}Ba(n,γ) value on the stellar models of this work was discussed already in Chapter 3 (see Figure 3.9).

Y/Fe and Zr/Fe have small uncertainties around 10%. For Y/Fe, the higher contribution to the uncertainty comes from branching points for which ^{89}Sr is the most likely candidate, as this reaction leads to bypassing Y production completely. ^{85}Kr(n,γ) has an individual test because it was one of the five largest Pearson correlation coefficients for ^{88}Sr/^{86}Sr. It was tested for Y/Fe and was found to contribute 50% of the lower uncertainty and 15% of the upper uncertainty. Uncertainties in Zr/Fe are dominated by stable reactions. For La/Fe, Ce/Fe and Nd/Fe uncertainties are around 30%, mainly due to the uncertainty of the ^{14}N(n,p) cross section adopted. As in previous cases, this will be improved when implementing newer and more accurate experimental data.

Now the uncertainties have been presented, it is useful to see how they affect the comparisons with observations i.e. pre-solar grains measurements and barium star spectra.

For Sr ratios, the model ^{84}Sr/^{86}Sr were higher than the observed values, however

this ratio has 17% uncertainty so within nuclear physics uncertainties, the agreement is good. ^{87}Sr/^{86}Sr and ^{88}Sr/^{86}Sr match with some of the observables, but the different models cannot reproduce the spread in observed values. The range of observed values can possibly be explained by contributions from stars with different rotational mixing as shown in the bottom panel of Figure 3.11.

For Zr isotopic ratios (see e.g. Figure 3.13), for all cases the nuclear physics uncertainties can account for any differences with observations: the agreement for ^{90,91,92}Zr/^{94}Zr is already fair, there is a disagreement for ^{96}Zr/^{94}Zr, but this ratio has a high uncertainty due to the unknown ^{95}Zr(n,γ) cross section (in addition ^{22}Ne(α,n) also affects this ratio, see Figure 3.16). The spread of values observed cannot be reproduced by models, hence this needs to be addressed by studying the effect of mixing.

There is already good agreement for most Mo isotopic ratios with observation, except for ^{95}Mo and ^{100}Mo. As mentioned previously, agreement can be improved when using an updated ^{95}Mo(n,γ) rate. ^{100}Mo/^{96}Mo ratios are at the moment predicted as too high, but agree within uncertainties given the high uncertainty of this ratio due to the unknown ^{99}Mo(n,γ) rate.

For Ba ratios, ^{134}Ba/^{136}Ba and ^{135}Ba/^{136}Ba are well reproduced in stellar models, although for ^{134}Ba/^{136}Ba the spread in observed values cannot be explained by the standard models, and likely other mixing processes need to be invoked. ^{137}Ba/^{136}Ba is predicted as higher compared to observations, while for ^{138}Ba/^{136}Ba the spread of observed values can be reproduced by models, however they tend to predict higher values. Since there are now updated cross sections on Ba isotopes, a new calculation should be performed in the future. In addition the ^{22}Ne(α,n) reaction is expected to have an impact on some ratios (see Figure 3.8).

Concerning the elemental ratios, there is good agreement already for Ce/Y, while for Ce/Fe only the highest values are reached. Although uncertainties are high for Ce/Fe and as a consequence Ce/Y, these cannot move the tracks to the mean of the observed values.

Summarising, many isotopic and elemental abundance ratios can be predicted within 10% uncertainty from the nuclear physics input. Higher uncertainties are usually obtained if abundances are affected by branching point reactions, where no experimental cross section data are available. However, in several cases updating the nuclear network using new experimental data would already improve

the predictive power of the MPPNP calculation and reduce some uncertainties. The single zone Monte Carlo approach allowed to identify the key nuclear reactions which most contribute to abundance uncertainties. However, the MPPNP runs revealed that some reactions were not as important as indicated by the Monte Carlo study, while other important reactions were missed. This concerns particularly reactions with a global impact on abundances (e.g. neutron source, neutron poison and reactions with very small cross sections). Hence, for an accurate determination of abundance uncertainties, a Monte Carlo MPPNP study would be required. Unfortunately, this is at present not possible due to the computational demand and time requirements.

Chapter 5

Conclusion

This thesis presents extensive post-processing calculations using the MPPNP code to update models of asymptotic giant branch (AGB) stars, and estimate uncertainties of specific isotopic and elemental abundance ratios coming from uncertainties in nuclear reaction rates. Chapter 3 presents results from post-processing calculations of AGB stellar models which were updated from models published in RI18. The update consisted of a different description of convective boundary mixing (CBM) (Battino et al. [11]) resulting in a three times larger ^{13}C-pocket compared to the RI18 models, hence increasing slow neutron-capture process (s-process) production which yielded an improved agreement to observations. In addition, models were also calculated for a metallicity Z = 0.03, since they have a large contribution to dust production and hence pre-solar grains can be significant (Lewis et al. [123], Lugaro et al. [138]). Surface abundances and yields were also calculated for two additional models (labelled '-hCBM') with metallicities Z = 0.02 and 0.03, these models have increased CBM under the convective envelope during third dredge ups. The resultant surface abundances were compared to a large set of observables, including surface abundances inferred from spectroscopy from carbon-stars and barium-stars, and isotopic ratios measured in meteoritic grains. It was found that models with an increased CBM (-hCBM) show a better general agreement to observations. This underlines the fact that a realistic description of CBM is indispensable for predicting s-process abundances, and more research is needed. Within all uncertainties (stellar modelling, nuclear physics, and observations) the models agree with most of observational data. The most difficult observables to reproduce are the full ranges of some isotopic ratios, precisely ^{84}Sr/^{86}Sr, ^{137}Ba/^{136}Ba,

^{96}Zr/^{94}Zr, ^{95,100}Mo/^{96}Mo. The Z = 0.03 model provided a better agreement with grains, specifically for ^{138}Ba/^{136}Ba ratios, which confirms results by Lugaro et al. [138]. A better agreement can also be found for lower metallicity models when introducing rotational mixing: the role of rotation-induced mixing was explored by adopting a simple parametric approach. Results indicate that this might be able to explain the range of observed values in pre-solar grains. It should be noted, however, that the effect of stellar rotation as an efficient extra mixing source in AGB stars is still a matter of debate (see Deheuvels et al. [55], Herwig [89], Straniero et al. [193]). Chapter 3 also presents the ejected yields from the models.

Chapter 4 was dedicated to estimate the uncertainties of specific isotopic and elemental ratios due to uncertainties of nuclear reaction rates. This was achieved by running one zone nucleosynthesis calculations thousands of times, while randomly varying nuclear reaction rates within their uncertainties. The most important nuclear reaction rates impacting the abundances considered were determined using Pearson correlation coefficients, and the total uncertainties were then determined in MPPNP runs, varying these reactions one at a time. As this approach is only valid for the *s*-process in the ^{13}C-pocket, where no mixing occurs, uncertainties of branching point reactions which are only important in the thermal pulse were studied separately with MPPNP. A similar Monte Carlo study was already performed by Cescutti et al. [29]. The key reactions identified in my work agree well with Cescutti et al.'s key reactions, with a few differences that could possibly come from using a stellar model with different metallicity and a different nuclear reaction network. The subsequent runs with MPPNP revealed that some single zone key rates were not important, while other rates had to be added. This concerned in particular reactions that globally affect *s*-process abundances, for example neutron source, neutron poison and reactions with very small neutron captures. In general, uncertainties in isotopic and elemental ratios were found to be around 10%, while in a few cases they were significantly higher due to the high impact of branching point reactions exhibiting high nuclei reaction rate uncertainties. While in some cases, reaction rate uncertainties could be responsible for disagreements of model predictions to observations (for example ^{84}Sr/^{86}Sr), in a few cases the results indicate that only improved stellar models can achieve a better match to observations (in the case of ^{88}Sr/^{86}Sr). The work was performed for one particular model (M = 3 $M_{\odot}$, metallicity, Z = 0.02) in the future the same studies should be performed for the remaining stellar models. Additionally, branching point reactions should be varied one by one to assess

their individual importance (this however, will take up significant time). The nuclear reaction network used by the NuGrid collaboration and in this work is outdated for several reactions. Any future studies should implement the newest experimental data. In addition, this study highlighted a few reactions that should be prioritised in future experimental studies, such as the ^{96}Mo(n,γ) and the ^{94}Zr(n,γ) reactions.

Appendix A

Finding Key Reactions using Monte Carlo Approaches

A.1 Nuclear Reaction Network and Uncertainties

Tables A.1, A.2 and A.3 provide the full list of reactions and their corresponding multiplication factors used for the Monte Carlo reaction rate tests conducted in Chapter 4.

Reaction	Factor	Reaction	Factor	Reaction	Factor
^{13}C(α,n)	1.217	^{22}Ne(α,n)	3.200	^{14}N(n,p)	1.200
^{1}H(n,γ)	1.079	^{2}H(n,γ)	1.067	^{12}C(n,γ)	1.000
^{13}C(n,γ)	1.190	^{14}C(n,γ)	1.067	^{14}N(n,γ)	2.000
^{15}N(n,γ)	1.103	^{16}O(n,γ)	1.105	^{17}O(n,γ)	1.100
^{18}O(n,γ)	1.090	^{19}F(n,γ)	1.031	^{20}Ne(n,γ)	1.133
^{21}Ne(n,γ)	1.097	^{22}Ne(n,γ)	1.051	^{22}Ne(α,γ)	4.000
^{23}Na(n,γ)	1.067	^{24}Mg(n,γ)	1.053	^{25}Mg(n,γ)	1.146
^{26}Mg(n,γ)	1.071	^{26}Al(n,γ)	2.000	^{27}Al(n,γ)	1.080
^{28}Si(n,γ)	1.092	^{29}Si(n,γ)	1.078	^{30}Si(n,γ)	1.181
^{31}P(n,γ)	1.052	^{32}S(n,γ)	1.049	^{33}S(n,γ)	1.203
^{34}S(n,γ)	1.044	^{36}S(n,γ)	1.082	^{35}Cl(n,γ)	1.031
^{36}Cl(n,γ)	2.000	^{37}Cl(n,γ)	1.081	^{36}Ar(n,γ)	2.000
^{38}Ar(n,γ)	2.000	^{39}Ar(n,γ)	2.000	^{40}Ar(n,γ)	1.059
^{39}K(n,γ)	1.034	^{40}K(n,γ)	2.000	^{41}K(n,γ)	1.032
^{40}Ca(n,γ)	1.059	^{41}Ca(n,γ)	2.000	^{42}Ca(n,γ)	1.128
^{43}Ca(n,γ)	1.118	^{44}Ca(n,γ)	1.138	^{45}Ca(n,γ)	2.000
^{46}Ca(n,γ)	1.094	^{48}Ca(n,γ)	1.103	^{45}Sc(n,γ)	1.053
^{46}Ti(n,γ)	1.119	^{47}Ti(n,γ)	1.120	^{48}Ti(n,γ)	1.160
^{49}Ti(n,γ)	1.111	^{49}V(n,γ)	2.000	^{50}V(n,γ)	1.105
^{50}Cr(n,γ)	1.265	^{51}Cr(n,γ)	2.000	^{52}Cr(n,γ)	1.261
^{53}Cr(n,γ)	1.172	^{54}Cr(n,γ)	1.239	^{55}Mn(n,γ)	1.076
^{54}Fe(n,γ)	1.099	^{55}Fe(n,γ)	2.000	^{56}Fe(n,γ)	1.043
^{57}Fe(n,γ)	1.100	^{58}(Fen,γ)	1.052	^{60}Fe(n,γ)	1.274
^{59}Co(n,γ)	1.068	^{60}Co(n,γ)	2.000	^{58}Ni(n,γ)	1.055
^{59}Ni(n,γ)	2.000	^{60}Ni(n,γ)	1.023	^{61}Ni(n,γ)	1.098
^{62}Ni(n,γ)	1.059	^{63}Ni(n,γ)	1.301	^{64}Ni(n,γ)	1.088
^{63}Cu(n,γ)	1.039	^{65}Cu(n,γ)	1.044	^{64}Zn(n,γ)	1.085
^{65}Zn(n,γ)	2.000	^{66}Zn,γ)	1.086	^{67}Zn(n,γ)	1.098
^{68}Zn(n,γ)	1.125	^{70}Zn(n,γ)	1.093	^{69}Ga(n,γ)	1.043
^{71}Ga(n,γ)	1.065	^{70}Ge(n,γ)	1.057	^{71}Ge(n,γ)	2.000
^{72}Ge(n,γ)	2.000	^{73}Ge(n,γ)	2.000	^{74}Ge(n,γ)	1.104
^{76}Ge(n,γ)	1.084	^{75}As(n,γ)	1.052	^{74}Se(n,γ)	2.000
^{76}Se(n,γ)	1.049	^{77}Se(n,γ)	2.000	^{78}Se(n,γ)	1.167
^{79}Se(n,γ)	2.000	^{80}Se(n,γ)	1.071	^{82}Se(n,γ)	2.000
^{79}Br(n,γ)	1.096	^{81}Br(n,γ)	1.039	^{78}Kr(n,γ)	1.081
^{79}Kr(n,γ)	2.000	^{80}Kr(n,γ)	1.052	^{81}Kr(n,γ)	2.000
^{82}Kr(n,γ)	1.065	^{83}Kr(n,γ)	1.051	^{84}Kr(n,γ)	1.061
^{85}Kr(n,γ)	2.000	^{86}Kr(n,γ)	1.059	^{85}Rb(n,γ)	1.039
^{86}Rb(n,γ)	2.000	^{87}Rb(n,γ)	1.057	^{84}Sr(n,γ)	2.000
^{86}Sr(n,γ)	1.047	^{87}Sr(n,γ)	1.043	^{88}Sr(n,γ)	1.048
^{89}Sr(n,γ)	2.000	^{89}Y(n,γ)	1.032	^{90}Zr(n,γ)	1.047
^{91}Zr(n,γ)	1.037	^{92}Zr(n,γ)	1.080	^{93}Zr(n,γ)	1.093

Table A.1 *Reactions and their respective factors used in the Monte Carlo tests for the ^{13}C-pocket scenario. Values given are for a 1σ uncertainty.*

Reaction	Factor	Reaction	Factor	Reaction	Factor
^{94}Zr(n,γ)	1.066	^{95}Zr(n,γ)	2.000	^{96}Zr(n,γ)	1.068
^{93}Nb(n,γ)	1.019	^{94}Nb(n,γ)	2.000	^{95}Nb(n,γ)	2.000
^{92}Mo(n,γ)	1.143	^{94}Mo(n,γ)	1.196	^{95}Mo(n,γ)	1.041
^{96}Mo(n,γ)	1.071	^{97}Mo(n,γ)	1.041	^{98}Mo(n,γ)	1.071
^{99}Mo(n,γ)	2.000	^{100}Mo(n,γ)	1.130	^{99}Tc(n,γ)	1.064
^{96}Ru(n,γ)	1.039	^{98}Ru(n,γ)	2.000	^{99}Ru(n,γ)	2.000
^{100}Ru(n,γ)	1.063	^{101}Ru(n,γ)	1.040	^{102}Ru(n,γ)	1.046
^{103}Ru(n,γ)	2.000	^{104}Ru(n,γ)	1.032	^{103}Rh(n,γ)	1.017
^{102}Pd(n,γ)	1.046	^{104}Pd(n,γ)	1.100	^{105}Pd(n,γ)	1.050
^{106}Pd(n,γ)	1.099	^{107}Pd(n,γ)	1.045	^{108}Pd(n,γ)	1.099
^{110}Pd(n,γ)	1.137	^{107}Ag(n,γ)	1.038	^{109}Ag(n,γ)	1.038
^{110}Ag(n,γ)	2.000	^{106}Cd(n,γ)	1.079	^{108}Cd(n,γ)	2.000
^{110}Cd(n,γ)	1.008	^{111}Cd(n,γ)	1.016	^{112}Cd(n,γ)	1.009
^{113}Cd(n,γ)	1.016	^{114}Cd(n,γ)	1.010	^{115}Cd(n,γ)	2.000
^{116}Cd(n,γ)	1.012	^{113}In(n,γ)	1.089	^{114}In(n,γ)	2.000
^{115}In(n,γ)	1.099	^{112}Sn(n,γ)	1.057	^{114}Sn(n,γ)	1.013
^{115}Sn(n,γ)	1.025	^{116}Sn(n,γ)	1.031	^{117}Sn(n,γ)	1.016
^{118}Sn(n,γ)	1.010	^{119}Sn(n,γ)	1.056	^{120}Sn(n,γ)	1.032
^{121}Sn(n,γ)	2.000	^{122}Sn(n,γ)	1.068	^{124}Sn(n,γ)	1.150
^{125}Sn(n,γ)	2.000	^{126}Sn(n,γ)	2.000	^{121}Sb(n,γ)	1.030
^{122}Sb(n,γ)	2.000	^{123}Sb(n,γ)	1.030	^{125}Sb(n,γ)	2.000
^{120}Te(n,γ)	1.050	^{122}Te(n,γ)	1.010	^{123}Te(n,γ)	1.010
^{124}Te(n,γ)	1.013	^{125}Te(n,γ)	1.009	^{126}Te(n,γ)	1.017
^{128}Te(n,γ)	1.029	^{130}Te(n,γ)	1.190	^{127}I(n,γ)	1.047
^{129}I(n,γ)	1.050	^{124}Xe(n,γ)	1.129	^{126}Xe(n,γ)	1.142
^{128}Xe(n,γ)	1.015	^{129}Xe(n,γ)	1.019	^{130}Xe(n,γ)	1.016
^{131}Xe(n,γ)	2.000	^{132}Xe(n,γ)	1.082	^{133}Xe(n,γ)	2.000
^{134}Xe(n,γ)	1.084	^{136}Xe(n,γ)	1.088	^{133}Cs(n,γ)	1.041
^{134}Cs(n,γ)	2.000	^{135}Cs(n,γ)	1.063	^{130}Ba(n,γ)	1.046
^{132}Ba(n,γ)	1.040	^{134}Ba(n,γ)	1.032	^{135}Ba(n,γ)	1.033
^{136}Ba(n,γ)	1.033	^{137}Ba(n,γ)	1.031	^{138}Ba(n,γ)	1.050
^{138}La(n,γ)	2.000	^{139}La(n,γ)	1.096	^{132}Ce(n,γ)	2.000
^{133}Ce(n,γ)	2.000	^{134}Ce(n,γ)	2.000	^{135}Ce(n,γ)	2.000
^{136}Ce(n,γ)	1.070	^{137}Ce(n,γ)	2.000	^{138}Ce(n,γ)	1.028
^{139}Ce(n,γ)	2.000	^{140}Ce(n,γ)	1.036	^{141}Ce(n,γ)	2.000
^{142}Ce(n,γ)	1.036	^{141}Pr(n,γ)	1.013	^{142}Pr(n,γ)	2.000
^{143}Pr(n,γ)	2.000	^{142}Nd(n,γ)	1.020	^{143}Nd(n,γ)	1.012
^{144}Nd(n,γ)	1.018	^{145}Nd(n,γ)	1.012	^{146}Nd(n,γ)	1.011
^{147}Nd(n,γ)	2.000	^{148}Nd(n,γ)	1.014	^{150}Nd(n,γ)	1.063
^{147}Pm(n,γ)	1.141	^{148}Pm(n,γ)	2.000	^{149}Pm(n,γ)	2.000
^{144}Sm(n,γ)	1.065	^{147}Sm(n,γ)	1.010	^{148}Sm(n,γ)	1.008
^{149}Sm(n,γ)	1.009	^{150}Sm(n,γ)	1.009	^{151}Sm(n,γ)	1.022
^{152}Sm(n,γ)	1.008	^{153}Sm(n,γ)	2.000	^{154}Sm(n,γ)	1.044

Table A.2 *Continuation of Table A.1.*

Reaction	Factor	Reaction	Factor	Reaction	Factor
^{151}Eu(n,γ)	1.061	^{152}Eu(n,γ)	2.000	^{153}Eu(n,γ)	1.029
^{154}Eu(n,γ)	1.152	^{155}Eu(n,γ)	1.064	^{152}Gd(n,γ)	1.016
^{153}Gd(n,γ)	2.000	^{154}Gd(n,γ)	1.012	^{155}Gd(n,γ)	1.011
^{156}Gd(n,γ)	1.008	^{157}Gd(n,γ)	1.011	^{158}Gd(n,γ)	1.009
^{160}Gd(n,γ)	1.130	^{159}Tb(n,γ)	1.095	^{160}Tb(n,γ)	2.000
^{156}Dy(n,γ)	1.082	^{158}Dy(n,γ)	2.000	^{160}Dy(n,γ)	1.013
^{161}Dy(n,γ)	1.010	^{162}Dy(n,γ)	1.009	^{163}Dy(n,γ)	1.010
^{164}Dy(n,γ)	1.014	^{163}Ho(n,γ)	1.045	^{165}Ho(n,γ)	1.078
^{162}Er(n,γ)	1.076	^{164}Er(n,γ)	1.047	^{166}Er(n,γ)	1.099
^{167}Er(n,γ)	1.100	^{168}Er(n,γ)	1.130	^{169}Er(n,γ)	2.000
^{170}Er(n,γ)	1.041	^{169}Tm(n,γ)	1.050	^{170}Tm(n,γ)	2.000
^{171}Tm(n,γ)	2.000	^{168}Yb(n,γ)	1.040	^{170}Yb(n,γ)	1.009
^{171}Yb(n,γ)	1.010	^{172}Yb(n,γ)	1.009	^{173}Yb(n,γ)	1.009
^{174}Yb(n,γ)	1.013	^{175}Yb(n,γ)	2.000	^{176}Yb(n,γ)	1.017
^{175}Lu(n,γ)	1.008	^{176}Lu(n,γ)	1.009	^{174}Hf(n,γ)	1.047
^{176}Hf(n,γ)	1.018	^{177}Hf(n,γ)	1.008	^{178}Hf(n,γ)	1.009
^{179}Hf(n,γ)	1.009	^{180}Hf(n,γ)	1.013	^{181}Hf(n,γ)	2.000
^{182}Hf(n,γ)	1.057	^{179}Ta(n,γ)	2.000	^{180}Ta(n,γ)	1.068
^{181}Ta(n,γ)	1.020	^{182}Ta(n,γ)	2.000	^{180}W(n,γ)	1.080
^{182}W(n,γ)	1.029	^{183}W(n,γ)	1.029	^{184}W(n,γ)	1.054
^{185}W(n,γ)	1.108	^{186}W(n,γ)	1.051	^{185}Re(n,γ)	1.040
^{186}Re(n,γ)	2.000	^{187}Re(n,γ)	1.049	^{184}Os(n,γ)	1.066
^{186}Os(n,γ)	1.041	^{187}Os(n,γ)	1.032	^{188}Os(n,γ)	1.048
^{189}Os(n,γ)	1.040	^{190}Os(n,γ)	1.044	^{191}Os(n,γ)	2.000
^{192}Os(n,γ)	1.045	^{191}Ir(n,γ)	1.032	^{192}Ir(n,γ)	2.000
^{193}Ir(n,γ)	1.070	^{190}Pt(n,γ)	1.087	^{192}Pt(n,γ)	2.000
^{193}Pt(n,γ)	2.000	^{194}Pt(n,γ)	2.000	^{195}Pt(n,γ)	2.000
^{196}Pt(n,γ)	1.087	^{198}(n,γ)	1.050	^{197}Au(n,γ)	1.015
^{198}Au(n,γ)	2.000	^{196}Hg(n,γ)	1.039	^{198}Hg(n,γ)	1.087
^{199}Hg(n,γ)	1.061	^{200}Hg(n,γ)	1.104	^{201}Hg(n,γ)	1.053
^{202}Hg(n,γ)	1.030	^{203}Hg(n,γ)	2.000	^{204}Hg(n,γ)	1.095
^{203}Tl(n,γ)	1.065	^{204}Tl(n,γ)	2.000	^{205}Tl(n,γ)	1.074
^{204}Pb(n,γ)	1.038	^{205}Pb(n,γ)	2.000	^{206}Pb(n,γ)	1.021
^{207}Pb(n,γ)	1.051	^{208}Pb(n,γ)	1.083	^{209}Bi(n,γ)	1.117
^{210}Bi(n,γ)	2.000				

Table A.3 *Continuation of Table A.1 and Table A.2.*

Appendix B

Determination of Abundance Uncertainties

Chapter 4 discusses the impact of reaction rate uncertainties. Here the abundance plots for the ratios presented in Chapter 3 are shown for the; plus 1σ and 2σ as well as the minus 1σ and 2σ for the default reaction rate. For simplicity not all key reaction rate are shown, but are presented with a figure of all tracks averaged to the default track. In some cases it is evident why there is an asymmetric uncertainty provided in Table B.4, this originates from the neutron source and poison reactions of the ^{13}C-pocket.

Table B.1 shows the abundance difference for each reaction test carried out in MPPNP, not all were used in the uncertainty calculation and are there to show the range of values other reaction caused in the tests. Shown is the 2σ reaction rate uncertainty values which were used in the calculation of the 16^{th} inter-pulses ^{13}C-pocket uncertainty.

Where Table 4.4 presents the total uncertainty for the given ratios, Table B.4 presents the uncertainty from the ^{13}C-pocket scenario and Table B.5 presents the uncertainty from the branching points test, which the results given in the latter two tables was added together in Table 4.4.

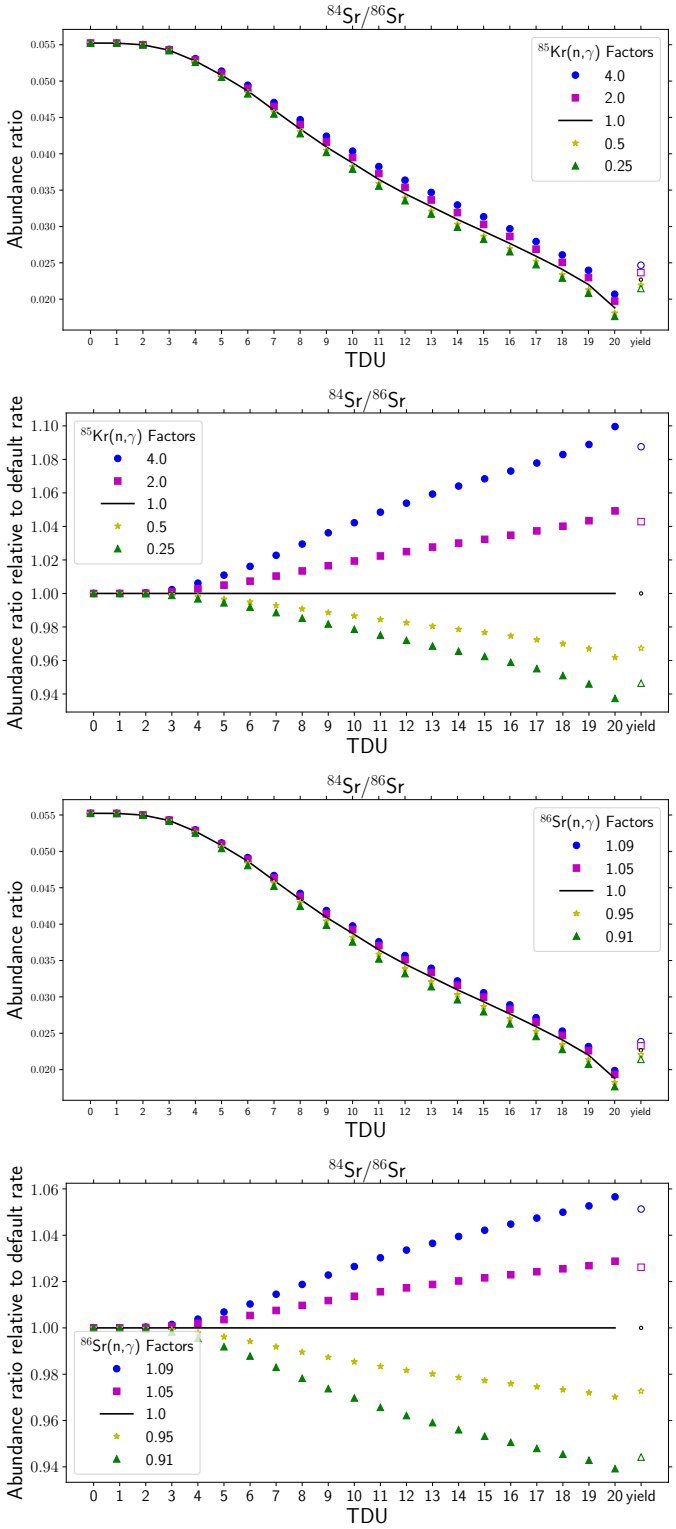

Figure B.1 *The evolution of $^{84}Sr/^{86}Sr$ abundances through the life of a $M=3M_{\odot}$, $Z=0.02$ star, observing the impact of the $^{85}Kr(n,\gamma)$ branching point and $^{86}Sr(n,\gamma)$ key reaction on this ratio.*

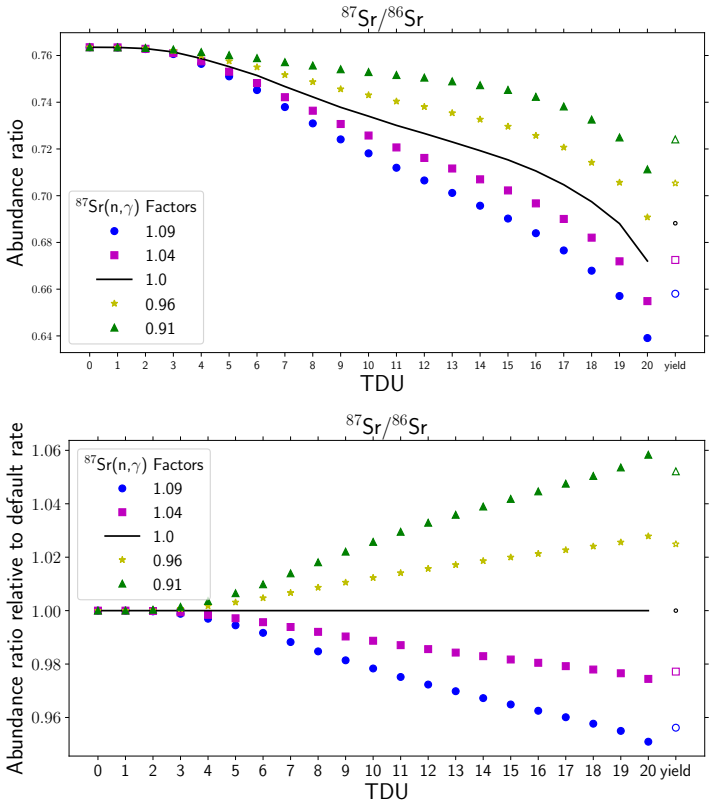

Figure B.2 *The evolution of $^{87}Sr/^{86}Sr$ abundances through the life of a $M=3M_{\odot}$, $Z=0.02$ star, observing the impact of the $^{87}Sr(n,\gamma)$ key reaction on this ratio.*

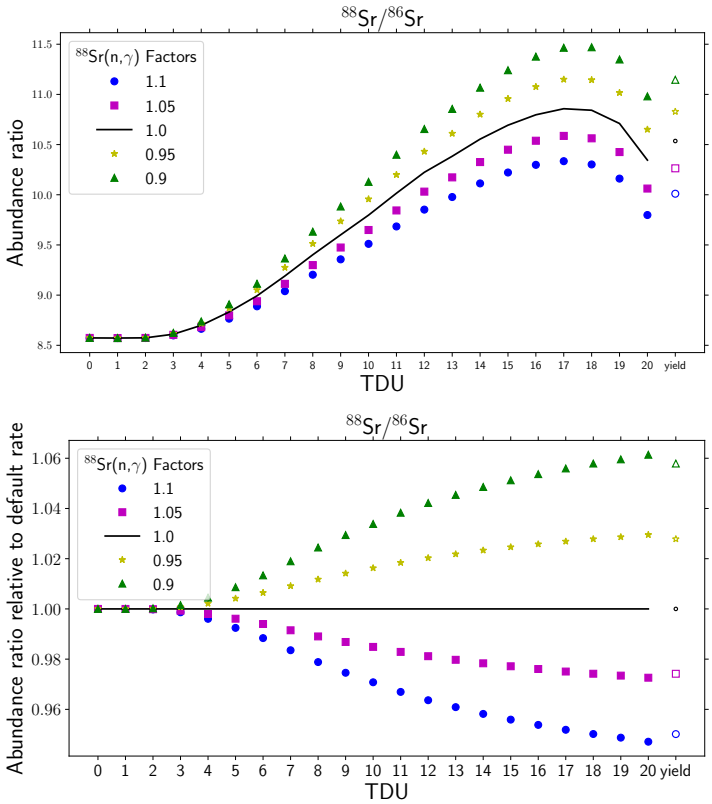

Figure B.3 *The evolution of $^{88}Sr/^{86}Sr$ abundances through the life of a $M=3M_{\odot}$, $Z=0.02$ star, observing the impact of the $^{88}Sr(n,\gamma)$ key reaction on this ratio.*

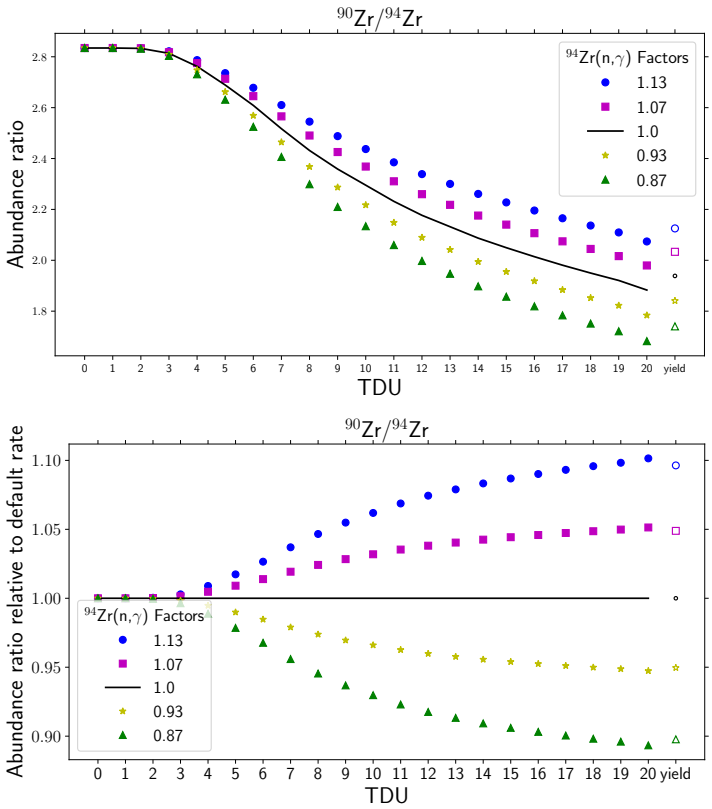

Figure B.4 *The evolution of $^{90}Zr/^{94}Zr$ abundances through the life of a $M=3M_{\odot}$, $Z=0.02$ star, observing the impact of the $^{90}Zr(n,\gamma)$ key reaction on this ratio.*

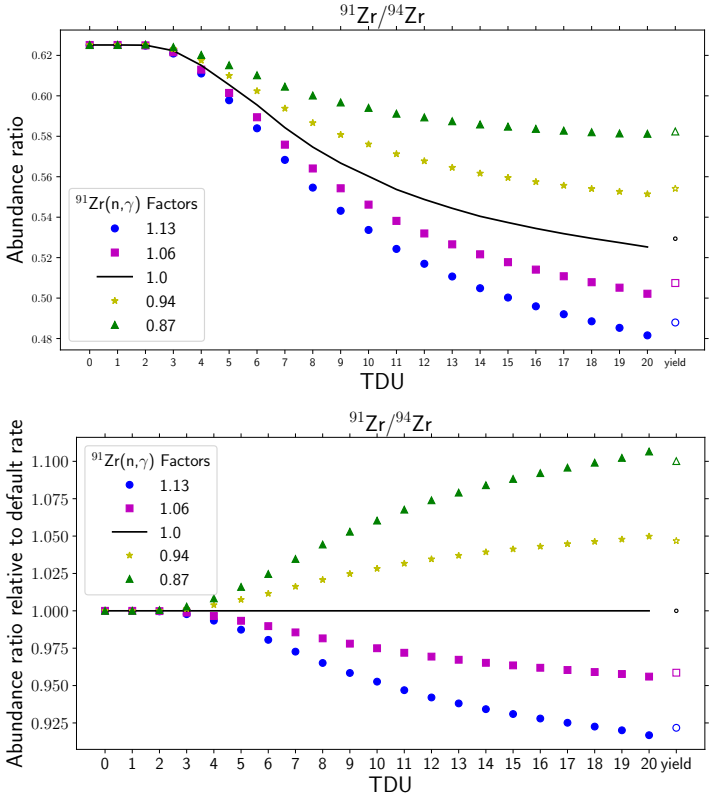

Figure B.5 *The evolution of $^{91}Zr/^{94}Zr$ abundances through the life of a $M=3M_{\odot}$, $Z=0.02$ star, observing the impact of the $^{91}Zr(n,\gamma)$ key reaction on this ratio.*

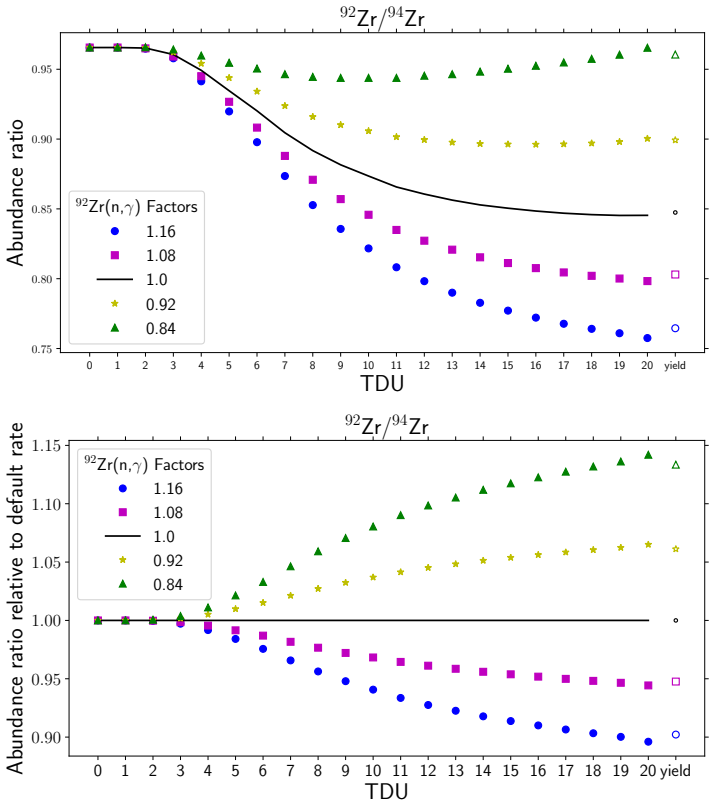

Figure B.6 *The evolution of $^{92}Zr/^{94}Zr$ abundances through the life of a $M=3M_{\odot}$, $Z=0.02$ star, observing the impact of the $^{92}Zr(n,\gamma)$ key reaction on this ratio.*

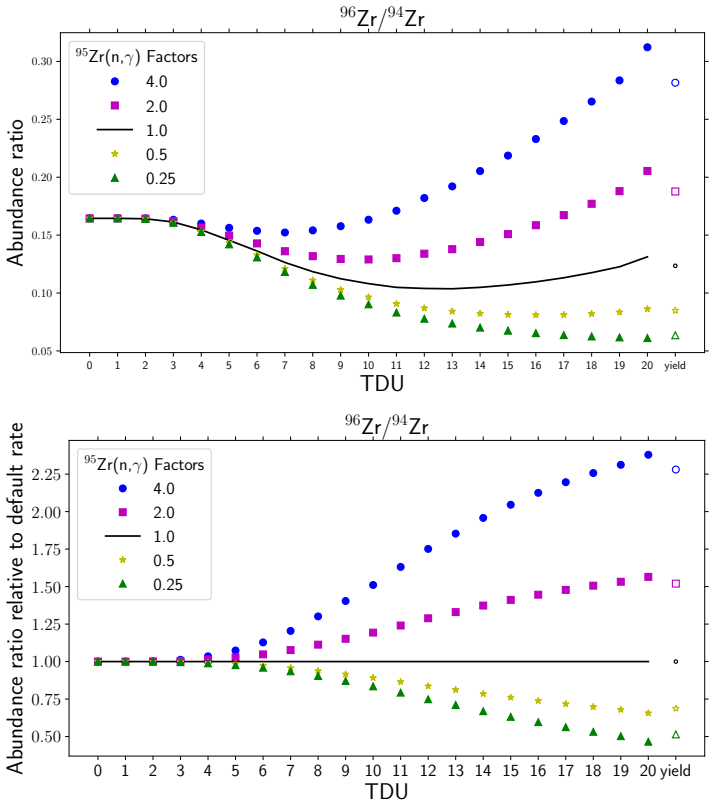

Figure B.7 *The evolution of $^{96}Zr/^{94}Zr$ abundances through the life of a $M=3M_{\odot}$, $Z=0.02$ star, observing the impact of the $^{95}Zr(n,\gamma)$ branching point on this ratio.*

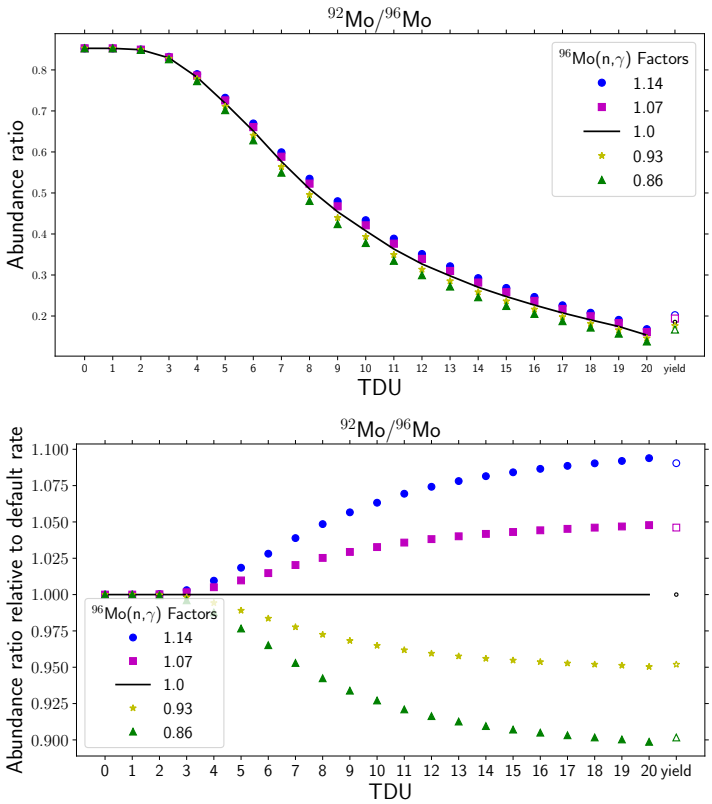

Figure B.8 *The evolution of $^{92}Mo/^{96}Mo$ abundances through the life of a $M=3M_{\odot}$, $Z=0.02$ star, observing the impact of the $^{96}Mo(n,\gamma)$ key reaction on this ratio.*

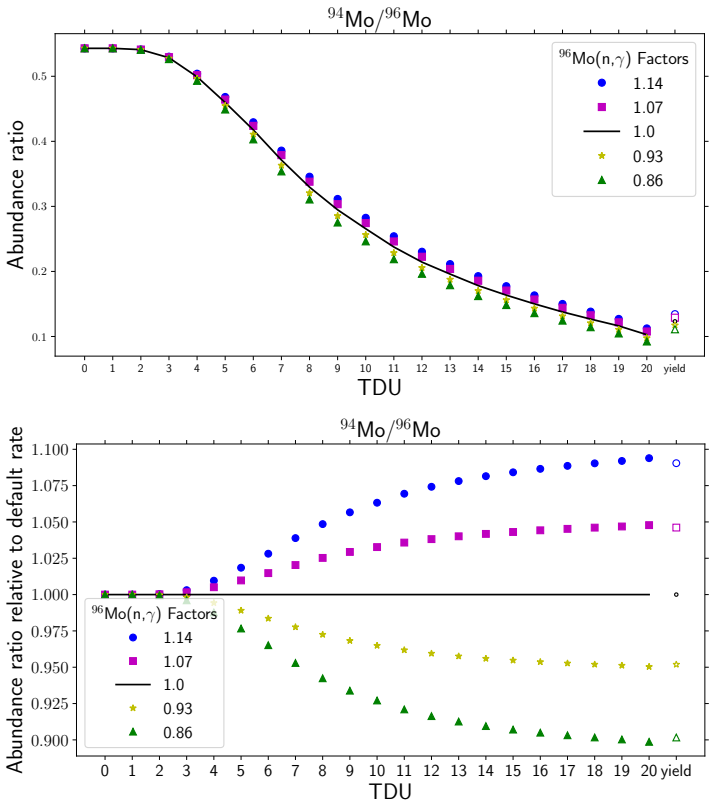

Figure B.9 *The evolution of $^{94}Mo/^{96}Mo$ abundances through the life of a $M=3M_{\odot}$, $Z=0.02$ star, observing the impact of the $^{96}Mo(n,\gamma)$ key reaction on this ratio.*

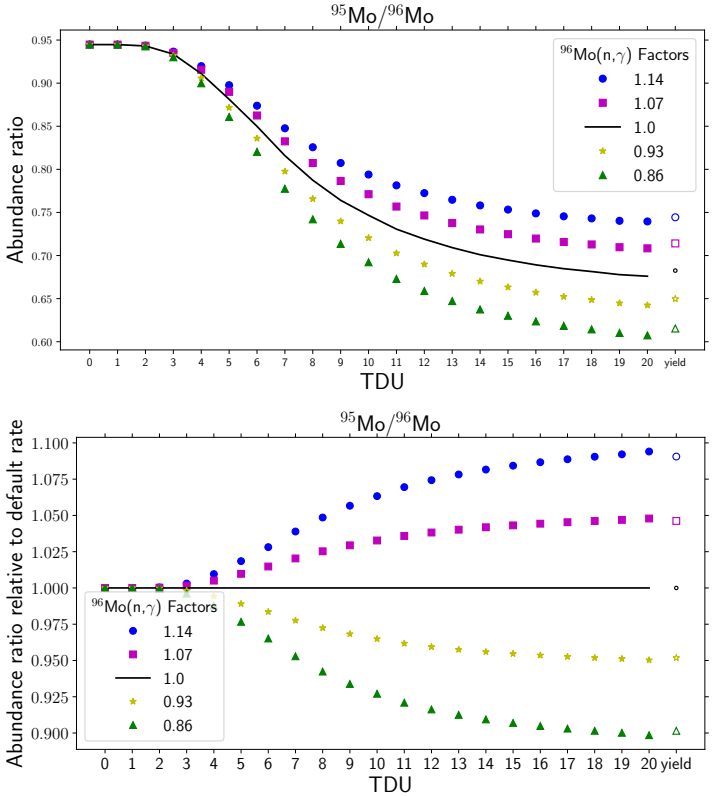

Figure B.10 *The evolution of ^{95}Mo/^{96}Mo abundances through the life of a M=3$M_{\odot}$, Z=0.02 star, observing the impact of the ^{96}Mo(n,γ) key reaction on this ratio.*

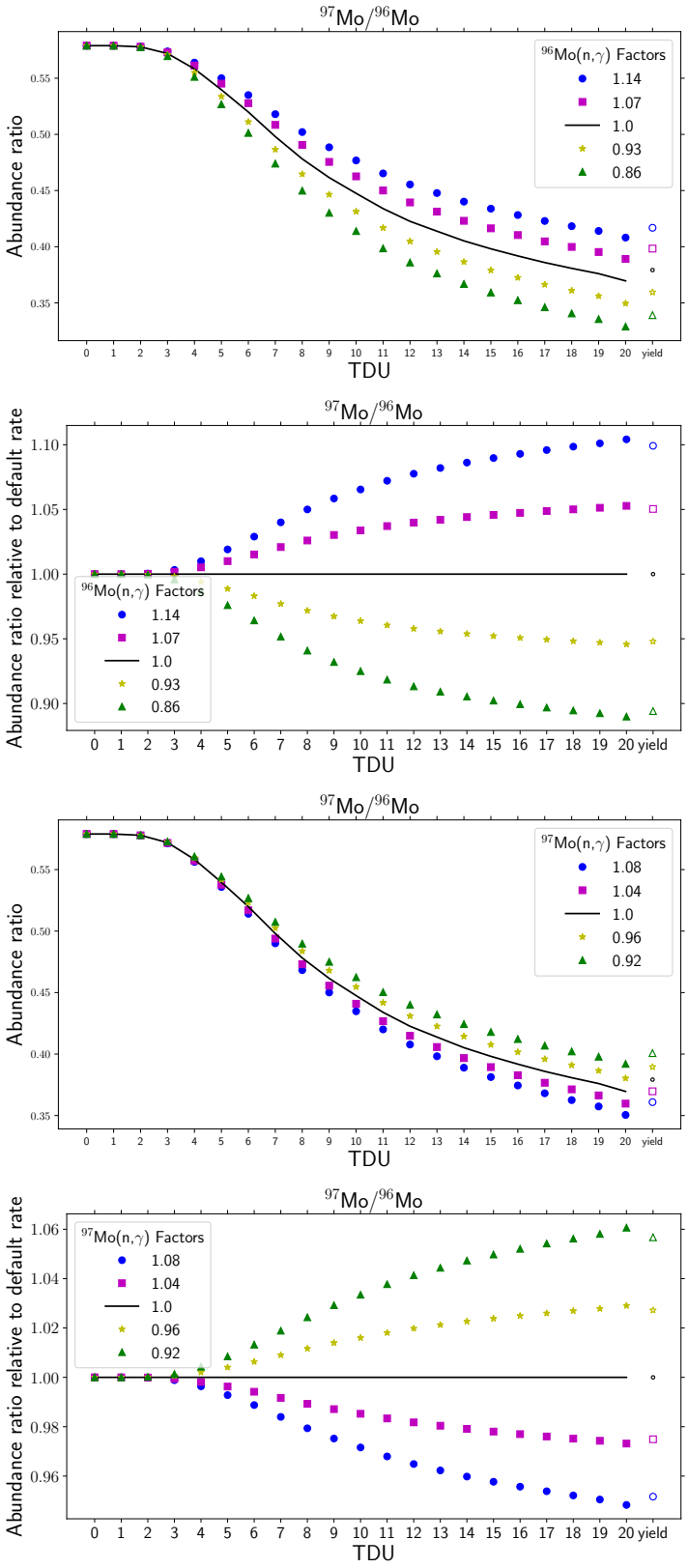

Figure B.11 *The evolution of $^{97}Mo/^{96}Mo$ abundances through the life of a $M=3M_{\odot}$, $Z=0.02$ star, observing the impact of the $^{96}Mo(n,\gamma)$ and $^{97}Mo(n,\gamma)$ key reactions on this ratio.*

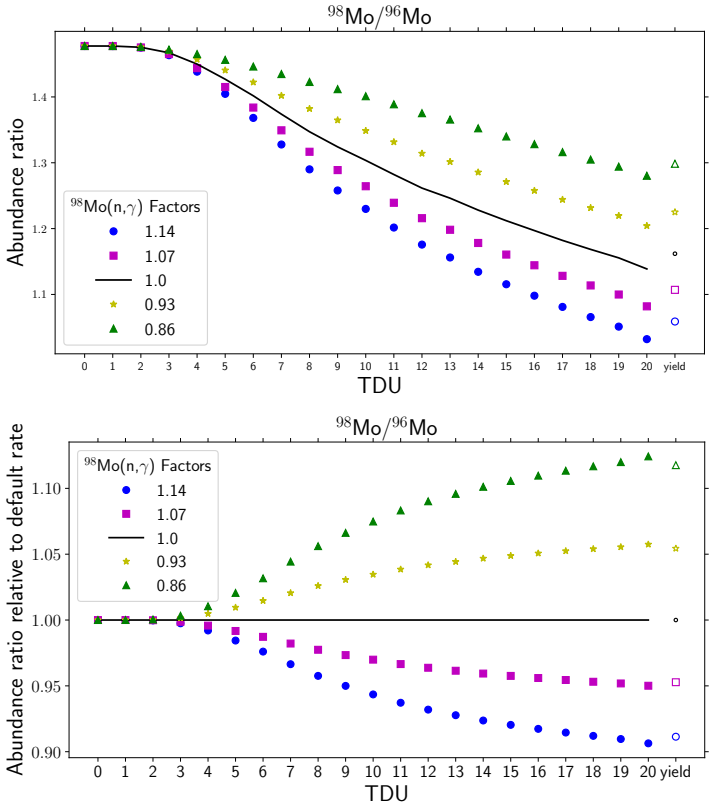

Figure B.12 *The evolution of $^{98}Mo/^{96}Mo$ abundances through the life of a $M=3M_{\odot}$, $Z=0.02$ star, observing the impact of the $^{98}Mo(n,\gamma)$ key reaction on this ratio.*

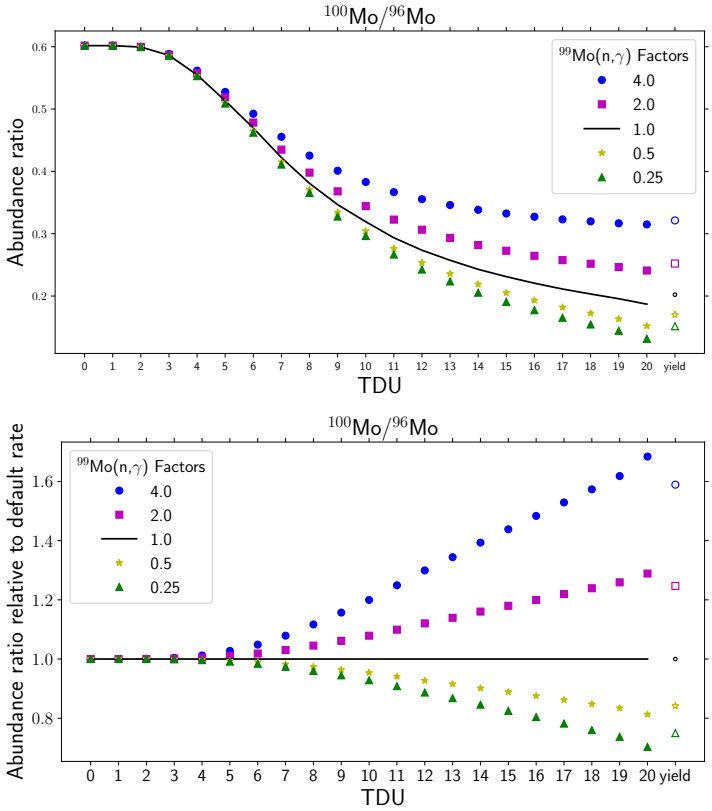

Figure B.13 *The evolution of $^{95}Mo/^{96}Mo$ abundances through the life of a $M=3M_{\odot}$, $Z=0.02$ star, observing the impact of the $^{99}Mo(n,\gamma)$ key reaction on this ratio.*

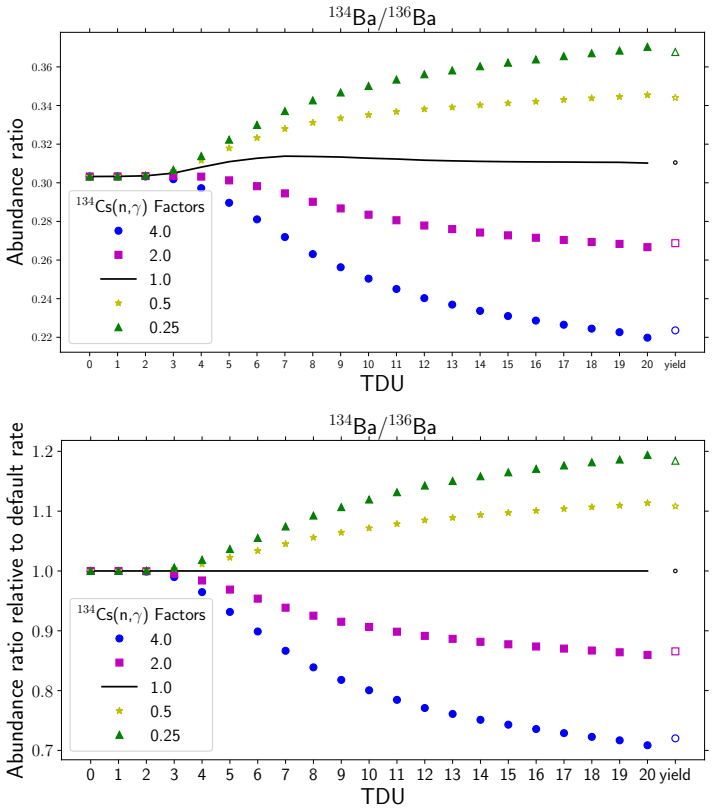

Figure B.14 *The evolution of $^{134}Ba/^{136}Ba$ abundances through the life of a $M=3M_{\odot}$, $Z=0.02$ star, observing the impact of the $^{134}Cs(n,\gamma)$ branching point on this ratio.*

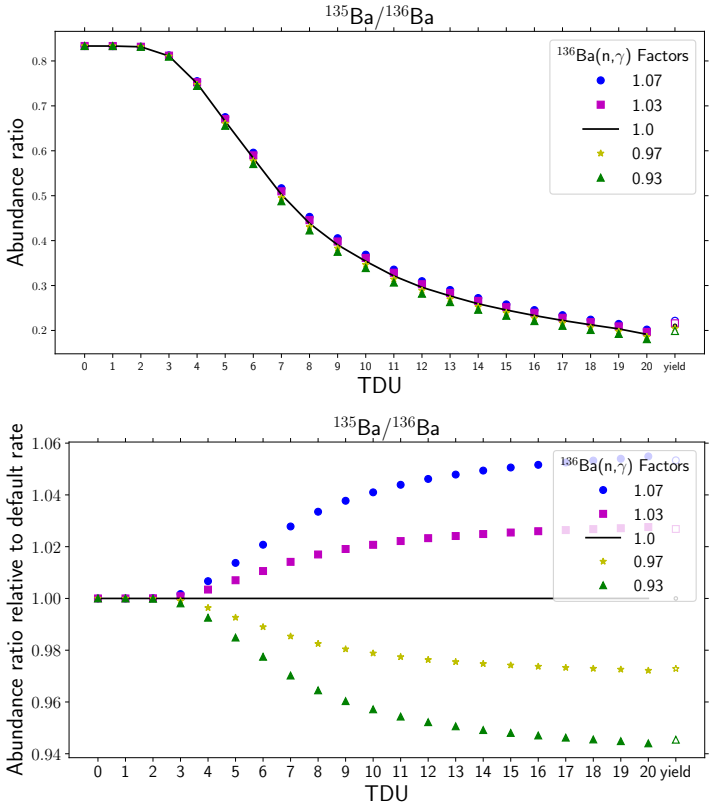

Figure B.15 *The evolution of $^{135}Ba/^{136}Ba$ abundances through the life of a $M=3M_{\odot}$, $Z=0.02$ star, observing the impact of the $^{136}Ba(n,\gamma)$ key reaction on this ratio.*

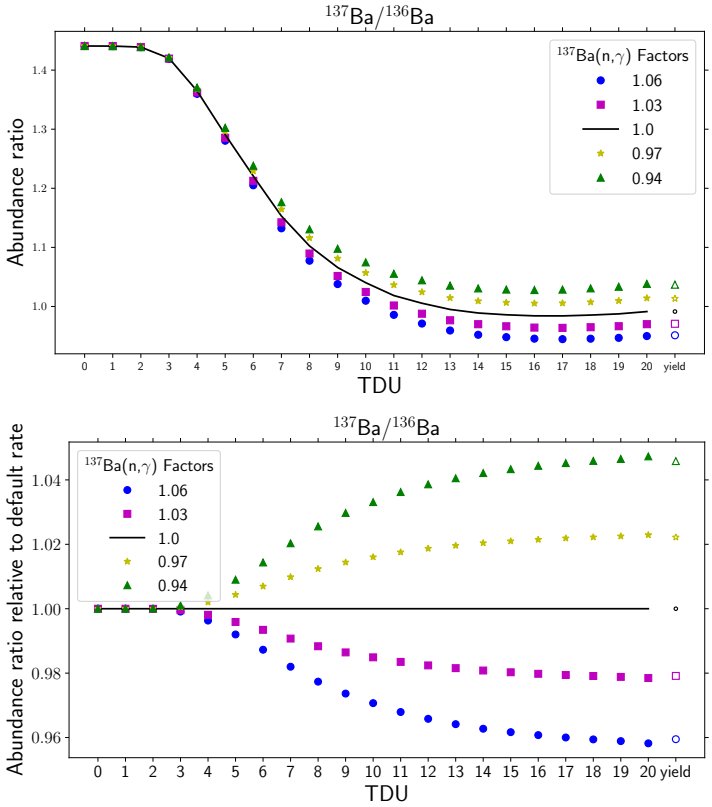

Figure B.16 *The evolution of $^{137}Ba/^{136}Ba$ abundances through the life of a $M=3M_{\odot}$, $Z=0.02$ star, observing the impact of the $^{137}Ba(n,\gamma)$ key reaction on this ratio.*

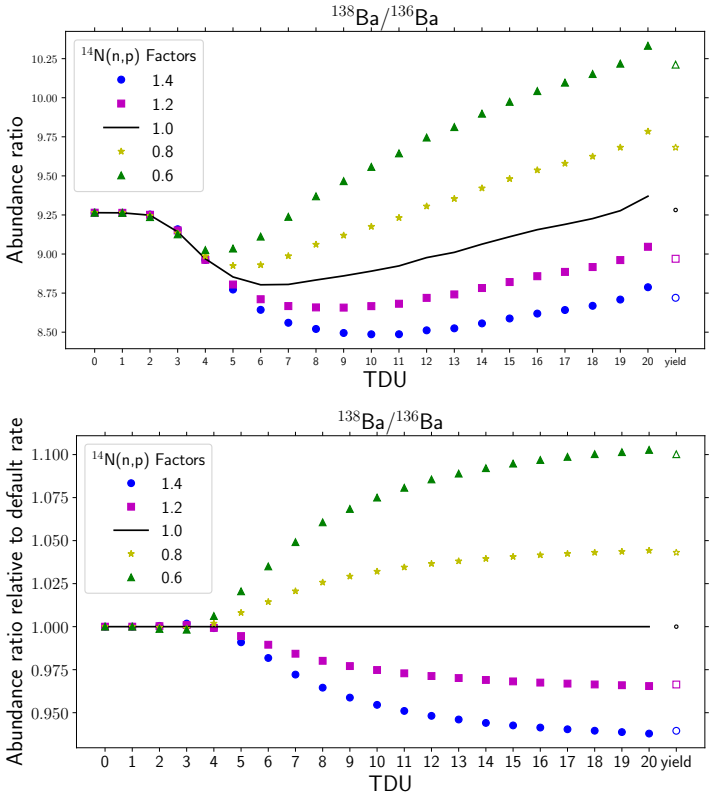

Figure B.17 *The evolution of $^{138}Ba/^{136}Ba$ abundances through the life of a $M=3M_{\odot}$, $Z=0.02$ star, observing the impact of the $^{14}N(n,p)$ key reaction on this ratio.*

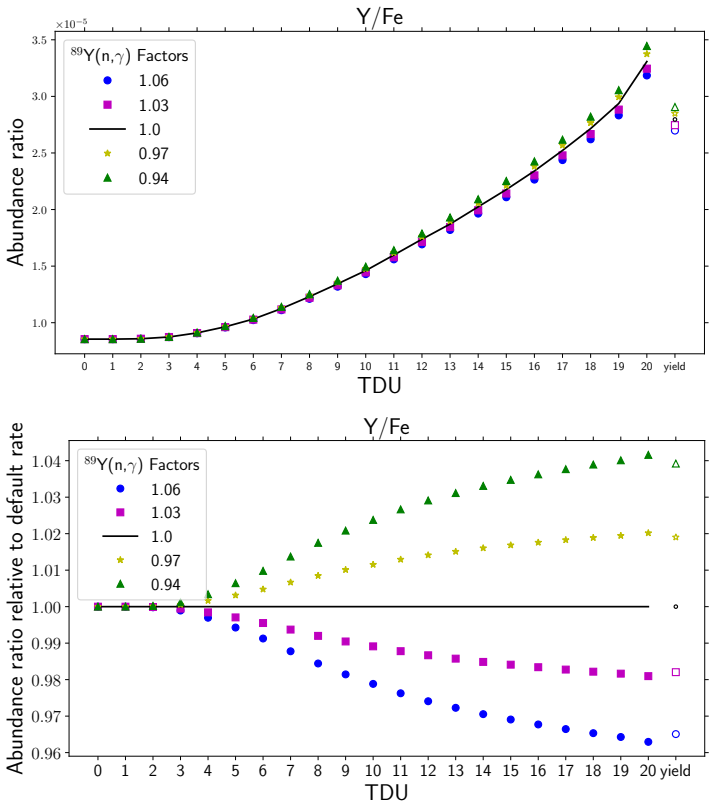

Figure B.18 *The evolution of Y/Fe abundances through the life of a M=3M$_\odot$, Z=0.02 star, observing the impact of the $^{89}Y(n,\gamma)$ key reaction on this ratio.*

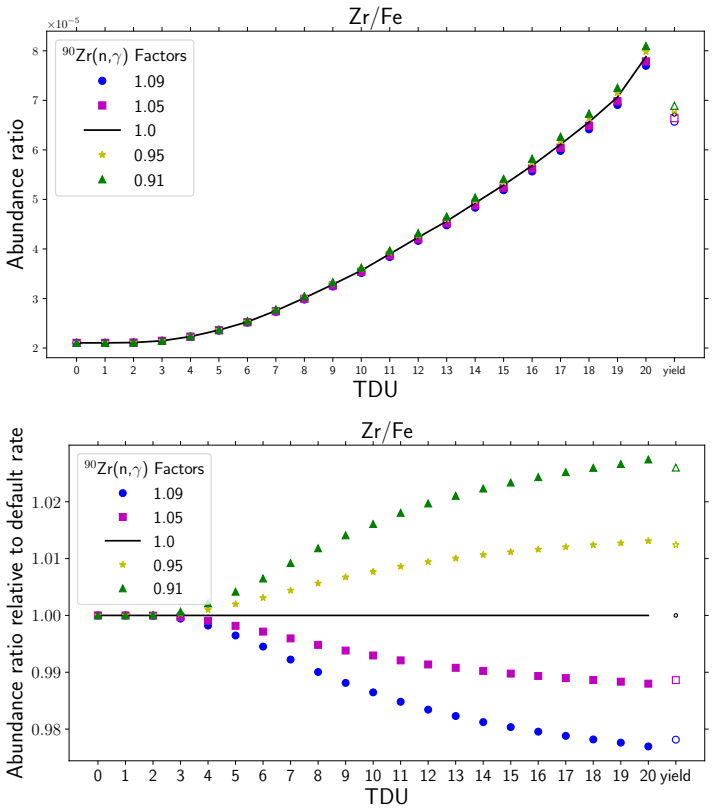

Figure B.19 *The evolution of Zr/Fe abundances through the life of a M=3M$_\odot$, Z=0.02 star, observing the impact of the ^{90}Zr(n,γ) key reaction on this ratio.*

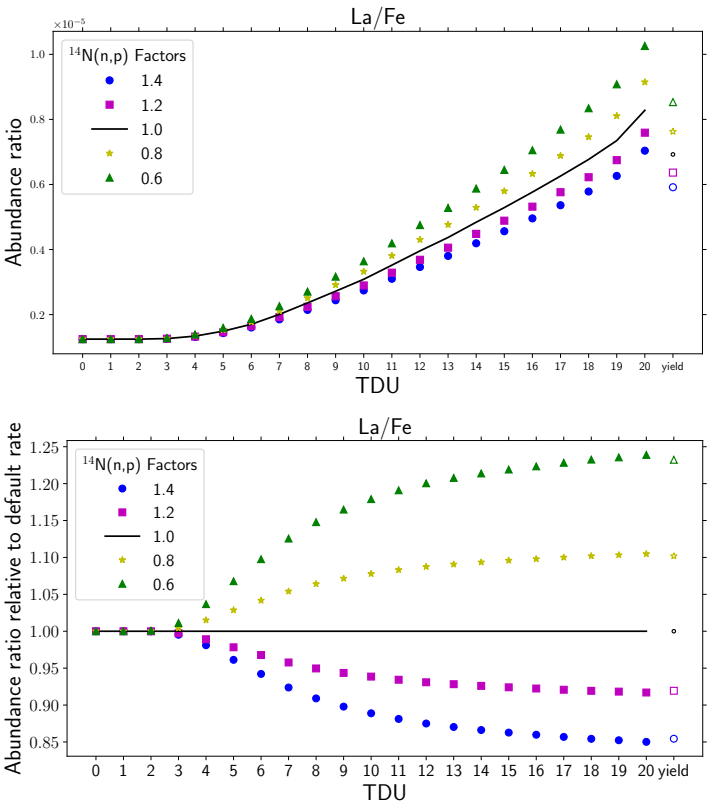

Figure B.20 *The evolution of La/Fe abundances through the life of a $M=3M_{\odot}$, $Z=0.02$ star, observing the impact of the $^{14}N(n,p)$ key reaction on this ratio.*

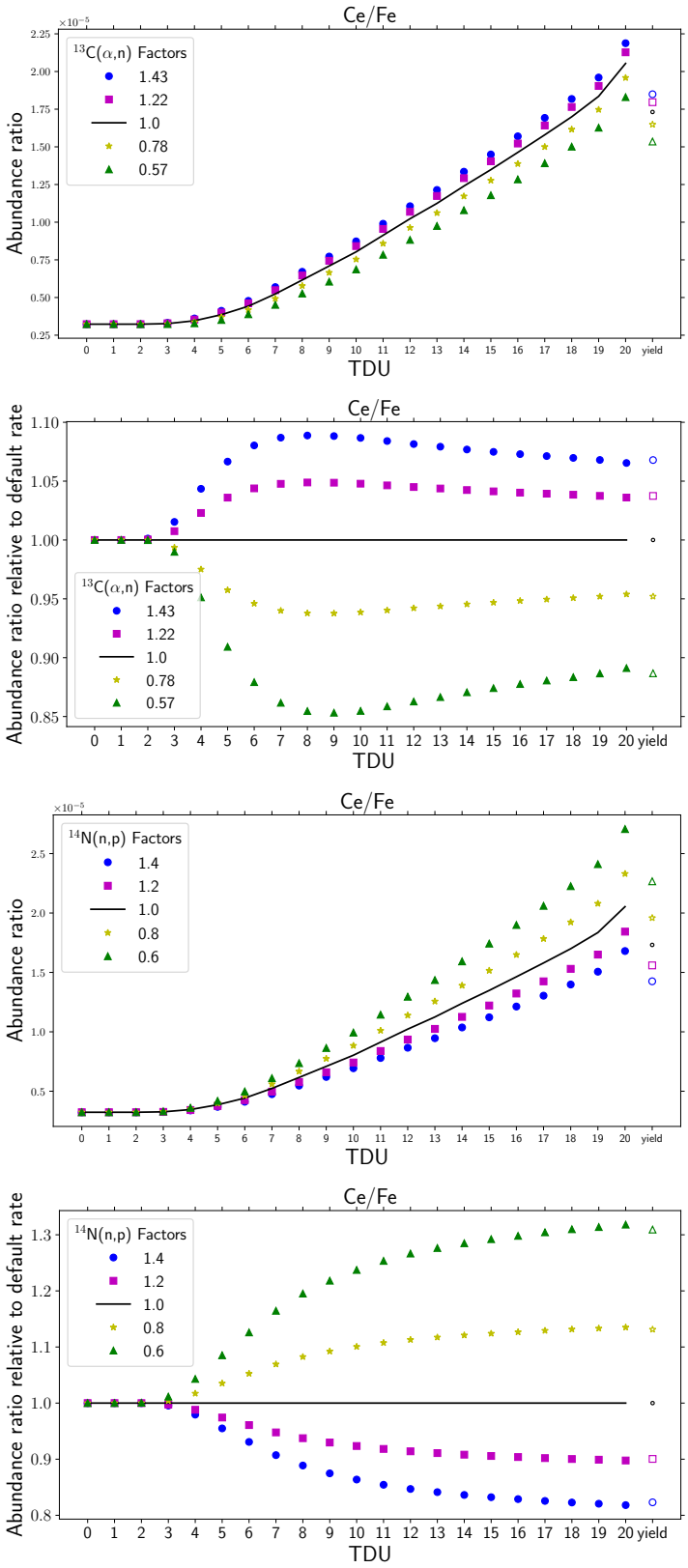

Figure B.21 *The evolution of Ce/Fe abundances through the life of a $M=3M_{\odot}$, $Z=0.02$ star, observing the impact of the $^{13}C(\alpha,n)$ and $^{14}N(n,p)$ key reactions on this ratio.*

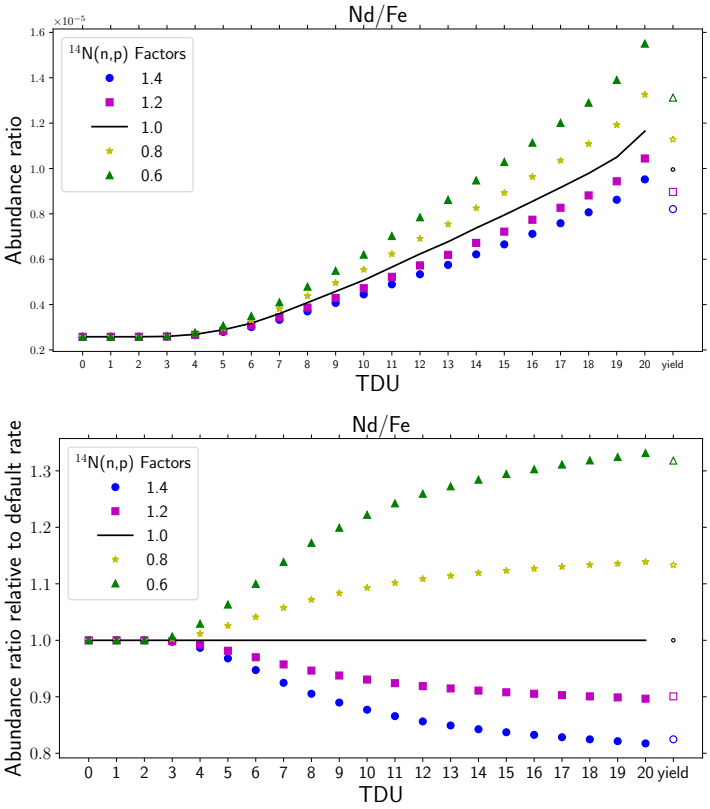

Figure B.22 *The evolution of Nd/Fe abundances through the life of a $M=3M_{\odot}$, $Z=0.02$ star, observing the impact of the $^{14}N(n,p)$ key reaction on this ratio.*

^{84}Sr/^{86}Sr	^{13}C(α,n)	^{14}N(n,p)	^{86}Sr(n,γ)	^{84}Sr(n,γ)	
+2σ	+0.00024	-0.00002	+0.0012	-0.000004	
-2σ	-0.00019	+0.00024	-0.0013	+0.000055	
Ratio =	0.0345	+0.0012	-0.0013		
^{87}Sr/^{86}Sr	^{13}C(α,n)	^{14}N(n,p)	^{86}Sr(n,γ)	^{87}Sr(n,γ)	
+2σ	+0.00063	-0.00017	+0.024	-0.020	
-2σ	-0.00089	+0.00048	-0.027	+0.024	
Ratio =	0.727	+0.034	-0.034		
^{88}Sr/^{86}Sr	^{13}C(α,n)	^{14}N(n,p)	^{86}Sr(n,γ)	^{88}Sr(n,γ)	^{56}Fe(n,γ)
+2σ	+0.10	-0.10	+0.35	-0.37	+0.011
-2σ	-0.22	+0.11	-0.39	+0.43	-0.015
Ratio =	10.22	+0.68	-0.63		
^{90}Zr/^{94}Zr	^{13}C(α,n)	^{14}N(n,p)	^{94}Zr(n,γ)	^{90}Zr(n,γ)	
+2σ	-0.015	+0.027	+0.162	-0.091	
-2σ	+0.030	-0.032	-0.179	+0.110	
Ratio =	2.18	+0.20	-0.20		
^{91}Zr/^{94}Zr	^{13}C(α,n)	^{14}N(n,p)	^{94}Zr(n,γ)	^{91}Zr(n,γ)	
+2σ	-0.0033	+0.0052	+0.041	-0.032	
-2σ	+0.0058	-0.0065	-0.045	+0.041	
Ratio =	0.549	+0.058	-0.056		
^{92}Zr/^{94}Zr	^{13}C(α,n)	^{14}N(n,p)	^{94}Zr(n,γ)	^{92}Zr(n,γ)	
+2σ	-0.0042	+0.060	+0.064	-0.062	
-2σ	+0.0073	-0.075	-0.071	+0.085	
Ratio =	0.86	+0.11	-0.09		
^{96}Zr/^{94}Zr	^{13}C(α,n)	^{14}N(n,p)	^{94}Zr(n,γ)		
+2σ	-0.0008	+0.0010	+0.0077		
-2σ	+0.0018	-0.0007	-0.0086		
Ratio =	0.104	+0.008	-0.009		
^{92}Mo/^{96}Mo	^{13}C(α,n)	^{14}N(n,p)	^{64}Ni(n,γ)	^{96}Mo(n,γ)	
+2σ	-0.005	+0.010	-0.0034	+0.024	
-2σ	+0.012	-0.009	+0.0049	-0.027	
Ratio =	0.327	+0.026	-0.028		

Table B.1 *The abundance variation values from the MPPNP tests for the 16th inter-pulse ^{13}C-pocket. Given in the table are a few reactions investigated, some of the included reactions were used in the final uncertainty calculation, and some reactions were not (see Table 4.3). The reactions not used are clearly seen as having an abundance change of close to a magnitude or more lower compared to the other reactions that were used in the calculation. The reactions with lower abundance change were found to have a significant Pearson correlation in the Monte Carlo study but when changing from the single zone to multi-zone models those reaction were no longer important. The values provided in this table are for the 16th inter-pulse including the default abundance value and its corresponding uncertainty for the ^{13}C-pocket case.*

^{94}Mo/^{96}Mo	^{13}C(α,n)	^{14}N(n,p)	^{96}Mo(n,γ)		
+2σ	-0.0027	+0.0066	+0.016		
-2σ	+0.0075	-0.0062	-0.018		
Ratio =	0.214	+0.016	-0.018		
^{95}Mo/^{96}Mo	^{13}C(α,n)	^{14}N(n,p)	^{95}Mo(n,γ)	^{96}Mo(n,γ)	
+2σ	-0.0030	+0.0053	-0.021	+0.053	
-2σ	+0.0074	-0.0055	+0.024	-0.060	
Ratio =	0.719	+0.059	0.064		
^{97}Mo/^{96}Mo	^{13}C(α,n)	^{14}N(n,p)	^{97}Mo(n,γ)	^{96}Mo(n,γ)	
+2σ	-0.0011	+0.0029	-0.015	+0.033	
-2σ	+0.0033	-0.0026	+0.017	-0.037	
Ratio =	0.423	+0.037	-0.040		
^{98}Mo/^{96}Mo	^{13}C(α,n)	^{14}N(n,p)	^{98}Mo(n,γ)	^{96}Mo(n,γ)	
+2σ	-0.0003	+0.0022	-0.086	+0.095	
-2σ	+0.0020	-0.0007	+0.114	-0.107	
Ratio =	1.26	+0.15	-0.14		
^{100}Mo/^{96}Mo	^{13}C(α,n)	^{14}N(n,p)	^{99}Mo(n,γ)	^{96}Mo(n,γ)	^{100}Mo(n,γ)
+2σ	-0.0031	+0.0065	+0.082	+0.020	-0.0093
-2σ	+0.0083	-0.0061	-0.031	-0.023	+0.0140
Ratio =	0.274	+0.086	-0.040		
^{134}Ba/^{136}Ba	^{13}C(α,n)	^{14}N(n,p)	^{134}Ba(n,γ)	^{136}Ba(n,γ)	
+2σ	-0.00025	+0.0014	-0.012	+0.014	
-2σ	+0.00053	-0.0020	+0.014	-0.015	
Ratio =	0.312	+0.020	-0.019		
^{135}Ba/^{136}Ba	^{13}C(α,n)	^{14}N(n,p)	^{135}Ba(n,γ)	^{136}Ba(n,γ)	
+2σ	-0.008	+0.016	-0.0045	+0.014	
-2σ	+0.016	-0.018	+0.0052	-0.014	
Ratio =	0.296	+0.028	-0.025		
^{137}Ba/^{136}Ba	^{13}C(α,n)	^{14}N(n,p)	^{137}Ba(n,γ)	^{136}Ba(n,γ)	
+2σ	-0.006	+0.010	-0.034	+0.047	
-2σ	+0.012	-0.010	+0.039	-0.049	
Ratio =	1.005	+0.063	-0.061		
^{138}Ba/^{136}Ba	^{13}C(α,n)	^{14}N(n,p)	^{138}Ba(n,γ)	^{136}Ba(n,γ)	^{88}Sr(n,γ)
+2σ	+0.19	-0.47	-0.34	+0.43	-0.023
-2σ	-0.34	+0.77	+0.38	-0.45	+0.029
Ratio =	8.98	+0.98	-0.81		

Table B.2 *A continuation of Table B.1*

Y/Fe	^{88}Sr(n,γ)	^{14}N(n,p)	^{89}Y(n,γ)	^{64}Ni(n,γ)		
+2σ	+1.7×10−7	-2.3×10−7	-4.5×10−7	+1.4×10−7		
-2σ	-2.0×10−7	+1.3×10−7	+5.1×10−7	-2.0×10−7		
Ratio =	1.738×10−5	+0.057×10−5	-0.058×10−5			
Zr/Fe	^{14}N(n,p)	^{64}Ni(n,γ)	^{88}Sr(n,γ)	^{90}Zr(n,γ)	^{92}Zr(n,γ)	^{94}Zr(n,γ)
+2σ	-8.5×10−7	+3.5×10−7	+4.7×10−7	-7.0×10−7	-4.7×10−7	-6.0×10−7
-2σ	+7.3×10−7	-5.1×10−7	-5.5×10−7	+8.3×10−7	+6.4×10−7	+7.7×10−7
Ratio =	4.24×10−5	+0.15×10−5	-0.16×10−5			
La/Fe	^{13}C(α,n)	^{14}N(n,p)	^{139}La(n,γ)			
+2σ	+2.5×10−7	-4.9×10−7	-4.1×10−7			
-2σ	-4.5×10−7	+7.9×10−7	+5.8×10−7			
Ratio =	3.96×10−6	+1.03×10−6	-0.81×10−6			
Ce/Fe	^{13}C(α,n)	^{14}N(n,p)	^{138}Ba(n,γ)	^{16}O(n,γ)	^{140}Ce(n,γ)	
+2σ	+0.8×10−6	-1.6×10−6	+3.1×10−7	-3.0×10−7	-3.7×10−7	
-2σ	-1.4×10−6	+2.7×10−6	-3.5×10−7	+3.0×10−7	+4.0×10−7	
Ratio =	1.02×10−5	+0.29×10−5	-0.22×10−5			
Nd/Fe	^{13}C(α,n)	^{14}N(n,p)	^{138}Ba(n,γ)			
+2σ	-4.7×10−7	-0.9×10−6	+1.6×10−7			
-2σ	+7.9×10−7	+1.6×10−6	-1.8×10−7			
Ratio =	6.23×10−6	+1.71×10−6	-1.22×10−6			

Table B.3 *A continuation of Table B.1 and Table B.2*

Abundance	TP 16 [$M_\odot$]	TP 18 [$M_\odot$]	TP 20 [$M_\odot$]	TP 22 [$M_\odot$]	TP 24 [$M_\odot$]	Yield [$M_\odot$]
$^{84}Sr/^{86}Sr$	$0.0345^{+0.0012}_{-0.0013}$	$0.0310^{+0.0013}_{-0.0014}$	$0.0277^{+0.0013}_{-0.0014}$	$0.0241^{+0.0013}_{-0.0014}$	$0.0188^{+0.0011}_{-0.0012}$	$0.0227^{+0.0012}_{-0.0013}$
$^{87}Sr/^{86}Sr$	$0.727^{+0.034}_{-0.034}$	$0.719^{+0.040}_{-0.039}$	$0.711^{+0.045}_{-0.044}$	$0.697^{+0.049}_{-0.048}$	$0.672^{+0.055}_{-0.053}$	$0.688^{+0.050}_{-0.09}$
$^{88}Sr/^{86}Sr$	$10.22^{+0.68}_{-0.63}$	$10.55^{+0.83}_{-0.74}$	$10.80^{+0.95}_{-0.85}$	$10.84^{+1.06}_{-0.94}$	$10.35^{+1.15}_{-1.00}$	$10.54^{+0.82}_{-0.87}$
$^{90}Zr/^{94}Zr$	$2.18^{+0.20}_{-0.20}$	$2.09^{+0.22}_{-0.22}$	$2.01^{+0.23}_{-0.22}$	$1.95^{+0.23}_{-0.23}$	$1.88^{+0.24}_{-0.23}$	$1.94^{+0.23}_{-0.23}$
$^{91}Zr/^{94}Zr$	$0.549^{+0.058}_{-0.056}$	$0.540^{+0.065}_{-0.061}$	$0.534^{+0.069}_{-0.065}$	$0.530^{+0.074}_{-0.068}$	$0.525^{+0.078}_{-0.072}$	$0.529^{+0.074}_{-0.069}$
$^{92}Zr/^{94}Zr$	$0.86^{+0.11}_{-0.09}$	$0.85^{+0.12}_{-0.10}$	$0.85^{+0.13}_{-0.11}$	$0.85^{+0.14}_{-0.12}$	$0.85^{+0.15}_{-0.13}$	$0.85^{+0.14}_{-0.12}$
$^{96}Zr/^{94}Zr$	$0.104^{+0.008}_{-0.009}$	$0.105^{+0.009}_{-0.010}$	$0.110^{+0.010}_{-0.011}$	$0.118^{+0.011}_{-0.012}$	$0.131^{+0.013}_{-0.014}$	$0.124^{+0.012}_{-0.013}$
$^{92}Mo/^{96}Mo$	$0.327^{+0.026}_{-0.028}$	$0.270^{+0.026}_{-0.027}$	$0.227^{+0.023}_{-0.023}$	$0.191^{+0.020}_{-0.020}$	$0.154^{+0.016}_{-0.017}$	$0.185^{+0.019}_{-0.020}$
$^{94}Mo/^{96}Mo$	$0.214^{+0.016}_{-0.018}$	$0.178^{+0.017}_{-0.017}$	$0.150^{+0.015}_{-0.015}$	$0.127^{+0.013}_{-0.013}$	$0.103^{+0.011}_{-0.011}$	$0.123^{+0.012}_{-0.013}$
$^{95}Mo/^{96}Mo$	$0.719^{+0.059}_{-0.064}$	$0.701^{+0.064}_{-0.068}$	$0.689^{+0.067}_{-0.071}$	$0.681^{+0.070}_{-0.073}$	$0.676^{+0.072}_{-0.075}$	$0.683^{+0.070}_{-0.073}$
$^{97}Mo/^{96}Mo$	$0.423^{+0.037}_{-0.040}$	$0.405^{+0.040}_{-0.042}$	$0.392^{+0.042}_{-0.043}$	$0.381^{+0.043}_{-0.044}$	$0.370^{+0.045}_{-0.045}$	$0.379^{+0.043}_{-0.044}$
$^{98}Mo/^{96}Mo$	$1.26^{+0.15}_{-0.14}$	$1.23^{+0.16}_{-0.15}$	$1.20^{+0.17}_{-0.15}$	$1.17^{+0.17}_{-0.16}$	$1.139^{+0.18}_{-0.16}$	$1.16^{+0.15}_{-0.17}$
$^{100}Mo/^{96}Mo$	$0.274^{+0.086}_{-0.040}$	$0.243^{+0.10}_{-0.05}$	$0.221^{+0.11}_{-0.05}$	$0.203^{+0.12}_{-0.06}$	$0.187^{+0.13}_{-0.06}$	$0.202^{+0.12}_{-0.06}$
$^{134}Ba/^{136}Ba$	$0.312^{+0.020}_{-0.019}$	$0.311^{+0.021}_{-0.020}$	$0.311^{+0.022}_{-0.021}$	$0.311^{+0.022}_{-0.021}$	$0.310^{+0.023}_{-0.022}$	$0.311^{+0.022}_{-0.021}$
$^{135}Ba/^{136}Ba$	$0.296^{+0.028}_{-0.025}$	$0.259^{+0.023}_{-0.022}$	$0.233^{+0.020}_{-0.019}$	$0.213^{+0.018}_{-0.018}$	$0.191^{+0.016}_{-0.016}$	$0.210^{+0.018}_{-0.017}$
$^{137}Ba/^{136}Ba$	$1.005^{+0.063}_{-0.061}$	$0.989^{+0.066}_{-0.064}$	$0.984^{+0.068}_{-0.066}$	$0.985^{+0.070}_{-0.068}$	$0.991^{+0.072}_{-0.070}$	$0.991^{+0.068}_{-0.070}$
$^{138}Ba/^{136}Ba$	$8.98^{+0.98}_{-0.81}$	$9.06^{+1.06}_{-0.86}$	$9.16^{+1.12}_{-0.90}$	$9.23^{+1.17}_{-0.93}$	$9.37^{+1.22}_{-0.96}$	$9.28^{+1.18}_{-0.93}$
Y/Fe	$(1.738^{+0.057}_{-0.058}) \times 10{-}5$	$(2.024^{+0.074}_{-0.075}) \times 10{-}5$	$(2.341^{+0.093}_{-0.094}) \times 10{-}5$	$(2.71^{+0.12}_{-0.12}) \times 10{-}5$	$(3.31^{+0.15}_{-0.15}) \times 10{-}5$	$(2.80^{+0.12}_{-0.12}) \times 10{-}5$
Zr/Fe	$(4.24^{+0.15}_{-0.16}) \times 10{-}5$	$(4.93^{+0.21}_{-0.20}) \times 10{-}5$	$(5.68^{+0.26}_{-0.25}) \times 10{-}5$	$(6.56^{+0.32}_{-0.30}) \times 10{-}5$	$(7.88^{+0.40}_{-0.39}) \times 10{-}5$	$(6.72^{+0.33}_{-0.31}) \times 10{-}5$
La/Fe	$(3.96^{+1.03}_{-0.81}) \times 10{-}6$	$(4.84^{+1.34}_{-1.02}) \times 10{-}6$	$(5.77^{+1.66}_{-1.24}) \times 10{-}6$	$(6.77^{+2.03}_{-1.49}) \times 10{-}6$	$(8.28^{+2.55}_{-1.85}) \times 10{-}6$	$(6.92^{+2.07}_{-1.52}) \times 10{-}6$
Ce/Fe	$(1.02^{+0.29}_{-0.22}) \times 10{-}5$	$(1.24^{+0.37}_{-0.27}) \times 10{-}5$	$(1.46^{+0.46}_{-0.32}) \times 10{-}5$	$(1.70^{+0.55}_{-0.38}) \times 10{-}5$	$(2.05^{+0.68}_{-0.46}) \times 10{-}5$	$(1.73^{+0.56}_{-0.38}) \times 10{-}5$
Nd/Fe	$(6.23^{+1.71}_{-1.22}) \times 10{-}6$	$(7.38^{+2.19}_{-1.52}) \times 10{-}6$	$(8.55^{+2.69}_{-1.81}) \times 10{-}6$	$(9.78^{+3.23}_{-2.12}) \times 10{-}6$	$(1.16^{+0.40}_{-0.26}) \times 10{-}5$	$(9.96^{+3.28}_{-2.14}) \times 10{-}6$

Table B.4 *Ratios for isotopes and elements seen in grains and observations taken from AGB stars that are relevant to the ^{13}C-pocket with alternate carbon rich surface enrichment data points on the plots in Chapter 3 are included as well as the yield include uncertainty from reaction rates. The uncertainty provided is for 2σ reaction rate uncertainty value.*

Abundance	TP 16 [$M_\odot$]	TP 18 [$M_\odot$]	TP 20 [$M_\odot$]	TP 22 [$M_\odot$]	TP 24 [$M_\odot$]	Yield [$M_\odot$]
$^{84}Sr/^{86}Sr$	$0.0345^{+0.0049}_{-0.0029}$	$0.0310^{+0.0054}_{-0.0032}$	$0.0277^{+0.0058}_{-0.0033}$	$0.0241^{+0.0061}_{-0.0033}$	$0.0188^{+0.0062}_{-0.0030}$	$0.0227^{+0.0062}_{-0.0032}$
$^{87}Sr/^{86}Sr$	$0.727^{+0.024}_{-0.015}$	$0.719^{+0.028}_{-0.016}$	$0.711^{+0.032}_{-0.017}$	$0.697^{+0.036}_{-0.017}$	$0.672^{+0.038}_{-0.014}$	$0.688^{+0.036}_{-0.016}$
$^{88}Sr/^{86}Sr$	$10.22^{+1.19}_{-0.75}$	$10.55^{+1.54}_{-0.94}$	$10.80^{+1.92}_{-1.12}$	$10.84^{+2.34}_{-1.29}$	$10.35^{+2.92}_{-1.46}$	$10.54^{+2.48}_{-1.32}$
$^{90}Zr/^{94}Zr$	$2.1768^{+0.0005}_{-0.0041}$	$2.0871^{+0.0097}_{-0.0036}$	$2.014^{+0.022}_{-0.003}$	$1.950^{+0.038}_{-0.002}$	$1.883^{+0.062}_{-0.002}$	$1.938^{+0.047}_{-0.002}$
$^{91}Zr/^{94}Zr$	$0.5488^{+0.0004}_{-0.0034}$	$0.5404^{+0.0017}_{-0.0051}$	$0.5344^{+0.0043}_{-0.0072}$	$0.5295^{+0.0077}_{-0.0095}$	$0.5253^{+0.013}_{-0.013}$	$0.5294^{+0.010}_{-0.011}$
$^{92}Zr/^{94}Zr$	$0.8606^{+0.0123}_{-0.0001}$	$0.8529^{+0.0142}_{-0.0002}$	$0.8485^{+0.0162}_{-0.0006}$	$0.8459^{+0.0179}_{-0.0006}$	$0.845^{+0.019}_{-0.001}$	$0.847^{+0.018}_{-0.001}$
$^{96}Zr/^{94}Zr$	$0.104^{+0.078}_{-0.026}$	$0.105^{+0.098}_{-0.035}$	$0.11^{+0.12}_{-0.04}$	$0.12^{+0.14}_{-0.06}$	$0.13^{+0.18}_{-0.07}$	$0.12^{+0.15}_{-0.06}$
$^{92}Mo/^{96}Mo$	$0.327^{+0.043}_{-0.015}$	$0.270^{+0.043}_{-0.016}$	$0.227^{+0.043}_{-0.016}$	$0.191^{+0.042}_{-0.016}$	$0.154^{+0.039}_{-0.015}$	$0.185^{+0.042}_{-0.016}$
$^{94}Mo/^{96}Mo$	$0.214^{+0.025}_{-0.007}$	$0.1782^{+0.025}_{-0.07}$	$0.1502^{+0.026}_{-0.008}$	$0.1267^{+0.025}_{-0.008}$	$0.1027^{+0.023}_{-0.007}$	$0.1232^{+0.025}_{-0.008}$
$^{95}Mo/^{96}Mo$	$0.719^{+0.023}_{-0.018}$	$0.7009^{+0.025}_{-0.020}$	$0.6892^{+0.026}_{-0.021}$	$0.6814^{+0.027}_{-0.021}$	$0.6760^{+0.027}_{-0.022}$	$0.6825^{+0.026}_{-0.021}$
$^{97}Mo/^{96}Mo$	$0.4226^{+0.030}_{-0.013}$	$0.4052^{+0.034}_{-0.015}$	$0.3918^{+0.039}_{-0.017}$	$0.3808^{+0.043}_{-0.019}$	$0.3696^{+0.049}_{-0.021}$	$0.3792^{+0.045}_{-0.020}$
$^{98}Mo/^{96}Mo$	$1.262^{+0.095}_{-0.045}$	$1.23^{+0.12}_{-0.06}$	$1.20^{+0.14}_{-0.07}$	$1.17^{+0.16}_{-0.08}$	$1.14^{+0.18}_{-0.09}$	$1.16^{+0.16}_{-0.08}$
$^{100}Mo/^{96}Mo$	$0.27^{+0.031}_{-0.012}$	$0.243^{+0.033}_{-0.013}$	$0.221^{+0.035}_{-0.014}$	$0.203^{+0.037}_{-0.016}$	$0.187^{+0.038}_{-0.017}$	$0.202^{+0.038}_{-0.016}$
$^{134}Ba/^{136}Ba$	$0.312^{+0.062}_{-0.048}$	$0.311^{+0.066}_{-0.052}$	$0.311^{+0.068}_{-0.056}$	$0.311^{+0.070}_{-0.058}$	$0.310^{+0.072}_{-0.061}$	$0.311^{+0.070}_{-0.059}$
$^{135}Ba/^{136}Ba$	$0.296^{+0.012}_{-0.009}$	$0.259^{+0.010}_{-0.011}$	$0.233^{+0.007}_{-0.013}$	$0.213^{+0.005}_{-0.015}$	$0.191^{+0.002}_{-0.017}$	$0.210^{+0.006}_{-0.015}$
$^{137}Ba/^{136}Ba$	$1.01^{+0.15}_{-0.05}$	$0.99^{+0.17}_{-0.06}$	$0.98^{+0.19}_{-0.08}$	$0.99^{+0.21}_{-0.10}$	$0.99^{+0.24}_{-0.12}$	$0.99^{+0.22}_{-0.10}$
$^{138}Ba/^{136}Ba$	$8.98^{+0.15}_{-0.05}$	$9.06^{+0.17}_{-0.06}$	$9.16^{+0.19}_{-0.08}$	$9.23^{+0.21}_{-0.10}$	$9.37^{+0.24}_{-0.12}$	$9.28^{+0.22}_{-0.10}$
Y/Fe	$(1.738^{+0.087}_{-0.031}) \times 10{-}5$	$(2.02^{+0.12}_{-0.05}) \times 10{-}5$	$(2.34^{+0.17}_{-0.07}) \times 10{-}5$	$(2.72^{+0.23}_{-0.09}) \times 10{-}5$	$(3.31^{+0.34}_{-0.14}) \times 10{-}5$	$(2.80^{+0.25}_{-0.10}) \times 10{-}5$
Zr/Fe	$(4.2350^{+0.0089}_{-0.0036}) \times 10{-}5$	$(4.927^{+0.006}_{-0.010}) \times 10{-}5$	$(5.682^{+0.031}_{-0.021}) \times 10{-}5$	$(6.561^{+0.067}_{-0.038}) \times 10{-}5$	$(7.880^{+0.14}_{-0.07}) \times 10{-}5$	$(6.716^{+0.085}_{-0.047}) \times 10{-}5$
La/Fe	$(3.96^{+0.11}_{-0.02}) \times 10{-}6$	$(4.84^{+0.15}_{-0.03}) \times 10{-}6$	$(5.77^{+0.20}_{-0.04}) \times 10{-}6$	$(6.77^{+0.24}_{-0.05}) \times 10{-}6$	$(8.28^{+0.33}_{-0.07}) \times 10{-}6$	$(6.92^{+0.26}_{-0.06}) \times 10{-}6$
Ce/Fe	$(1.023^{+0.013}_{-0.015}) \times 10{-}5$	$(1.240^{+0.021}_{-0.022}) \times 10{-}5$	$(1.463^{+0.030}_{-0.031}) \times 10{-}5$	$(1.699^{+0.041}_{-0.042}) \times 10{-}5$	$(2.053^{+0.057}_{-0.059}) \times 10{-}5$	$(1.731^{+0.043}_{-0.045}) \times 10{-}5$
Nd/Fe	$(6.23^{+0.24}_{-0.04}) \times 10{-}6$	$(7.38^{+0.36}_{-0.08}) \times 10{-}6$	$(8.55^{+0.50}_{-0.14}) \times 10{-}6$	$(9.78^{+0.66}_{-0.22}) \times 10{-}6$	$(1.164^{+0.094}_{-0.037}) \times 10{-}5$	$(9.96^{+0.71}_{-0.26}) \times 10{-}6$

Table B.5 *Similar to Table B.4, these results are for the branching point uncertainty test.*

Bibliography

[1] Abia, C., et al. 2002, The Astrophysical Journal, 579, 817

[2] Adelberger, E. G., et al. 2011, Rev. Mod. Phys., 83, 195

[3] Adsley, P., et al. 2021, Phys. Rev. C, 103, 015805

[4] Angulo, C., et al. 1999, Nuclear Physics A, 656, 3

[5] Arnould, M., & Goriely, S. 2003, Physics Reports, 384, 1

[6] Bader, G., & Deuflhard, P. 1983, Numerische Mathematik, 41, 373

[7] Bao, Z., Beer, H., Käppeler, F., Voss, F., Wisshak, K., & Rauscher, T. 2000, Atomic Data and Nuclear Data Tables, 76, 70

[8] Barzyk, J. G., et al. 2007, Meteoritics & Planetary Science

[9] Battino, U. 2024, personal communication

[10] Battino, U., Lederer-Woods, C., Cseh, B., Denissenkov, P., & Herwig, F. 2021, Universe, 7, 25

[11] Battino, U., et al. 2016, APJ, 827, 30

[12] Battino, U., Pignatari, M., Travaglio, C., Lederer-Woods, C., Denissenkov, P., Herwig, F., Thielemann, F., & Rauscher, T. 2020, Monthly Notices of the Royal Astronomical Society, 497, 4981

[13] Battino, U., et al. 2019, Monthly Notices of the Royal Astronomical Society, 489, 1082

[14] Best, J., et al. 2001, Phys. Rev. C, 64, 015801

[15] Bisterzo, S., Travaglio, C., Gallino, R., Wiescher, M., & Käppeler, F. 2014, APJ, 787, 10

[16] Bloecker, T. 1995, A&A, 297, 727

[17] Blouin, S., Mao, H., Herwig, F., Denissenkov, P., Woodward, P. R., & Thompson, W. R. 2023, Monthly Notices of the Royal Astronomical Society, 522, 1706

[18] Böhm-Vitense, E. 1958, Zeitschrift fuer Astrophysik, 46, 108

[19] Braithwaite, J., & Spruit, H. C. 2004, Nature, 431, 819

[20] Braithwaite, J. 2006, A&A, 449, 451

[21] Busso, M., Gallino, R., Lambert, D. L., Travaglio, C., & Smith, V. V. 2001, ApJ, 557, 802

[22] Busso, M., Vescovi, D., Palmerini, S., Cristallo, S., & Antonuccio-Delogu, V. 2021, The Astrophysical Journal, 908, 55

[23] Busso, M., Wasserburg, G. J., Nollett, K. M., & Calandra, A. 2007, APJ, 671, 802

[24] Cantiello, M., Mankovich, C., Bildsten, L., Christensen-Dalsgaard, J., & Paxton, B. 2014, APJ, 788, 93

[25] Carobbi, C., Cati, M., & Millanta, L. 2003, in 2003 IEEE Symposium on Electromagnetic Compatibility. Symposium Record (Cat. No.03CH37446), Vol. 2, 812–816 vol.2

[26] Casanova, J., José, J., García-Berro, E., Shore, S. N., & Calder, A. C. 2011, Nature, 478, 490

[27] Cash, J. R., & Karp, A. H. 1990, ACM Trans. Math. Softw., 16, 201–222

[28] Caughlan, G. R., & Fowler, W. A. 1988, Atomic Data and Nuclear Data Tables, 40, 283

[29] Cescutti, G., Hirschi, R., Nishimura, N., Hartogh, J. W. d., Rauscher, T., Murphy, A. S. J., & Cristallo, S. 2018, Monthly Notices of the Royal Astronomical Society, 478, 4101

[30] Chandrasekhar, S. 1961, Hydrodynamic and hydromagnetic stability (Clarendon Press Oxford)

[31] Chugunov, A. I., Dewitt, H. E., & Yakovlev, D. G. 2007, Phys. Rev. D, 76, 025028

[32] Ciani, G. F., et al. 2021, Phys. Rev. Lett., 127, 152701

[33] Cook, C. W., Fowler, W. A., Lauritsen, C. C., & Lauritsen, T. 1957, Phys. Rev., 107, 508

[34] Coquard, L., Käppe, er, Dillmann, I., Wallner, A., Knie, K., & Kutschera, W. 2006, in International Symposium on Nuclear Astrophysics - Nuclei in the Cosmos, ed. A. Mengoni, J. Cederkall, J. D'Auria, L. Fraile, H. Fynbo, M. Hass, M. M. Jeanne, M. Hjorth Jensen, F. Käppeler, K. L. Kratz, M. Lindroos, M. Menna, G. Meynet, & K. Riisager, 274.1

[35] Corvi, F., Fioni, G., Gunsing, F., Mutti, P., & Zanini, L. 2002, Nuclear Physics A, 697, 581

[36] Côté, B., et al. 2019, arXiv e-prints, arXiv:1911.00035

[37] Côté, B., Lugaro, M., Reifarth, R., Pignatari, M., Világos, B., Yagüe, A., & Gibson, B. K. 2019, The Astrophysical Journal, 878, 156

[38] Cowan, J. J., & Thielemann, F.-K. 2004, Physics Today, 57, 47

[39] Cowling, T. G. 1945, Monthly Notices of the Royal Astronomical Society, 105, 166

[40] Cox, J. P., & Giuli, R. T. 1968, Principles of stellar structure (New York: Gordon and Breach)

[41] Cristallo, S., Abia, C., Straniero, O., & Piersanti, L. 2015, The Astrophysical Journal, 801, 53

[42] Cristallo, S., et al. 2018, The Astrophysical Journal, 859, 105

[43] Cristallo, S., Karinkuzhi, D., Goswami, A., Piersanti, L., & Gobrecht, D. 2016, The Astrophysical Journal, 833, 181

[44] Cristallo, S., et al. 2011, APJS, 197, 17

[45] Cristallo, S., Straniero, O., Gallino, R., Herwig, F., Chieffi, A., Limongi, M., & Busso, M. 2001, Nuclear Physics A, 688, 217, nuclei in the Cosmos

[46] Cristallo, S., Straniero, O., Gallino, R., Piersanti, L., Domínguez, I., & Lederer, M. T. 2009, Astrophysical Journal, 696, 797

[47] Cristallo, S., Straniero, O., Piersanti, L., & Gobrecht, D. 2015, Astrophysical Journal, Supplement, 219, 40

[48] Csedreki, L., et al. 2021, Nuclear Instruments and Methods in Physics Research A, 994, 165081

[49] Cseh, B., et al. 2018, A&A, 620, A146

[50] Cseh, B., et al. 2022, Astronomy and Astrophysics, 660, A128

[51] Cyburt, R. H., et al. 2010, APJS, 189, 240

[52] Côté, B., Belczynski, K., Fryer, C. L., Ritter, C., Paul, A., Wehmeyer, B., & O'Shea, B. W. 2017, The Astrophysical Journal, 836, 230

[53] de Castro, D. B., Pereira, C. B., Roig, F., Jilinski, E., Drake, N. A., Chavero, C., & Sales Silva, J. V. 2016, Monthly Notices of the Royal Astronomical Society, 459, 4299

[54] Decressin, T., Charbonnel, C., Siess, L., & Palacios, A. 2004, Mem. Societa Astronomica Italiana, 75, 682

[55] Deheuvels, S., Ballot, J., Beck, P. G., Mosser, B., Østensen, R., García, R. A., & Goupil, M. J. 2015, A&A, 580, A96

[56] den Hartogh, J., Battino, U., Hirschi, R., Pignatari, M., & Herwig, F. 2017, in 14th International Symposium on Nuclei in the Cosmos (NIC2016), ed. S. Kubono, T. Kajino, S. Nishimura, T. Isobe, S. Nagataki, T. Shima, & Y. Takeda, 020904

[57] den Hartogh, J. W., Eggenberger, P., & Hirschi, R. 2019, A&A, 622, A187

[58] den Hartogh, J. W., et al. 2023, Astronomy and Astrophysics, 672, A143

[59] Denissenkov, P. A., & Tout, C. A. 2003, Monthly Notices of the Royal Astronomical Society, 340, 722

[60] Deuflhard, P. 1983, Numerische Mathematik, 41, 399

[61] Dillmann, I. 2013, private communication to Kadonis.org database, unpublished

[62] Dillmann, I., Domingo-Pardo, C., Heil, M., Käppeler, F., Walter, S., Dababneh, S., Rauscher, T., & Thielemann, F. K. 2010, Phys. Rev. C, 81, 015801

[63] Dillmann, I., Heil, M., Käppeler, F., Plag, R., Rauscher, T., & Thielemann, F.-K. 2006, in American Institute of Physics Conference Series, Vol. 819, Capture Gamma-Ray Spectroscopy and Related Topics, ed. A. Woehr & A. Aprahamian, 123–127

[64] Domingo-Pardo, C., et al. 2007, Phys. Rev. C, 75, 015806

[65] Dunbar, D. N. F., Pixley, R. E., Wenzel, W. A., & Whaling, W. 1953, Phys. Rev., 92, 649

[66] Eddington, A. S. 1925, The Observatory, 48, 73

[67] Edelmann, P. V. F., Röpke, F. K., Hirschi, R., Georgy, C., & Jones, S. 2017, A&A, 604, A25

[68] Eggenberger, P., Meynet, G., Maeder, A., Hirschi, R., Charbonnel, C., Talon, S., & Ekström, S. 2008, APSS, 316, 43

[69] Eggleton, P. P., et al. 2011, STARS: A Stellar Evolution Code, Astrophysics Source Code Library, record ascl:1107.008

[70] Endal, A. S., & Sofia, S. 1978, The Astrophysical Journal, 220, 279

[71] François, P., Matteucci, F., Cayrel, R., Spite, M., Spite, F., & Chiappini, C. 2004, A&A, 421, 613

[72] Freytag, B., Ludwig, H.-G., & Steffen, M. 1996, A&A, 313, 497

[73] Fricke, K. 1968, Zeitschrift fuer Astrophysik, 68, 317

[74] Fuller, G. M., Fowler, W. A., & Newman, M. J. 1985, The Astrophysical Journal, 293, 1

[75] Gallino, R., Arlandini, C., Busso, M., Lugaro, M., Travaglio, C., Straniero, O., Chieffi, A., & Limongi, M. 1998, APJ, 497, 388

[76] García-Hernández, D. A., Zamora, O., Yagüe, A., Uttenthaler, S., Karakas, A. I., Lugaro, M., Ventura, P., & Lambert, D. L. 2013, AA, 555, L3

[77] Goldreich, P., & Schubert, G. 1967, The Astrophysical Journal, 150, 571

[78] Goriely, S. 1999, A&A, 342, 881

[79] Goriely, S., & Siess, L. 2004, AA, 421, L25

[80] Guber, K. H., Sayer, R. O., Valentine, T. E., Leal, L. C., Spencer, R. R., Harvey, J. A., Koehler, P. E., & Rauscher, T. 2002, Phys. Rev. C, 65, 058801

[81] Heger, A., Langer, N., & Woosley, S. E. 2000, The Astrophysical Journal, 528, 368

[82] Heil, M., Juseviciute, A., Käppeler, F., Gallino, R., Pignatari, M., & Uberseder, E. 2009, PASA, 26, 243

[83] Heil, M., Käppeler, F., Uberseder, E., Gallino, R., Bisterzo, S., & Pignatari, M. 2008, Phys. Rev. C, 78, 025802

[84] Heil, M., Käppeler, F., Uberseder, E., Gallino, R., & Pignatari, M. 2007, Progress in Particle and Nuclear Physics, 59, 174, international Workshop on Nuclear Physics 28th Course

[85] Heil, M., et al. 2014, Phys. Rev. C, 90, 045804

[86] Heil, M., et al. 2008, The Astrophysical Journal, 673, 434

[87] Herwig, F. 2000, A&A, 360, 952

[88] Herwig, F. 2004, The Astrophysical Journal, 605, 425

[89] Herwig, F. 2005, ARA&A, 43, 435

[90] Herwig, F., Blöcker, T., Schönberner, D., & El Eid, M. F. 1997, A&A, 324, L81

[91] Herwig, F., et al. 2008, in Nuclei in the Cosmos (NIC X)

[92] Herwig, F., Freytag, B., Fuchs, T., Hansen, J. P., Hueckstaedt, R. M., Porter, D. H., Timmes, F. X., & Woodward, P. R. 2007, in Astronomical Society of the Pacific Conference Series, Vol. 378, Why Galaxies Care About AGB Stars: Their Importance as Actors and Probes, ed. F. Kerschbaum, C. Charbonnel, & R. F. Wing, 43

[93] Herwig, F., Langer, N., & Lugaro, M. 2003, APJ, 593, 1056

[94] Hirschi, R., Meynet, G., & Maeder, A. 2005, A&A, 433, 1013

[95] Hoyle, F., Dunbar, D. N. F., Wenzel, W. A., & Whaling, W. 1953, in Physical Review, Vol. 92, AMERICAN PHYSICAL SOC ONE PHYSICS ELLIPSE, COLLEGE PK, MD 20740-3844 USA, 1095–1095

[96] Iben, Jr., I., & Renzini, A. 1982, Astrophysical Journal, Letters, 259, L79

[97] Iliadis, C. 2015, Nuclear physics of stars (John Wiley & Sons, Ltd)

[98] Iliadis, C., D'Auria, J. M., Starrfield, S., Thompson, W. J., & Wiescher, M. 2001, ApJS, 134, 151

[99] Iliadis, C., Longland, R., Champagne, A., Coc, A., & Fitzgerald, R. 2010, Nuclear Physics A, 841, 31, the 2010 Evaluation of Monte Carlo based Thermonuclear Reaction Rates

[100] Jaeger, M., Kunz, R., Mayer, A., Hammer, J. W., Staudt, G., Kratz, K. L., & Pfeiffer, B. 2001, Physical Review Letters, 87, 202

[101] Jones, S. W., et al. 2019, Monthly Notices of the Royal Astronomical Society, 485, 4287

[102] Kamath, D., Karakas, A. I., & Wood, P. R. 2012, The Astrophysical Journal, 746, 20

[103] Karakas, A., & Lattanzio, J. C. 2007, Publications of the Astronomical Society of Australia, 24, 103–117

[104] Karakas, A. I. 2010, Monthly Notices of the Royal Astronomical Society, 403, 1413

[105] Karakas, A. I., & Lattanzio, J. C. 2014, PASA, 31, 30

[106] Karakas, A. I., & Lugaro, M. 2016, APJ, 825, 26

[107] Kippenhahn, R. 1974, in IAU Symposium, Vol. 66, Late Stages of Stellar Evolution, ed. R. J. Tayler & J. E. Hesser, 20

[108] Kippenhahn, R., Weigert, A., & Weiss, A. 2012, Stellar Structure and Evolution (Springer)

[109] Knobloch, E., & Spruit, H. C. 1983, Astronomy and Astrophysics, 125, 59

[110] Kobayashi, C., & Ibrahim, D. 2024, in EAS2024, European Astronomical Society Annual Meeting, 1821

[111] Kobayashi, C., Karakas, A. I., & Lugaro, M. 2020, The Astrophysical Journal, 900, 179

[112] Koehler, P. E. 2022, Phys. Rev. C, 105, 054306

[113] Koehler, P. E., Harvey, J. A., Winters, R. R., Guber, K. H., & Spencer, R. R. 2001, Phys. Rev. C, 64, 065802

[114] Krane, K. S. 1987, Introductory Nuclear Physics (John Wiley & Sons, Ltd)

[115] Käppeler, F., Beer, H., & Wisshak, K. 1989, Reports on Progress in Physics, 52, 945

[116] Käppeler, F., Gallino, R., Busso, M., Picchio, G., & Raiteri, C. M. 1990, APJ, 354, 630

[117] Langanke, K., & Martínez-Pinedo, G. 2000, Nuclear Physics A, 673, 481

[118] Langer, N., Fricke, K. J., & Sugimoto, D. 1983, Astronomy and Astrophysics, 126, 207

[119] Langer, N., Heger, A., Wellstein, S., & Herwig, F. 1999, Astronomy and Astrophysics, 346, L37

[120] Lawlor, T. M., & MacDonald, J. 2006, Monthly Notices of the Royal Astronomical Society, 371, 263

[121] Lederer, C., et al. 2013, Phys. Rev. Lett., 110, 022501

[122] Lederer, C., et al. 2014, Phys. Rev. C, 89, 025810

[123] Lewis, K. M., Lugaro, M., Gibson, B. K., & Pilkington, K. 2013, The Astrophysical Journal, 768, L19

[124] Li, K.-A., Qi, C., Lugaro, M., López, A. Y., Karakas, A. I., den Hartogh, J., Gao, B.-S., & Tang, X.-D. 2021, The Astrophysical Journal Letters, 919, L19

[125] Limongi, M., & Chieffi, A. 2006, APJ, 647, 483

[126] Lineweaver, C. H., Fenner, Y., & Gibson, B. K. 2003, in American Astronomical Society Meeting Abstracts, Vol. 203, American Astronomical Society Meeting Abstracts, 136.07

[127] Liu, N., Gallino, R., Cristallo, S., Bisterzo, S., Davis, A. M., Trappitsch, R., & Nittler, L. R. 2018, The Astrophysical Journal, 865, 112

[128] Liu, N., et al. 2014, The Astrophysical Journal, 786, 66

[129] Liu, N., et al. 2015, The Astrophysical Journal, 803, 12

[130] Liu, W., et al. 2022, in European Physical Journal Web of Conferences, Vol. 260, European Physical Journal Web of Conferences, 08001

[131] Longland, R., Martin, D., & José, J. 2014, AA, 563, A67

[132] Lugaro, M., & Chieffi, A. 2011, Radioactivities in Low- and Intermediate-Mass Stars (Berlin, Heidelberg: Springer Berlin Heidelberg), 83–151

[133] Lugaro, M., & Chieffi, A. 2018, in Astrophysics and Space Science Library, Vol. 453, Astrophysics and Space Science Library, ed. R. Diehl, D. H. Hartmann, & N. Prantzos, 643

[134] Lugaro, M., & Chieffi, A. 2018, Low- and Intermediate-Mass Stars (Cham: Springer International Publishing), 91–172

[135] Lugaro, M., et al. 2020, The Astrophysical Journal, 898, 96

[136] Lugaro, M., Davis, A. M., Gallino, R., Pellin, M. J., Straniero, O., & Käppeler, F. 2003, The Astrophysical Journal, 593, 486

[137] Lugaro, M., Herwig, F., Lattanzio, J. C., Gallino, R., & Straniero, O. 2003, APJ, 586, 1305

[138] Lugaro, M., Karakas, A. I., Pető, M., & Plachy, E. 2018, Geochim. Cosmochim. Acta, 221, 6

[139] Lugaro, M., Tagliente, G., Karakas, A. I., Milazzo, P. M., Käppeler, F., Davis, A. M., & Savina, M. R. 2014, APJ, 780, 95

[140] Maeder, A. ., & Meynet, G. 2000, ARA&A, 38, 143

[141] Marganiec, J., Dillmann, I., Pardo, C. D., & Käppeler, F. 2009, Phys. Rev. C, 80, 025804

[142] Marigo, P. 2012, in IAU Symposium, Vol. 283, Planetary Nebulae: An Eye to the Future, 87–94

[143] Marigo, P., Bressan, A., & Chiosi, C. 1996, A&A, 313, 545

[144] Marigo, P., Bressan, A., Girardi, L., Aringer, B., Gullieuszik, M., & Groenewegen, M. A. T. 2011, in Astronomical Society of the Pacific Conference Series, Vol. 445, Why Galaxies Care about AGB Stars II: Shining Examples and Common Inhabitants, ed. F. Kerschbaum, T. Lebzelter, & R. F. Wing, 431

[145] Marigo, P., Bressan, A., Nanni, A., Girardi, L., & Pumo, M. L. 2013, Monthly Notices of the Royal Astronomical Society, 434, 488

[146] Massimi, C., et al. 2012, Phys. Rev. C, 85, 044615

[147] Mathis, S., Palacios, A., & Zahn, J.-P. 2004, A&A, 425, 243

[148] McClave, J., & Sincich, T. 2020, Statistics (Pearson Education, Incorporated)

[149] Mohr, P., et al. 2004, Phys. Rev. C, 69, 032801

[150] Mutti, P., Beer, H., Brusegan, A., Corvi, F., & Gallino, R. 2005, AIP Conference Proceedings, 769, 1327

[151] Nishimura, N., Hirschi, R., Rauscher, T., Murphy, A. S. J., & Cescutti, G. 2016, Monthly Notices of the Royal Astronomical Society

[152] Nishimura, N., Rauscher, T., Hirschi, R., Murphy, A. S. J., Cescutti, G., & Travaglio, C. 2018, Monthly Notices of the Royal Astronomical Society, 474, 3133

[153] Nucci, M. C., & Busso, M. 2014, The Astrophysical Journal, 787, 141

[154] Oda, T., Hino, M., Muto, K., Takahara, M., & Sato, K. 1994, Atomic Data and Nuclear Data Tables, 56, 231

[155] Ota, S., et al. 2020, Physics Letters B, 802, 135256

[156] Palmerini, S., Busso, M., & Vescovi, D. 2020, Journal of Physics: Conference Series, 1668, 012032

[157] Palmerini, S., et al. 2021, The Astrophysical Journal, 921, 7

[158] Palmerini, S., Trippella, O., Busso, M., Vescovi, D., Petrelli, M., Zucchini, A., & Frondini, F. 2018, GCA, 221, 21

[159] Paxton, B., Bildsten, L., Dotter, A., Herwig, F., Lesaffre, P., & Timmes, F. 2010, APJ, 192, 3

[160] Paxton, B., et al. 2013, The Astrophysical Journal Supplement Series, 208, 4

[161] Paxton, B., et al. 2015, The Astrophysical Journal Supplement Series, 220, 15

[162] Paxton, B., et al. 2018, The Astrophysical Journal Supplement Series, 234, 34

[163] Paxton, B., et al. 2019, The Astrophysical Journal Supplement Series, 243, 10

[164] Pereira, C. B., Sales Silva, J. V., Chavero, C., Roig, F., & Jilinski, E. 2011, A&A, 533, A51

[165] Phillips, A. C. 1994, The physics of stars (John Wiley & Sons, Ltd)

[166] Piersanti, L., Cristallo, S., & Straniero, O. 2013, APJ, 774, 98

[167] Pignatari, M., Gallino, R., Heil, M., Wiescher, M., Käppeler, F., Herwig, F., & Bisterzo, S. 2010, The Astrophysical Journal, 710, 1557

[168] Pignatari, M., & Herwig, F. 2012, Nuclear Physics News, 22, 18

[169] Pignatari, M., et al. 2016, ApJS, 225, 24

[170] Pignatari, M., et al. 2023, Monthly Notices of the Royal Astronomical Society, stad2167

[171] Pols, O. R. 2011, Stellar Structure and Evolution (Astronomical Institute Utrecht, University of Utrecht)

[172] Pritychenko, B. 2020, EPJ Web Conf., 239, 07002

[173] Raiteri, C. M., Busso, M., Gallino, R., & Picchio, G. 1991, APJ, 371, 665

[174] Rauscher, T., Nishimura, N., Cescutti, G., Hirschi, R., & Murphy, A. S. J. 2018, in American Institute of Physics Conference Series, Vol. 1947, 14th International Symposium on Origin of Matter and Evolution of Galaxies (OMEG 2017), 020015

[175] Rauscher, T., Nishimura, N., Hirschi, R., Cescutti, G., Murphy, A. S. J., & Heger, A. 2016, Monthly Notices of the Royal Astronomical Society, 463, 4153

[176] Rauscher, T., & Thielemann, F.-K. 2000, Atomic Data and Nuclear Data Tables, 75, 1

[177] Raut, R., et al. 2013, Phys. Rev. Lett., 111, 112501

[178] Rees, N. R., Izzard, R. G., & Karakas, A. I. 2024, Monthly Notices of the Royal Astronomical Society, 527, 9643

[179] Reifarth, R. 2014, https://exp-astro.physik.uni-frankfurt.de/kadonis1.0/index.php

[180] Reifarth, R., et al. 2018, European Physical Journal Plus, 133, 424

[181] Reifarth, R., Lederer, C., & Käppeler, F. 2014, Journal of Physics G: Nuclear and Particle Physics, 41, 053101

[182] Richard, D., & Zahn, J.-P. 1999, Astronomy and Astrophysics, 347, 734

[183] Ritter, C., Herwig, F., Jones, S., Pignatari, M., Fryer, C., & Hirschi, R. 2018, Monthly Notices of the Royal Astronomical Society, 480, 538

[184] Rohlf, J. W., & Collings, P. J. 1994, Physics Today, 47, 62

[185] Rolfs, C., & Rodney, W. 1988, Cauldrons in the Cosmos: Nuclear Astrophysics, Theoretical Astrophysics (University of Chicago Press)

[186] Roriz, M. P., Lugaro, M., Pereira, C. B., Sneden, C., Junqueira, S., Karakas, A. I., & Drake, N. A. 2021, Monthly Notices of the Royal Astronomical Society, 507, 1956

[187] Salaris, M., & Cassisi, S. 2005, Evolution of Stars and Stellar Populations (Wiley)

[188] Siess, L., Goriely, S., & Langer, N. 2004, A&A, 415, 1089

[189] Spitoni, E., Matteucci, F., & Sozzetti, A. 2014, Monthly Notices of the Royal Astronomical Society, 440, 2588

[190] Spruit, H. C., Knobloch, E., & Roxburgh, I. W. 1983, Nature, 304, 520

[191] Straniero, O., Cristallo, S., & Piersanti, L. 2014, Astrophysical Journal, 785, 77

[192] Straniero, O., Cristallo, S., & Piersanti, L. 2015, in Astronomical Society of the Pacific Conference Series, Vol. 497, Why Galaxies Care about AGB Stars III: A Closer Look in Space and Time, ed. F. Kerschbaum, R. F. Wing, & J. Hron, 259

[193] Straniero, O., Gallino, R., Busso, M., Chiefei, A., Raiteri, C. M., Limongi, M., & Salaris, M. 1995, The Astrophysical Journal Letters, 440, L85

[194] Straniero, O., Gallino, R., & Cristallo, S. 2006, Nuclear Physics A, 777, 311

[195] Sweet, P. A. 1950, Monthly Notices of the Royal Astronomical Society, 110, 548

[196] Tagliente, G., Lugaro, M., Karakas, A. I., Milazzo, P. M., & n TOF Collaboration. 2012, in Nuclei in the Cosmos (NIC XII), ed. J. Lattanzio, A. Karakas, M. Lugaro, & G. Dracoulis, 25

[197] Taioli, S., Vescovi, D., Busso, M., Palmerini, S., Cristallo, S., Mengoni, A., & Simonucci, S. 2022, The Astrophysical Journal, 933, 158

[198] Takahashi, K., & Yokoi, K. 1987, Atomic Data and Nuclear Data Tables, 36, 375

[199] Thielemann, F.-K., et al. 2011, Progress in Particle and Nuclear Physics, 66, 346, particle and Nuclear Astrophysics

[200] Thielemann, F. K., Arnould, M., & Truran, J. W. 1986, in Advances in Nuclear Astrophysics, ed. E. Vangioni-Flam, J. Audouze, M. Casse, J.-P. Chieze, & J. Tran Thanh Van, 525–540

[201] Thielemann, F.-K., et al. 2010, Journal of Physics: Conference Series, 202, 012006

[202] Thompson, W. J., & Iliadis, C. 1999, Nuclear Physics A, 647, 259

[203] Timmes, F. X. 1999, ApJS, 124, 241

[204] Travaglio, C., Gallino, R., Arnone, E., Cowan, J., Jordan, F., & Sneden, C. 2004, APJ, 601, 864

[205] Travaglio, C., Röpke, F. K., Gallino, R., & Hillebrandt, W. 2011, APJ, 739, 93

[206] Trippella, O., Busso, M., Palmerini, S., Maiorca, E., & Nucci, M. C. 2016, The Astrophysical Journal, 818, 125

[207] Vassiliadis, E., & Wood, P. R. 1993, The Astrophysical Journal, 413, 641

[208] Vescovi, D. 2022, Universe, 8

[209] Vescovi, D., Cristallo, S., Busso, M., & Liu, N. 2020, The Astrophysical Journal Letters, 897, L25

[210] Vitense, E. 1953, Zeitschrift fuer Astrophysik, 32, 135

[211] von Zeipel, H. 1924, Monthly Notices of the Royal Astronomical Society, 84, 665

[212] Žugec, P., et al. 2014, Phys. Rev. C, 89, 014605

[213] Wallner, A., et al. 2016, Phys. Rev. C, 93, 045803

[214] Wasiutynski, J. 1946, Astrophysica Norvegica, 4, 1

[215] Werner, K., & Herwig, F. 2006, Publications of the ASP, 118, 183

[216] Wisshak, K., Voss, F., Käppeler, F., Krticka, M., , & Raman, S. 2004, Stellar neutron capture cross section of the unstable branching point sup 151Sm

[217] Yoon, S.-C., & Langer, N. 2004, A&A, 419, 623

[218] Zahn, J. P. 1974, in IAU Symposium, Vol. 59, Stellar Instability and Evolution, ed. P. Ledoux, A. Noels, & A. W. Rodgers, 185

[219] Zahn, J.-P. 1992, A&A, 265, 115

[220] Zamora, O., Abia, C., Plez, B., Domínguez, I., & Cristallo, S. 2009, A&A, 508, 909

[221] Zinner, E. 1998, Annual Review of Earth and Planetary Sciences, 26, 147

[222] Zinner, E. 2014, Presolar Grains, Vol. 1 (Elsevier), 181–213

[223] Zinner, E., Nittler, L. R., Gallino, R., Karakas, A. I., Lugaro, M., Straniero, O., & Lattanzio, J. C. 2006, APJ, 650, 350

[224] Žerovnik, G., Trkov, A., Smith, D. L., & Capote, R. 2013, Nuclear Instruments and Methods in Physics Research Section A: Accelerators, Spectrometers, Detectors and Associated Equipment, 727, 33